STRUCTURAL CHARACTERISTICS OF ARTICULAR CARTILAGE IN THE EARLY DETECTION OF POST-TRAUMATIC OSTEOARTHRITIS BY MICROSCOPIC IMAGING TECHNIQUES

by

HANNAH MANTEBEA

A dissertation submitted in partial fulfillment of the
requirements for the degree of

DOCTOR OF PHILOSOPHY IN BIOMEDICAL SCIENCES:

MEDICAL PHYSICS

2023

Oakland University
Rochester, Michigan

Doctoral Advisory Committee:

Yang Xia, Ph.D., Chair
Bradley J Roth, Ph.D.
Evgeniy Khain, Ph.D.
Eugene Surdutovic, Ph.D.
Jiang Quan, Ph.D.

To my Family and Friends Who Have Been Supportive Through This Journey
You Are Irreplaceable!!

ACKNOWLEDGMENTS

These studies were performed through the Department of Physics: Medical Physics Program. I am grateful and indebted to my advisor Yang Xia Ph.D. for his immense support, motivation, and guidance throughout my research years working with him. My utmost sincere gratitude and respect goes to Bradley J. Roth Ph.D. for his advice and continuing selfless support. I am thankful to Eugene Surdutovic Ph.D. for his never-ending encouragement. To the entire Xia Lab team especially Farid Badar, Syeda Batool, Amanveer Singh, Austin Tetmeyer, Aaron Blanc, and Sarah Salem for their help. I would like to thank all my co-authors from these studies and copyright owners who permitted me to use their work. I am thankful to the dissertation committee members; Dr. Evgeniy Khain and Dr. Jiang Quan for their warm response and enthusiastic reception to becoming part of the committee. To Beaumont Research Institute; Michael Newton and Kevin Baker for their contribution towards sample acquisition. I am also thankful for the grant support from the National Institutes of Health (AR069047). I am thankful to Oakland University for allowing me to advance toward my career goal.

Hannah Mantebea

ABSTRACT

STRUCTURAL CHARACTERISTICS OF ARTICULAR CARTILAGE IN THE EARLY DETECTION OF POST-TRAUMATIC OSTEOARTHRITIS BY MICROSCOPIC IMAGING TECHNIQUES

by

HANNAH MANTEBEA

Adviser: Yang Xia Ph.D.

Cartilage is a specialized form of connective tissue that provides support and cushioning to adjacent tissues in the body. Cartilage is of three types: Hyaline, fibrocartilage, and elastic. The articular cartilage is a hyaline type and is the most found throughout the animal and human bodies. Articular cartilage is composed of a dense extracellular matrix (ECM) with specialized cells, and chondrocytes, which are sparsely distributed. The ECM is primarily made up of collagen, proteoglycan, water, non-collagenous proteins, and glycoproteins. The components of the ECM are subject to change in the disease state, especially in osteoarthritis. As a result of the complex and unique nature of the articular cartilage, early detection, treatment, and repair pose a challenge in clinic. Imaging techniques such as magnetic resonance imaging (MRI) has been used in the noninvasive evaluation of the cartilage structure, and polarized light microscopy (PLM) allows the examination of the molecular organization at optical resolution.

The first project in this dissertation aimed to study the structural characteristics of the articular cartilage in the patella and the fibrocartilage of the suprapatella in the knee

joint. This was achieved quantitatively using μMRI and PLM at both low and high resolutions. The second project in this dissertation aimed to compare the structures between the immature and mature articular cartilage of the femur and humerus qualitatively and quantitatively using μMRI and PLM. The third project in this dissertation was aimed at the structural characteristics of the articular cartilage in the disease state. Specifically qualitative and quantitative characteristics from traumatized joints (post-traumatic osteoarthritis) were studied using μMRI and PLM at high resolutions.

These studies confirmed the ability of μMRI and PLM to examine the cartilage structure quantitatively and qualitatively in a healthy state and in a diseased state. The ability to study the microscopic anatomy of cartilage and pathology (osteoarthritis) in the early stage will contribute to the treatment and early diagnosis of arthritis.

TABLE OF CONTENTS

TABLE OF CONTENTS—Continued

TABLE OF CONTENTS—Continued

TABLE OF CONTENTS—Continued

LIST OF TABLES

LIST OF FIGURES

LIST OF ABBREVIATIONS

1D	One dimensional
2D	Two dimensional
ACL	Anterior cruciate ligament
B_0	Static magnetic field
B_1	Magnetic field of the excitation pulse
CCD	Charge-coupled device
CT	Computed tomography
ECM	Extracellular matrix
FID	Free induction decay
FOV	Field of view
GAG	Glycosaminoglycan
ICP	Inductively coupled plasma
MMP	Matrix metalloproteinase
MR	Magnetic resonance
MRI	Magnetic resonance imaging
MSME	Multi-slice multi-echo
NMR	Nuclear magnetic resonance
OA	Osteoarthritis
OES	Optical emission spectrometry
OPD	Optical path difference
PI	Protease inhibitor

PLM	Polarized light microscopy
PTOA	Post-traumatic osteoarthritis
RF	Radiofrequency
ROI	Region of interest
RZ	Radial zone
SE	Spin echo
SZ	Superficial zone
T1	Longitudinal relaxation time
T2	Transverse relaxation time
TE	Echo time
TR	Repetition time
TZ	Transitional zone
UTE	Ultra-short echo
ρ	rho

LIST OF PUBLICATIONS

This dissertation is based upon the following original research articles referred to by their Roman numeral:

I. Mantebea, H., Batool, S., Hammami, M., & Xia, Y. (2021). Structural Morphology of Rabbit Patella and Suprapatella Cartilage by Microscopic MRI and Polarized Light Microscopy. *Cartilage*, 1–11. https://doi.org/10.1177/1947603521990882

II. Mantebea, H., Batool, S., Singh, A., Hammami, M., Badar, F., & Xia, Y. (2022). Structural differences between immature and mature articular cartilage of rabbits by microscopic MRI and polarized light microscopy. *Journal of Anatomy*, *December 2021*, 1–11. https://doi.org/10.1111/joa.13620

III. Mantebea H., Singh A., Badar A., Abdelmessih G., Sebastian M.T., Baker K., Newton M., Xia Y. Characteristics of Distal Femoral Articular Cartilage in Six Weeks Post-Traumatic Osteoarthritis by a Sub-critical Impact (summited to *Journal of Orthopedic Research*)

CO-AUTHORED ARTICLE

I. Batool, S., Hammami, M., Mantebea, H., Badar, F., & Xia, Y. (2022). Location-Specific Study of Young Rabbit Femoral Cartilage by Quantitative μMRI and Polarized Light Microscopy. Cartilage, 13(1), 194760352210851. https://doi.org/10.1177/19476035221085143

CHAPTER ONE

INTRODUCTION

Osteoarthritis (OA) is characterized by the degeneration of articular cartilage in synovial joints resulting from imbalanced mechanical and biological events in the tissue. This leads to pain, stiffness, and disability (Ishiguro et al., 2002; Thomas et al., 2012). The risk factors prevalent in osteoarthritis include age, previous joint injuries, gender, obesity, and genetics (Pritzker, 1994). Post-traumatic osteoarthritis (PTOA) is a form of osteoarthritis characterized by damage resulting from traumatic injury. The nature of injury associated with PTOA is a fracture, recurrent instability, and ligament tear. PTOA is common in the lower extremities (knee and ankle) and costly in its treatment. In the United States, individuals with PTOA account for 12% of all osteoarthritis cases with approximately 5.6 million of such cases related to the lower extremities (Brown et al., 2006). The effect of osteoarthritis affects the whole joint including the synovial membrane, periarticular muscles, capsules, subchondral bone, and ligaments (Ishiguro et al., 2002).

In preclinical studies involving PTOA, animal models are essential as human tissues in the early stages of the disease are unavailable until the end stage of the disease. The animal injury model is also advantageous in PTOA as the impact dose can be determined and pathological changes in cartilage and related structures can be monitored as the time of the disease progresses. The rabbit model has been commonly used in research since it is less costly (Racine & Aaron, 2014). More importantly, the rabbit has more phylogenetic, hemodynamic, and histological similarities to humans. To appreciate

the alterations in the articular cartilage involved in the progression of the disease, the cartilage structure must be understood (Mantebea et al., 2021).

The cartilage contains a small number of living cells, chondrocytes, that are scattered within an extracellular matrix (ECM). The ECM is made of primarily collagen fibers, proteoglycans, fibronectins, integrins, water, and non-collagenous proteins (Ishiguro et al., 2002; Shah et al., 2007). In the knee and other synovial joints, articular cartilage covers the ends of the joint bones. The collagen fibers are made up of mainly Type II and the proteoglycans are macromolecules with glycosaminoglycan side chains. The highly negatively charged glycosaminoglycan chains make the proteoglycans attract cations and water molecules (Xia, 1998). Structurally, adult articular cartilage can be sub-divided into three histological zones; the superficial zone where collagen fibers are parallel in arrangement, the randomized transitional zone, and the perpendicularly arranged radial zone (Lee & Xia, 2013).

The studies carried out in this dissertation used microscopic magnetic resonance imaging (μMRI) and polarized light microscopy (PLM) to determine the structure of the cartilage from the rabbit knee joints and the changes in the tissue structures resulting from traumatically induced PTOA. μMRI is a non-invasive imaging technique that provides excellent tissue contrast at high resolution. In knee imaging using MRI, different pulse sequences can be used (Hash, 2013) to determine various NMR parameters in tissue. For example, T2 relaxation is sensitive to the anisotropic motion of water molecules through dipolar interaction owing to collagen fiber orientation (Xia, 1998). This anisotropy of T2 causes laminar appearance in articular cartilage when the cartilage

surface is made parallel to the external magnetic field (B_0); when the tissue is set at 55˚ to B_0, the laminar appearance can disappear, as a result of minimized dipolar interaction (Xia, 1998). In addition, T1ρ relaxation is the spin-lattice relaxation time in the rotating frame, which is sensitive to slow motional interaction between macromolecules and water in tissues. The values of T1ρ are dependent on the strength of the spin-lock pulse, which can become less anisotropic in biological tissues (Regatte et al., 2006).

Polarized light microscopy (PLM) is an imaging technique that is commonly used in studying the architecture of collagen fibers at optical resolutions. PLM can be used to quantify the retardation (optical path difference between electromagnetic fields entering and emerging out of tissue) of samples. PLM also allows the determination and visualization of the angular orientation of the collagen fibers in cartilage (Lee & Xia, 2013).

To further provide an additional complementary explanation to the imaging findings is the assessment of the element concentrations in the articular cartilage, where inductively coupled plasma-optical emission spectrometry (ICP-OES) was performed in this dissertation. The ICP-OES is one of the spectroscopic techniques that allows the elementary elements in cartilage to be determined using plasma.

In this dissertation, the experimental works studied cartilage structure with a goal for the early detection of osteoarthritis, using different imaging modalities qualitatively and quantitatively at high resolutions. The dissertation is divided into six chapters. The literature overview is presented in chapters two and three. Chapters four, five, and six are three original research papers based on three individual projects; two of the papers have been published in peer-reviewed journals, and the third paper has been submitted to a

journal for consideration. Chapter seven is a summary of the dissertation research and further studies for the future.

CHAPTER TWO

THE KNEE JOINT, CARTILAGE, AND OSTEOARTHRITIS

2.1 The knee joint

The knee is a complex joint that comprises of a tibiofemoral joint and patellofemoral joint (Flandry & Hommel, 2011). As a modified hinge joint, the knee has a wide range of movement in extension and flexion in the frontal, sagittal and transverse planes (Abulhasan & Grey, 2017). The extensor mechanism is associated with the patellofemoral joint whiles the tibiofemoral joint allows the joint to withstand the body weight from the femur through to the tibia (Flandry & Hommel, 2011).

The knee encompasses muscles, bones, cartilage, and ligaments. The ligaments are fibrous bands of tissue that primarily provide stability to the joint, most importantly the anterior cruciate ligament (ACL) (Ellison & Berg, 1985). The bones of the knee joint are mainly long bones (femur, tibia, fibula) and sesamoid bones (patella). The diaphysis (shaft) of long bones is made up of compact bone that merges into the epiphysis (end from the shaft) made of spongy bone. Spongy bone has a trabecular formation. During the process of maturation, the bone cells are of three types: osteoblast, osteocytes, and osteoclast. In matured bone, the cells are predominantly osteocytes found in lacunae of calcified interstitial substance. During the formation of bone tissue, the osteoblast plays a major role (Lehneis, 1987). The bone plays a major role in locomotion and supports vital organs. It also regulates calcium concentration in body fluids and protects components responsible for blood formation.

Other joints affected by OA are the shoulder joint, the ankle, the spinal cord and the wrist. These joints are mostly affected due to effect of weight bearing and repetitive use in everyday life.

2.2 Gross anatomy of the rabbit Knee

The rabbit knee joint is similar in structure to the human knee joint. The long bone of this joint is the femur which meets with the top of the tibia and fibula aligned and parallel to the side of the tibia. The top of the tibia has menisci to reduce shock and absorb impact during motion. The joint has several sesamoid bones with the largest and most significant being the patella (Tecklenburg et al., 2006). The patella glides along the groove located in front of the femur. In rabbit, the femur articulating surface is the patella and proximal to it is the suprapatella. The suprapatella is sesamoid fibrocartilage, embedded in the quadriceps tendon (Ralphs et al., 1992). This suprapatellar structure is not found in humans; and in rabbit for extremely flexed knee, it is a weight-bearing organ (Tischer et al., 2002).

2.3 Cartilage

There are three types of cartilage: hyaline, fibrocartilage, and elastic cartilage. Hyaline cartilage is smooth and glasslike found in bones and linings of joints. This type of cartilage is most commonly found in mammals. Elastic cartilage is similar to hyaline but has elastic bundles or elastin scattered in its matrix. An example of this cartilage type is found in the walls of the auditory system. Fibrocartilage is found in areas where tensile strength and tough support are required. An example of this cartilage type is found in between intervertebral disks (Parvizi & Kim, 2010). For the rest of the dissertation, the word *cartilage* refers to *articular cartilage*.

2.3.1 Articular cartilage

Articular cartilage (figure 2.2) is a hyaline cartilage that covers the ends of bones in joints. It is a viscoelastic and avascular connective tissue with a lubricated surface to reduce load bearing and friction (Carballo et al., 2017). The main components of articular cartilage include chondrocytes, collagen, proteoglycans, non-collagenous proteins, and water. The chondrocytes are highly

specialized cells in cartilage, which are sparsely embedded in an extracellular matrix (ECM) (Buckwalter et al., 2005). Chondrocytes are known to synthesize proteoglycans, collagen, fibronectin integrins, and adhesive proteins in the ECM, which maintain low compressibility and tensile strength under load (Camarero-Espinosa et al., 2016; Ishiguro et al., 2002). Structurally, chondrocytes reside in lacunae and are embedded in the arcade-like network of collagen fibrils in zone-specific regions of the cartilage, i.e., the superficial, transitional, deep, and calcified zones (Poole, 1999); (Camarero-Espinosa et al., 2016; Xia, 1998; Xia et al., 2001). The major proteoglycan in articular cartilage is aggrecans made of large chains of chondroitin sulfate (Poole et al., 2001). Proteoglycans are made up of a core protein to which glycosaminoglycan (GAG) chains are bonded covalently (Poole, 1999). The content of proteoglycans increases along the thickness of the cartilage. Water provides a significant weight at about 60-70% to articular cartilage, and is responsible for to the proton signals in magnetic resonance imaging (MRI) (Xia. et al., 2016). In articular cartilage, type II collagen fiber makes up 40% of its' dry weight (Parvizi & Kim, 2010). Collagen type III, VI, IX, X, XII, and XIV are other types of collagen present in the cartilage. Collagen is protein in nature and the major solid component of the cartilage.

2.4 Osteoarthritis

Osteoarthritis (OA) is characterized by progressive changes in joint structures that are preceded by the degenerative changes of articular cartilage (Umlauf et al., 2010). These changes also occur in the subchondral bone, the synovial fluid, and the synovial membrane. Osteoarthritis is classed as either primary or secondary depending on the cause of diagnosis. In the knee, important risk factors are age, gender, obesity, genetic predisposition, physical occupational load, and previous joint injuries (Pritzker, 1994; Snoeker et al., 2020). Primary OA is from an unavoidable cause such as age. Secondary OA occurs because of other conditions such as trauma and obesity.

Uncontrolled proteolysis of the extracellular matrix in cartilage leads to alteration and destruction of the joint (Umlauf et al., 2010). In the initial stages of OA, pro-inflammatory cytokines induce chondrocyte metabolism which leads to alterations of the structure of the cartilage matrix. The cytokines (IL-1β and TNF-α) are mediators of inflammation whose effect induces chondrocytes to trigger ECM-degrading enzymes such as metalloproteinases (MMPs), collagenase, and aggrenase (Fernandes et al., 2002). The MMP is important alongside collagenase in the cleavage of collagen type II fibers (Poole, 1999). The activated MMPs cause loss of aggrecan and degradation of proteoglycans that lead to significant loss of mechanical properties of the cartilage (Ishiguro et al., 2002). Consequently, water content in the matrix can increase. During the initial degradation, there is a repair attempt by chondrocytes to proliferate in order to synthesize collagen type II and proteoglycan until attempts are outmatched by degradation (Poole et al., 2001). There is a display of swelling progressing to fibrillation at the surface and eventually loss of cartilage tissue exposing the subchondral bone (Kidd, 2012). Intraosseous hypertension causes trabecular remodeling, thickening of subchondral bone, and periosteal new bone formation (Racine & Aaron, 2014).

2.5 Post-traumatic osteoarthritis (PTOA)

PTOA occurs as a result of joint trauma. Several risk factors contribute to PTOA. In knee injury, the anterior cruciate ligament (ACL) tear, meniscal injury and intra-articular fracture ligament injuries, quadriceps weakness (Palmieri-Smith & Thomas, 2009), and alteration in load at the injured site all contribute to PTOA (Racine & Aaron, 2014). In addition, genetic risk factors contribute to the susceptibility to PTOA (Spector & MacGregor, 2004; Valdes et al., 2013). Finally, repetitive use of joints from physical activities contributes to PTOA (Johnson & Hunter, 2014).

2.5.1 Progression of PTOA in the knee joint

Several factors contribute to the progression of OA after injury driven by failure in joint biomechanics, biochemical cascades, and neurological and cellular immunity responding to an inflammatory environment. Mechanical damage results from abnormal loading to the knee joints which contributes to the damage of static stabilizing structures including the cartilage, quadriceps, and hamstring, joint instability, and muscle weakness. Mechanical loading leads to disruption in homeostasis through changes in chondrocyte metabolism (Carbone & Rodeo, 2017). The biological factors, jointly with the associated damaged structures, have the tendency to trigger the degeneration of the joint progressively. The factors include synovial cellular infiltration, cytokine production (IL-1, IL-6, IL-8, IL-17, and TNF-α), and inflammatory activation of joint tissue cells; all of which can cause the progression of the disease through the release of cytokines and free oxygen radicals from chondrocytes to cause chondrocyte damage and matrix degradation (Riordan et al., 2014).

Injury to the knee joint may cause damage to the neuromuscular function, which can contribute to the disease progression. This neuromuscular alteration results from the impairment to muscular functions and persistent ligament laxity (Dare & Rodeo, 2014). The progression of OA driven by chronic inflammation is known to also have the ability to repair the damaged tissue as a result of newly formed blood vessels that infiltrate the cartilage tissue in disease (Li et al., 2019).

2.5.2 Role of other structures of the knee in PTOA

Despite damage to cartilage being a characteristic of OA, the progression of the disease is influenced by all other structures of the knee. The connections between

cartilage and subchondral bone are vital in joint homeostasis and disease progression. The subchondral bone beneath the calcified cartilage consists of a subchondral plate (cortical bone), and a deeper layer of subchondral trabecular or cancellous bone. In OA the subchondral bone plate increases in volume and thickness along with alterations in the subchondral trabecular bone. OA causes neovascularization of subchondral bone and nerve infiltration from the bone to invade the overlying cartilage tissue, making a communication channel for the exchange of biological factors (Funck-Brentano & Cohen-Solal, 2015).

The synovium which consists of the synovial fluid and synovial membrane acts as a reservoir for nutrients and degrading products (macrophage-like synoviocytes) to both healthy and diseased cartilage (Hügle & Geurts, 2017). In OA synovitis stimulated by mediators of inflammation and synovial hypertrophy is associated with the disease progression.

Abnormal mechanical loading in OA can cause meniscal lesions and tears, due to a decrease in resistance to tension, compression, and shear stress. This leads to damage to cartilage, changes in subchondral bone, lesions of bone marrow, and synovitis (Englund et al., 2012). Other structures such as the quadriceps, hamstring, and muscles that play a role in daily movement can all become weak during OA, which is impacted by the knee biomechanics (Alnahdi et al., 2012).

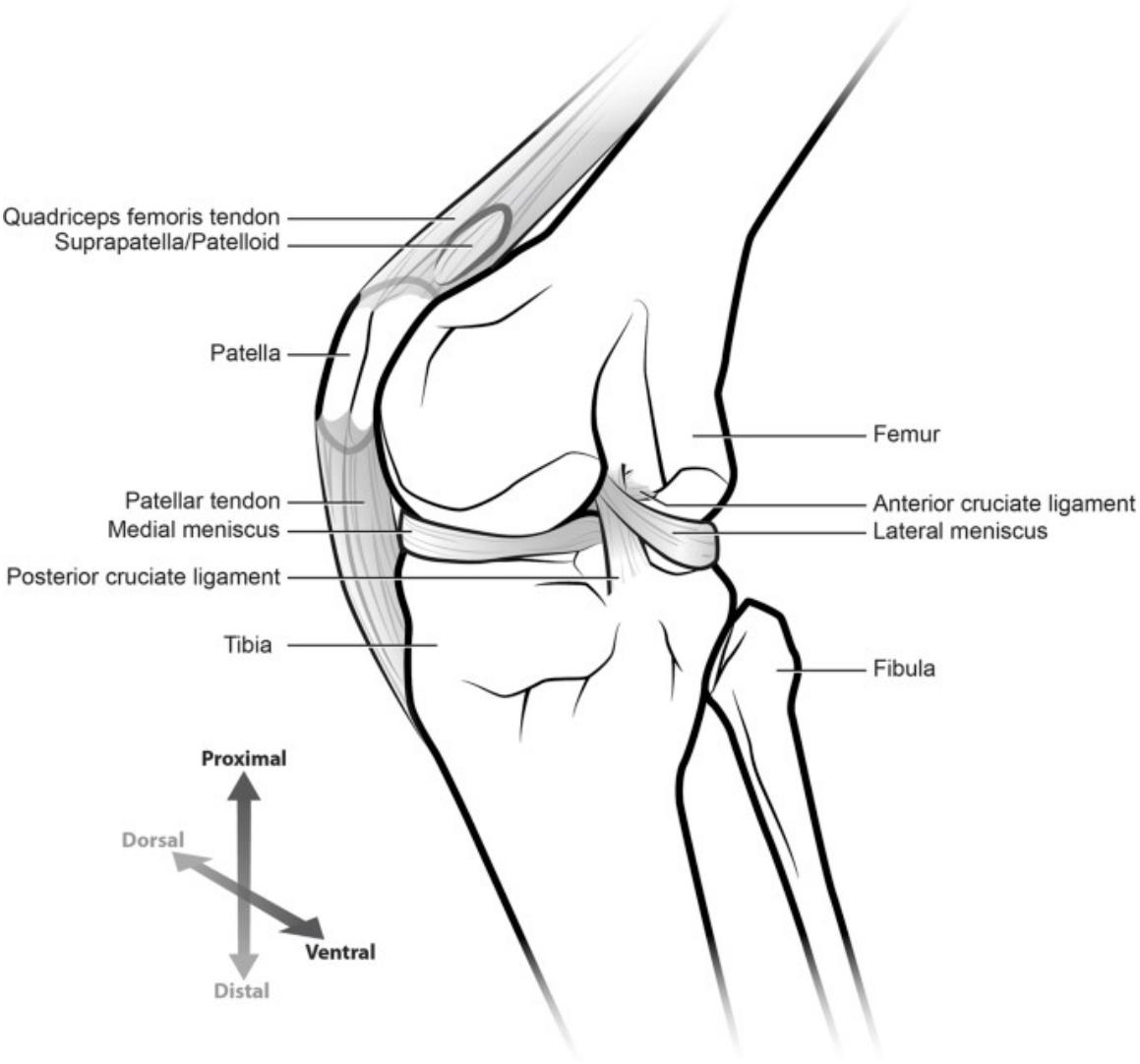

Figure 2.1 Schematic representation of the rabbit knee joint. (Reproduced with permission from Samuels et al. 2017)

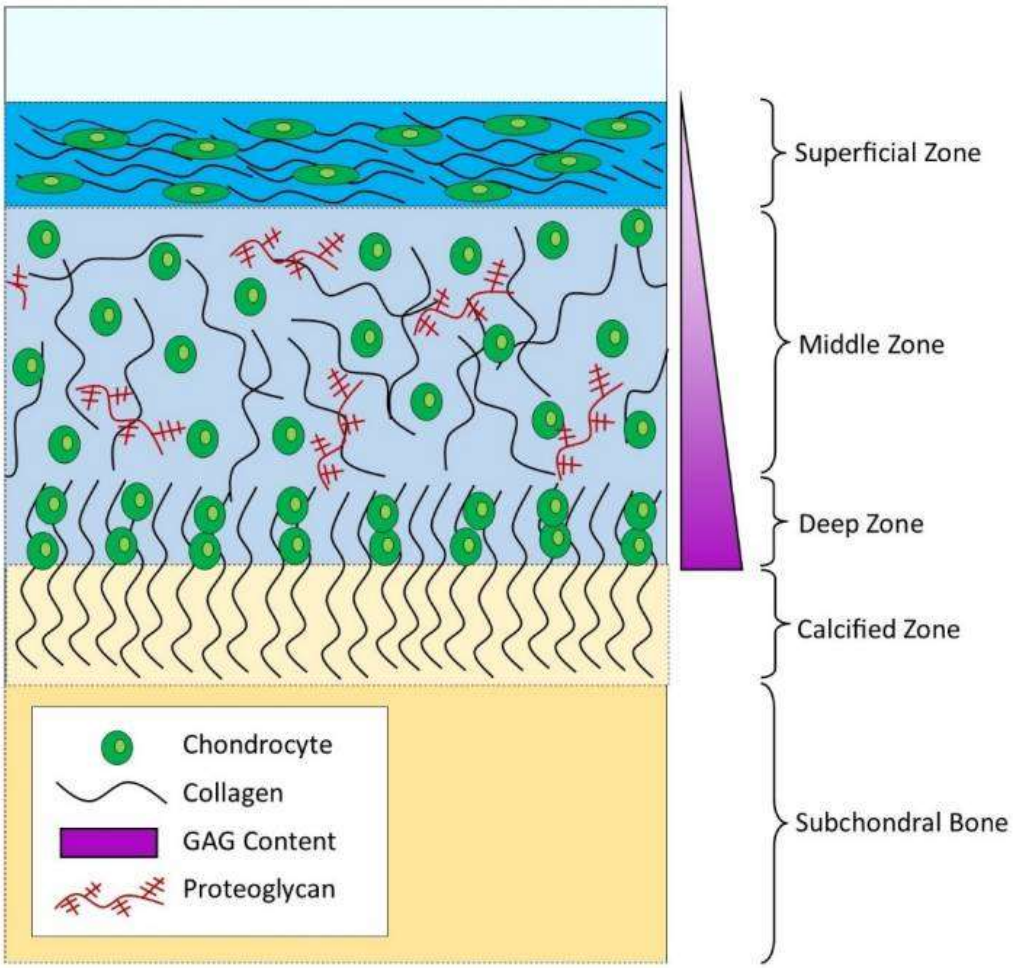

Figure 2.2 Structure of articular cartilage.
(Image reproduced under creative commons license on from (Davies & Kuiper, 2019) Regenerative Medicine: A Review of the Evolution of Autologous Chondrocyte Implantation ACI Therapy *Bioengineering* 6(1):22)

CHAPTER THREE

IMAGING TECHNIQUES AND ELEMENT DETERMINATION IN CARTILAGE

3.1 Imaging in Knee and Osteoarthritis Studies

General x-ray radiography, computed tomography (CT), and magnetic resonance imaging (MRI) are modalities often used in the clinic. However, due to the challenges in the use of radiographs to visualize soft tissue of cartilage (Novakofski et al., 2016), CT and MRI are preferred choices in clinical studies involving early detection of osteoarthritis.

3.2 Magnetic Resonance Imaging (MRI)

Magnetic Resonance Imaging is a non-invasive imaging technique that uses nonionizing radiation to excite nuclei to produce images. The protons of the hydrogen atoms are most commonly used in MRI due to their abundance in biological tissue (Plewes & Kucharczyk, 2012). MRI has its roots from the physics and application of nuclear magnetic resonance (NMR).

3.2.1 Nuclear Magnetic Resonance Overview

The concept of nuclear magnetic resonance is based on the atomic properties of atoms and the interaction of its proton nuclear spins with an external magnetic field (B_0). Quantum mechanically, the hydrogen nuclei, protons, have an intrinsic property called spin I; the protons also have a magnetic moment μ. The spin states of the protons are quantized with specific values to a nucleus. For the protons of the hydrogen atoms, the spin I has a value of ½, which yields two allowed states (+1/2 and -1/2) from the equation,

$$m = 2I + 1 \quad (3.1).$$

The magnetic moment associated with the nucleus of spin I is given by

$$\mu = \gamma \hbar I \quad (3.2)$$

where, μ is the magnetic moment (J T^{-1}), γ is the gyromagnetic ratio (rad sec^{-1} T^{-1}) and $\hbar$ is the Planck's constant divided by 2π (1.055 x 10^{-34} J s),

Individual nuclear spins can be visualized as a line vector on the surface of a cone that is either parallel or antiparallel with the external magnetic field B_0 (which is set along the z axis in the laboratory frame of reference). The line vector precesses around the B_0 on the cone surface at the Larmor frequency ω,

$$\omega = \gamma B_o \quad (3.3)$$

For any practical sample, the number of the individual nuclear spins is enormous (given the Avogadro's constant). There is a population difference between the parallelly and antiparallelly precessing nuclei, which is due to the Boltzmann distribution,

$$\frac{n_-}{n_+} = e^{\frac{-\Delta E}{kT}} \quad (3.4)$$

where n_- and n_+ are the number of spins in the two energy states, k is the Boltzmann constant, T is the absolute temperature, and ΔE is the difference in the energy between the two states, given by

$$\Delta E = \frac{-h\gamma B_o}{2\pi} \quad (3.5)$$

This population difference of the nuclei between the two energy states for a spin half system results in a net macroscopic magnetization vector (M), which in thermal equilibrium points in the direction of the external magnetic field B_0, since there are more protons aligning themselves in parallel to B_0 (Novakofski et al., 2016). In thermal

equilibrium and with a typical Cartesian coordinate system, this macroscopic magnetization M is entirely on the z-axis (i.e., $M = M_z$); there is no transverse magnetization.

A transverse magnetization (M_{xy}) can be established by forcing M away from its thermal equilibrium (along the z axis) towards the transverse plane (the x-y plane), with the use of an alternating magnetic field/pulse B_1 at the Larmor frequency (Plewes & Kucharczyk, 2012). This transverse magnetization can induce an electric current in a receiver coil, which is subsequently amplified as the MRI signal, called the free induction decay (FID) (Plewes & Kucharczyk, 2012).

As soon as the macroscopic magnetization M is tipped away from its thermal equilibrium, there is a regrowth of the magnetization longitudinally and a decay of the magnetization transversely. The longitudinal recovery process is called spin-lattice relaxation (T1), while the transverse dephasing process is called spin-spin relaxation (T2). In addition to the T2 relaxation process due to the spin system, inhomogeneities from equipment can also cause the signal to dephase (Novakofski et al., 2016).

The motion of the magnetization M after the application of the resonant rf pulses can be described by the following two equations,

$$\frac{dM_z}{dt} = -\frac{M_z - M_o}{T_1} \tag{3.6}$$

And

$$\frac{dM_{xy}}{dt} = -\frac{M_{xy}}{T_2} \tag{3.7}$$

Since the two relaxation processes can be considered independent of each other, the motion of the magnetization can be written as

$$\frac{dM}{dt} = \Upsilon(MxB) - \left[\frac{(M_x i + M_y j)}{T_2} + \frac{(M_z - M_o)k}{T_1}\right] \quad (3.8)$$

The first term describes the precessional motion and the second term describes the two relaxation processes. This is the well-known Bloch equation.

3.2.2 Principles of MRI

In MRI, the spatial resolution is introduced with the use of three magnetic field gradients, which are being superimposed to the uniform external magnetic field B_0. These gradients vary orthogonally among themselves in the x, y, z directions. In 2D MRI, which is the most common form of MRI, one of the field gradients (for example, G_z) is used for the slice selection, while the two other gradients (for example, G_x ad G_y) enable the 2D mapping. The Larmor frequency in an MRI experiment hence gains location-dependent terms due to the use of the imaging gradients, as

$$\omega = \gamma(B_o + G_x x + G_y y + G_z z) \quad (3.9)$$

In MRI, the signal is acquired in k space (spatial frequency); a 2D Fourier transform of the signal can produce an image in the reciprocal space. Two important parameters are TR and TE. TR is the repetition time, which is the time duration at which the pulse sequence repeats itself. TE is the echo time, which is the time duration between the initial excitation rf pulse (typically 90°) and the moment when the signal (echo) reaches maximum in acquisition.

3.2.3 T2 Relaxation Time

T2 relaxation describes the decay in the transverse magnetization M_{xy}, which can be defined through the Bloch equation as

$$M_{xy} = M_o e^{\frac{-t}{T2}} \quad (3.10)$$

where M_0 is the initial net magnetization as illustrated in figure 3.1a (Nishimura, 1996). To determine T2 relaxation experimentally, a delay time is varied in the pulse sequence; by plotting the exponential decay curve at various time points, the T2 relaxation time can be obtained from the fitting parameters (Hajidah & Dwihapsari, 2021). T2 is sensitive to the motion of water molecules, and can become anisotropic in biological tissues.

3.2.4 Spin echo sequence

Spin echo (SE) is the restoration of spin phase coherence after the signal appears to have lost coherence during the decay of the FID. In the pulse sequence, a 90° pulse tips the spins into the transverse plane, where the difference in local microscopic fields causes some spin groups to precess faster/slower hence gain/loss phase relative to the others. The spins gradually fan out as the arrows shown in fig 3.2, which results in a loss of the MRI signal. After a time period, a 180° pulse is applied that flips the precessing nuclear spins to the other axis according to the phase of the rf pulse. Since the direction of the precessing is not affected, the faster spins, which now lag behind in time, will catch up with the slower spins. After a time period that is equal to the time between the 90° excitation pulse and the 180° pulse, all spins converge and align again in the transverse plane, which forms the spin echo.

In addition to the T2 relaxation process, which is intrinsic to the spin system, the signal decay associated with the transverse spins can also be caused by several other factors, such as inhomogeneities in the external magnetic field. These additional decay factors cause the MRI signal to decay faster than due to the T2 relaxation alone. In this case, the signal decay is called T2* relaxation. The spin echo sequence is able to remove

the T2* dephasing, which allows T2 to be measured experimentally. The description of the timing and pulse and gradient application is shown in fig 3.3 (Jung & Weigel, 2013).

3.2.5 T1 and T1ρ relaxation times

T1 relaxation process describes the return of the excited spins back to the thermal equilibrium (which is along the longitudinal direction, z axis). This process involves energy exchange between the spins and the lattice and so is called the spin-lattice relaxation time. T1 can be determined as in fig 3.1b (Nishimura, 1996), based on the Bloch equation

$$M_z = M_o(1 - e^{\frac{-t}{T1}}) \tag{3.11}$$

T1ρ relaxation is called the spin-lattice relaxation in the rotating frame. In this situation, an rf pulse locks the transverse magnetization in the transverse plane, which generates another type of relaxation – due to the shrinkage of the magnetization magnitude in the transverse plane (Regatte et al., 2006). In biological tissues, it has been shown that T1 is insensitive to the anisotropic movement of water molecules in tissue (Xia, 1998) whiles T1ρ is sensitive to the slow-motion interaction between macromolecules and water (Regatte et al., 2006).

3.2.6 MRI Imaging Parameters

A number of experimental parameters in MRI are primarily important as they affect either the total exam time, signal-to-noise ratio (SNR), and contrast-to-noise ratio (CNR). From the imaging point of view, the parameter of resolution is the ratio of the field of view (FOV) in mm to the size of digital matrix.

$$\text{Resolution} = \text{FOV}/\text{Matrix} \tag{3.12}$$

A smaller FOV and large digital matrix both can improve the image resolution, at the cost of lower SNR and longer TE. In other words, a desire for better imaging resolution can cause the sequence to have longer TE (in the signal reading), a weaker signal, and a longer experimental time (due to more repetitions in the phase direction). Any determination of the experimental parameters in MRI is the consequence of careful analysis and compromises.

In a typical 2D MRI, the thickness of the imaging slice (slice thickness) is the size of the voxel in the slice encoding direction. Thicker slices increase the SNR and lower the resolution along that direction. Slice gap or spacing in multi-slice imaging is used in acquisition to reduce crosstalk artifacts caused by the excitation of neighboring slices. The number of averages (signal averages) taken during an MR acquisition increases the SNR but increases acquisition time. SNR is proportional to the square root of the number of averages.

3.3 Polarized Light Microscopy

PLM can be used to image structures and compounds that exhibit anisotropic properties, and has been used to visualize the architecture of fibrocartilage (Mantebea et al., 2021) and articular cartilage (Xia et al., 2001) in preclinical research studies. Structures of many connective tissues that are rich in collagen fibers (e.g., cartilage and tendon) show the characteristics of birefringence, which is the ability to transmit plane-polarized lights at different velocities and angles (azimuth) within the tissue (Wolman, 1975).

A polarizing light microscope has a light source and a condenser with a polarizer fixed between them. It also has a rotating stage to hold samples and the nosepiece for

adjusting objectives. When the light enters the optical axes of isotropic structures, the interaction is similar regardless of its crystal orientation. In anisotropic structures, however, the interaction is dependent on the orientation of the crystalline lattice with respect to the incident light. This causes the incident light to be diffracted into two rays at different velocities. The polarizer transmits the light before it passes through the specimen to generate two light-ray components that are at right angles to each other.

The two independent refractive indices of the anisotropic structure can be quantified in terms of their birefringence as

$$B = |n_{high} - n_{low}| \tag{3.13}$$

where B is the birefringence, and n is the refractive index. Due to the difference in refractive indices, one ray travels through the structure at a slower rate than the other ray. The slower ray is said to be retarded with respect to the faster ray, which can be quantified as

$$\Gamma = t * B \tag{3.14}$$

where Γ is the retardation, t is the thickness of the sample, and B is the birefringence. The light waves are transmitted through the specimen in various phases and combined through by the analyzer to produce high contrast image.

3.4 Technique for determining element composition

3.4.1 Inductively Coupled plasma (ICP)-optical emission spectroscopy (OES)

The ICP technique allows component elements of a sample to be determined using plasma and a spectrometer. The principle is based on the absorption of energy by electrons of atoms to an excited state and emitting rays at specified wavelengths as they return to a lower energy level. The source of the energy is heat from an argon gas plasma

with high electron density and temperature of 6000K to 10000K. The amount of light released at each wavelength is proportional to the number of atoms or ions making the transition (Hitachi hightech, n.d.). The light intensity of the wavelength is measured and with the calibration calculated into a concentration based on the Beer-Lambert law.

$$I = I_0 e^{-\mu x} \tag{3.15}$$

where I is the measured intensity, I_0 is the initial intensity, μ is the coefficient of absorption, x is the depth in meter

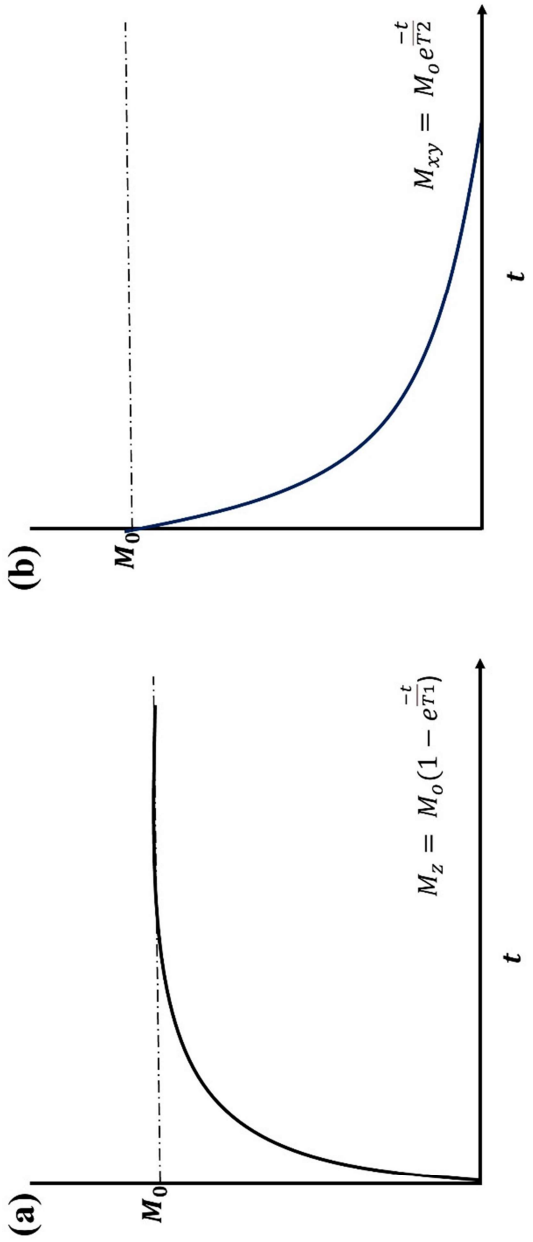

Figure 3.1 A) the regrowth curve for longitudinal magnetization to equilibrium magnetization M_o B) the exponential decay curve for transverse magnetization of T2 after excitation and

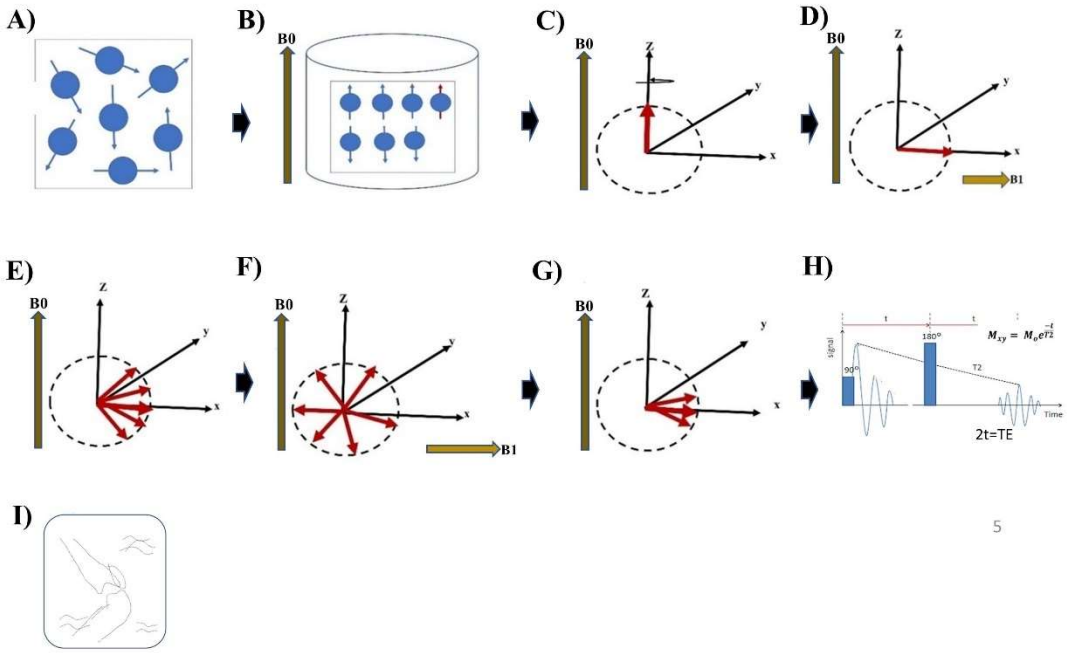

Fig 3.2 schematic representation of spin echo generated from sample a) with protons (spins) represented in blue. An application of external magnetic field B_o in b) causes protons to align parallel and antiparallel with excess protons in the direction of the B_o which results in a net magnetization vector M as represented with red arrow in c). Application of a B_1 field/pulse can tip M to the transverse plane d). When B_1 is switched off, the magnetization will return to equilibrium due to the T1 relaxation; at the same time, the spins dephase as in e) and f), which can be re-phased with 180˚ pulse in g). The signal from this relaxation time is measured as T2 (h) to produce an image i).

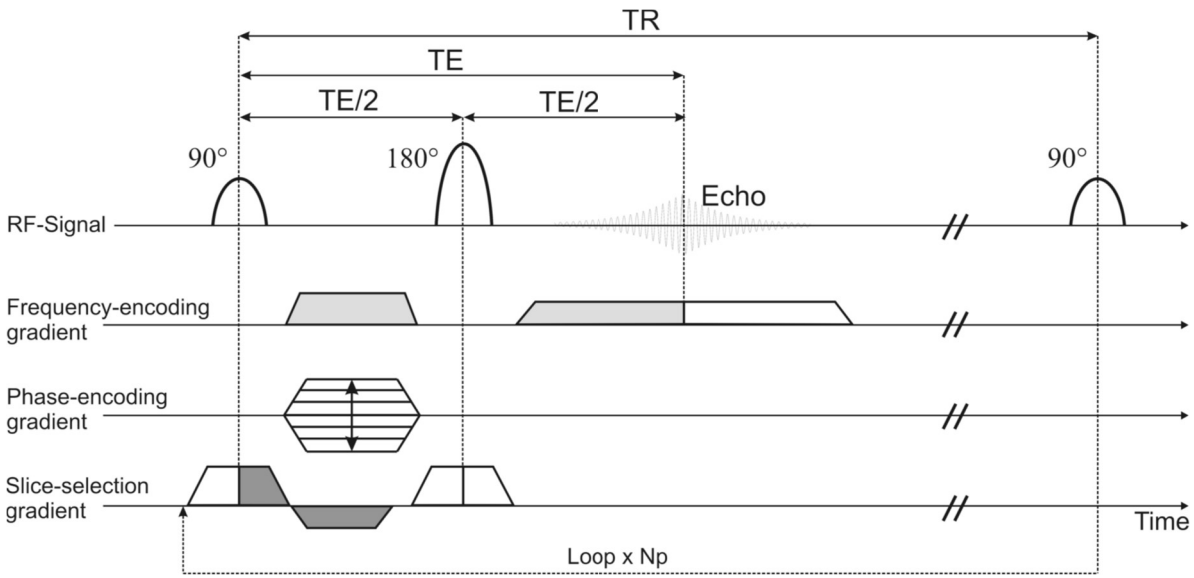

Figure 3.3 pulse sequence of spin echo (SE) showing the timings, pulses, and gradients involved. TR is the time it takes the whole cycle to repeat. (Reproduced with permission from Jung & Weigel 2013)

CHAPTER FOUR

STRUCTURAL MORPHOLOGY OF RABBIT PATELLA AND SUPRAPATELLAR CARTILAGE BY MICROSCOPIC MRI AND POLARIZED LIGHT MICROSCOPY

4.1 Introduction

The patella acts as a mechanical lever arm to improve extension capability of the quadriceps muscle through increment of the moment arm of the patellar tendon while shielding the tibiofemoral joint (Niu et al., 2017; Tecklenburg et al., 2006). The posterior aspect of the patella is the site for growth (Bland & Ashhurst, 1997) with the surface lined with cartilage. The cartilaginous surface can broadly be divided into two regions (medial and lateral) by a raised vertical midline ridge (Fox et al., 2012).

In studies of arthritis using rabbits (Arzi et al., 2015; Largo et al., 2010), its suprapatellar structure in the knee was often overlooked despite its prominence and contribution (Tischer et al., 2002). The suprapatella in rabbits is a sesamoid fibrocartilage found in the deep surface of the quadriceps tendon (Ralphs et al., 1992) and proximal to the patella. It forms an essential part of the knee joint as it articulates with the femur. Similar to articular cartilage, the suprapatella is known to contain aggrecan, type II collagen, and glycosaminoglycan (Tischer et al., 2002). As fibrocartilage, the suprapatella is also affected in degenerative joint disease (Benjamin & Ralphs, 1998) and for an extremely flexed knee, the suprapatella is a weight-bearing structure in the knee joint (Tischer et al., 2002). To appreciate the roles articular cartilage of sesamoid bones and sesamoid fibrocartilage play in pathology and biomechanics, it is important to understand the molecular and fibril structures of the patella cartilage and suprapatellar- the former is extensively used as a model for cartilage repair and the latter is subject to

degenerative change in osteoarthritis (Tischer et al., 2002). Patellar cartilage of rabbits is known to behave differently from other species due to the difference in response to damage and healing (Athanasiou et al., 1991; Wang & Xia, 2012; Xia et al., 2001; Xia & Zheng, 2010). So far, there is also a lack of sensitive markers in detecting critical changes when assessing the structural and biochemical properties of patella cartilage and suprapatellar tissues (Wang & Xia, 2012).

The study in this chapter aimed to provide both quantitative and qualitative structural and morphological characterization for rabbit patella cartilage and suprapatella at high resolutions using microscopic MRI (μMRI) and polarized light microscopy (PLM). Whole-body MRI is valuable in the clinic for detecting degradative variations in the molecular environment of biological tissue and organ noninvasively. Available at a transverse resolution down to about 10 μm, μMRI is extremely useful in the quantitative examination of connective tissues such as articular cartilage at high resolution (Xia, 1998). The μMRI technique can assess the depth-dependent anisotropic morphology in articular cartilage non-destructively (Wang & Xia, 2012). In particular, the T2 relaxation time, which can be quantified in both clinical MRI and μMRI based on the same physics principles, is sensitive to the orientation of collagen fibrils and the proteoglycan-water interactions depth-dependently in cartilage (Wang & Xia, 2012; Xia, 1998). The T2 anisotropy protocol was used in this study for the first time to study the suprapatellar of the rabbit. The non-invasive characterization of these tissues by μMRI is correlated in this study with the quantifiable information by PLM on the angle (representing the pixel-averaged orientation of collagen fibers) and retardation (representing the pixel-averaged organization of collagen fibers) in cartilage (Xia et al., 2001).

4.2 Materials and Methods

4.2.1 Sample Preparation for Patella and Suprapatella

The patella and suprapatella were obtained from the left hind limbs of five 12-15-weeks-old male New Zealand white rabbits. The rabbits were healthy and sacrificed for an unrelated experimental study (which was approved by the relevant Institutional Review Committee); the intact bodies were frozen at -80˚C and later thawed at 4˚C before harvesting. Four intact knee joints were placed individually in a glass tube for the low-resolution MRI axially centered at the patellofemoral region.

Four patellar cartilage blocks, one from each rabbit, were cut from the central and medial parts of the tissue, which had a size of 4 x 3 x 2 mm and included the full depth of tissue and underlying bone. A medial section was taken because in deep flexion the patella tilts medially, i.e., more surface contact with the medial condyle (Moro-oka et al., 2002). Each block was sealed in a 5 mm glass tube containing saline with protease inhibitor. In addition, four randomly selected suprapatella from the five rabbits with the full thickness of tissue still attached to a part of the underlying quadriceps tendon were excised. Each sample was placed in a 5 mm glass tube without saline. Both patella and suprapatella were imaged in the sagittal view in μMRI and later prepared for histology. (Xia et al., 2008; Xia & Zheng, 2010)

4.2.2 Microscopic MRI Protocol

A Bruker Avance III HD 300 NMR spectrometer was used to image all specimens, which has a 7-Tesla 89-mm-bore-diameter superconducting magnet. A quantitative T2 magnetization-prepared imaging sequence (Xia et al., 2008) was used. The sequence has a leading segment for relaxation weighting by a spin-echo and a

subsequent MSME (multi-slice multi-echo) imaging segment where all timings were kept constant (Xia, Alhadlaq, et al., 2008; Xia & Zheng, 2010). The intact joint imaging used a field of view (FOV) of 25 x 25 mm, a slice thickness of 0.8 mm, and a matrix size of 256 x 256 with five echo times (8, 16, 24, 32, 40 ms). The cartilage blocks were imaged with a FOV of 5 x 5 mm and a matrix size of 256 x 128, which was later reconstructed into the size of 256 x 256 in ImageJ (v1.52a). These imaging parameters resulted in a pixel resolution of 97.6 μm per pixel for the intact joint and a higher resolution of 19.5 μm for the cartilage blocks. A TR (repetition time) of 2 s was used in both imaging experiments. For the patella cartilage blocks, the TE (echo time) in the contrast segment for the T2 weighting was 2, 4, 8, 16, and 38 ms. The normal axis to the cartilage surface in the bone blocks was placed at 0˚ and 55˚ angular orientations with respect to the external magnetic field B_0, which manipulated the geometrical factor $(3\cos^2\theta - 1)$ that dominates the non-zero dipolar Hamiltonian (Xia, 1998). The suprapatella was imaged with similar parameters without the use of saline (otherwise it would be difficult to separate the saline from the tissue in the quantitative calculation). For suprapatella, the echo times used in the T2 weighting were 2, 4, 8, 10, and 12 ms. (We optimized each set of echo times in quantitative imaging for each type of tissue.)

4.2.3 PLM Protocol

After the MRI experiments, the suprapatellar tissue and the patellar cartilage blocks used in MRI were fixed in 10% neutral buffered formalin at 4˚C. These specimens were sent to an external facility for histological processes (Yale Pathology Tissue Services, New Haven, CT). Sections from the MRI imaged specimen were made such as to coincide with the slice-selected region of the specimen during the MRI scan.

Additional whole length-wise and width-wise sections from the cartilage bone plugs and length-wise sections from suprapatellar tissue were prepared.

The PLM system used in the study was a digital CCD camera that is mounted on a polarized light microscope (Leica, Germany). The output of the CCD camera generated two quantitative images, the optical retardation and the angular orientation (Oldenbourg & Mei, 1995). The tissue sections were imaged at three optical resolutions: under an objective of 2.5x resulting in a 4.0-μm pixel size for the whole specimen, under an objective of 10x resulting in a 1.0-μm pixel size for the small specimens, and under an objective of 40x resulting in a 0.25-μm pixel size for detailed examination of cellular features. In total, about 15 patellar cartilage sections (3 from each sample), 3 whole lengths and width (each patella section), 12 width-wise and 3 length-wise suprapatellar sections were imaged with PLM.

4.2.4 Data Analysis

2D images from the patellar cartilage blocks and the suprapatellar fibrocartilage tissues were used to examine the results from both MRI and PLM. From each 2D image, a rectangular region of interest (ROI) was selected in the tissue to extract 1D depth-dependent cross-sectional profiles. The ROI was taken at approximately the same location in both PLM and MRI images. The width of the ROI for the intact joint was chosen such that the tissue thickness matched that of the cartilage blocks. Public-domain software ImageJ (v1.25a) and commercial software KaleidaGraph (v4.5.4) were used in the analysis with no manual scaling and adjustment during the averaging of the data.

4.3 Results

4.3.1 Physical Observation

Fig 4.1a shows a photo of the intact posterior aspect patella and suprapatella that articulate with the anterior aspect of the femur, where the suprapatella (which appeared white to pinkish colored) is positioned above the base of the patella. The lateral aspect of the patella was slightly raised as compared to the medial and was consistent in all rabbits. The approximate measurement for the flipped triangular-shaped patella was 10 x 8 x 4 mm (length x width x thickness) taken at the widest points (Fig 4.1c). Similarly, the suprapatella consistently appeared to have an elongated-oval bulging shape with approximate dimensions of 9 x 6 mm (major x minor axis) (Fig 4.1b). The suprapatellar was observed to have tougher cartilage.

The whole suprapatellar fibrocartilage and patellar cartilage cut centrally widthwise are shown in Fig 4.1d and Fig 4.1e as viewed by an optical microscope, while a medial cut lengthwise for the cartilage are shown as PLM images in Fig 4.1f and Fig 4.1g. The patellar cartilage had a slight thickness variation along the width, with a thicker tissue in the medial aspect as compared to the lateral side. Lengthwise, the patellar cartilage had an insignificant variation of thickness except for the apical region with highly packed chondrocytes. The thickness of the suprapatellar fibrocartilage decreased proximally away from the patella.

4.3.2 MRI Results

Fig 4.2a shows five MRI T2-weighted intensity images of the axial and sagittal view of the intact knee joint at 97.6-μm resolution. The axial view in Fig 4.2a shows both medial and lateral aspects of the cartilage and its attachment to the sesamoid bone. Both

the medial and lateral posterior aspects were seen to be slightly convex to almost flat, which were consistent in all rabbits. The medial side was just slightly longer than the lateral side with homogenous cartilage signal intensity. The suprapatella with its attached tendon was visualized on the sagittal view in Fig 4.2a as a thin white streak bounded posteriorly by the tendon and a fat pad anteriorly. Fig 4.2b shows a patellar cartilage block at a higher resolution at different echo times. In all four patellar blocks, a tri-laminar appearance of the articular cartilage (Xia et al., 2001) was observed at an orientation 0˚ to the magnetic field B_0 (which is vertically up), which disappeared at the magic angle (55º to B_0) (Xia, 2000b). The fibrocartilage in Fig 4.2c demonstrated a more homogeneous and higher intensity compared to its underlying tendon. Quantitative T2 maps were calculated for both types of cartilages (the furthest right image on each row). The T2 image of the fibrocartilage (Fig 4.2c) had a dark thin line on the surface.

Quantitative 1D T2 profiles were calculated from the 2D images and shown as a function of tissue depth in Fig 4.3. In patellar cartilage (Fig 4.3a and 4.3b), the asymmetrical bell-shaped curve of articular cartilage was visible only at the high resolution when the tissue was oriented at 0˚ to the magnetic field, confirming the characteristics from previous studies (Xia, 1998; Xia et al., 2001). The comparison between the low- and high-resolution profiles in patellar cartilage (Fig 4.3a) shows the lack of tissue features in the low-resolution imaging. Based on the high-resolution profiles and the established divisional criteria (Xia et al., 2001), we determined the thicknesses of the three structure zones in patellar cartilage as, the superficial zone from 0 to 20 μm, the transitional zone from 20 to 60 μm, and the radial zone from 60 to 440 μm. Table 4.1 and Table 4.2 summarize the average zonal thicknesses of patellar cartilage and

the zonal averaged T2 relaxation times. In contrast, the T2 profiles of the suprapatella cartilage at high resolution (Fig 4.3c) show a lack of the magic angle effect for the upper half of the tissue (i.e., the 0˚ and 55˚ profiles were similar), and some weak T2 anisotropy for the lower half of the tissue (i.e., the 0˚ and 55˚ profiles were different). Based on the T2 characteristics, the suprapatella cartilage seems to have a thin surface layer that covers the much thicker main tissue of about 390 μm in thickness.

4.3.3 Quantitative Morphology by PLM

2D quantitative maps of angle and retardation in the patellar cartilage and sesamoid fibrocartilage were obtained and analyzed for all histological sections. Fig 4.4a shows one set of quantitative images for a patellar specimen at 1.0 μm pixel resolution. Several features can be identified. For example, the commonly known 90º difference between the surface cartilage and the deep tissue was observed in the angle map of the patella cartilage. The 0˚ angle (blue color) in the superficial zone corresponds to the parallel orientation of the surface collagen with the articular surface. The collagen fibers change their orientation in the transitional zone, and reach the 90˚ values of angles (red color) in the radial zone, suggesting the perpendicular orientation of the fibers in the radial zone. The retardation image from the patellar cartilage in Fig 4.3a shows the prominence of chondrocytes in the tissue, with their orientations clearly changed from being parallel to the articular surface in the surface tissue to more random and in clusters in most of the deep tissue (Xia et al., 2001). The location of the minimum values of the retardation indicates the center of the transitional zone where the fibers are mostly random between two peripheral zones that have a nominal 90˚ orientation difference. The minimum retardation in the patella cartilage was 2.2±1.2 nm. Finally, the retardation and

angle images in some other animal models (such as canine) contain a recognizable feature that has been attributed to the tide mark (the mineral front) (Xia et al., 2001). In the rabbit patellar cartilage, the quantitative images did not contain such a feature, which may indicate insufficient infusion of minerals in these 12-15-week-old rabbits.

Fig 4.5a shows a set of quantitative images for one sesamoid fibrocartilage specimen at 1.0-μm pixel resolution. Several observations can be made from these quantitative PLM images. First, the top 10 μm of the sesamoid fibrocartilage can be viewed as the surface layer (or skin) of the fibrocartilage, which has some considerable portion of the collagen fibers being oriented in parallel with the surface of sesamoid fibrocartilage (as in the line drawings on the furthest right of Fig 4.5a). Below this organized layer, the quantitative values in most of the fibrocartilage have large variations, in contrast to the consistent zonal values in the PLM images for patellar cartilage. The retardation values for most of the non-surface fibrocartilage varied around 1 nm, indicating the lack of a coherent fibril organizational structure.

Fig 4.6 shows PLM images of the same tissue regions at 0.25-μm pixel resolution, where each image was pieced together by several high-resolution images due to the smaller field of view. At this resolution, the cellular orientations in both tissues can be examined. Two major structural differences between these two types of cartilage tissue can be noted. First, the patella has a well-defined three-zone structure while the suprapatella has an ill-defined interface between its surface layer and the main tissue. Second, patellar cartilage has rather a uniform fibril density, while the heterogeneity in the fibril density in suprapatellar cartilage is recognizable, likely indicating the loose packing/formation of individual collagen bundles.

The average thicknesses for both tissues from all histological sections were measured and shown in Table 4.3. For the patellar cartilage, the zonal division was carried out based on the criteria defined by a previous study (Xia et al., 2001). For the suprapatellar fibrocartilage, only the total tissue thickness was measured from 2D images in both PLM and μMRI images. Note that the statistical comparisons between the two imaging techniques are influenced by the imaging resolutions.

4.4 Discussion

The degradation of patellar cartilage is one of the most common issues for osteoarthritic deterioration in the knees (Kim & Joo, 2012; Samuels et al., 2017). The extracellular matrix in the patella composes mostly of two macromolecules (glycosaminoglycan, collagen), together with water (Mow et al., 1980). The fibrillar collagen in the patellar cartilage in rabbits is of type I, II, III, and V, with distributions that vary with age (Bland & Ashhurst, 1997). In contrast to the presence of patellar cartilage in knee joints of both animals and humans, the sesamoid fibrocartilage is not present in human knees but in some other joints of humans such as the ankles (in Achilles tendon alongside the calcaneus). Histochemistry has shown that both types of cartilage have similar chemical properties (Tischer et al., 2002). The decrease in thickness of the suprapatella proximally results from reduced compression toward the ends of the vastus intermedius and rectus femoris muscle and away from the knee joint. This imaging study focused on patellar cartilage and suprapatellar cartilage in young rabbits, in order to understand the wide range of disorders associated with the patellofemoral regions associated with arthritis. Two different imaging techniques were used, MRI and PLM, which measure different aspects of the same tissue. MRI T2 anisotropy is sensitive to the

mobility of water molecules in tissue, which is modulated by the interactions between water and macromolecules via the dipole interaction and chemical exchange. In contrast, quantitative PLM is based on optical birefringence, which in cartilage measures the fibril orientation (angle) and fibril organization (retardation). MRI T2 anisotropy and PLM parameters offer complementary information to the micro-structures of cartilage and other connective tissues.

4.4.1 Patella

The results of μMRI and PLM show that the patellar cartilage in rabbits has a morphological structure similar to articular cartilage in some other animals such as canine (Wang & Xia, 2012), which can be divided along its thickness into three distinctly different histological zones. The superficial zone has its collagen fibers in parallel with the articular surface; its strong T2 anisotropy (Fig 4.3b) and the high values in the PLM retardation (Fig 4.4b) suggests the SZ fibers are densely packed. This parallel arrangement of the surface fibers helps in easy sliding between itself and the opposing surfaces of the femur cartilage. In the transitional zone, the randomness of the collagen fibers results in its higher T2 values and lower T2 anisotropy, which yields the T2 peak at the 0˚ orientation (Fig 4.3b). This randomness gives the minimum retardation for the tissue, centered around 50 μm below the articular surface in rabbit tissue. In the radial zone of the patellar cartilage, the collagen fibers are arranged perpendicular to the articular surface; its strong T2 anisotropy and low T2 values for most of the radial zone again suggest a densely and well-arranged fibril organization. However, its retardation increases nearly linearly from the min value in the middle of the transitional zone to a max value near the cartilage-bone interface (Fig 4.4b). This linear increment in the

retardation suggests that although the overall organization of the collagen fibers in the radial zone stays consistently perpendicular to the articular surface throughout the entire radial zone (Fig 4.4b), the coherence of this perpendicular fibril organization increases gradually over the thickness of the radial zone, from the most random organization in the transitional zone to the most coherent organization near the cartilage-bone interface. This three-zone arrangement of the fibers in the non-calcified cartilage helps the tissue to withstand the load pressure from the femur and the sesamoid bone.

4.4.2 Suprapatella

In contrast to the triple structural zones in the patellar cartilage, the suprapatella only has two layers of tissue; a thin surface layer (~ 10 μm thick) and a much thicker main tissue. For the superficial layer of suprapatella, although MRI results showed a lack of articular-cartilage-like anisotropy (Fig 4.3c), it is likely caused by its thinness (~ 10 μm), which is difficult to measure even with our μMRI resolution (19.5 μm). The quantitative PLM profiles of the surface layer (0-10 μm in Fig 4.5b) are similar to those of the patellar cartilage, with a retardation peak around 5 μm below the suprapatellar surface. Therefore, together with the short T2 values in the surface layer (Fig 4.3c), we can conclude that the collagen fibers in the surface layer of suprapatella are well organized, dense, and in parallel with the surface. This structured surface layer of suprapatella likely aids in the reduction of friction when the surface slides with the femur cartilage. Our observation from the suprapatella results was in agreement with the qualitative study by Tischer et al. (Tischer et al., 2002), who observed that the suprapatella has a thin layer of tissue with cells organized parallel to the articular surface basket and weave-like collagen fibers.

The majority of the suprapatella is its main tissue body, where the T2 values in μMRI are consistently high and have no orientational dependence in the magnetic field for the top half of the tissue (Fig 4.3c). This lack of strong T2 anisotropy suggests that the majority of the suprapatella fibers must have a close-to-random and loose-packed pattern, similar to the transitional zone of the patella. Its much-higher T2 values in most of the suprapatella tissue imply little dipolar interaction and abundant water molecules. However, based on the localized pixel averaging over the tissue depth, the collagen fibers in the majority of the suprapatella cartilage maintain an overall orientation that is perpendicular to the suprapatella surface (Fig 4.5b). In the lower part of the suprapatella (c.f., over 300 μm in Fig 4.5b) when the fibers get imbedded into the quadriceps tendon, the collagen fibers of the suprapatella have increased retardation (i.e., better organized) and a reduction of the orientation (i.e., change of the orientation). The random arrangement offers flexibility to the suprapatella cartilage and allows it to withstand stress from the quadriceps tendon during flexion, while at the same time reducing pressure load from the femur.

Note that since fibrocartilage in saline produced insufficient MRI contrast, the fibrocartilage was imaged in air. Given the fact that the fibrocartilage is tough and the tissue blocks were large and intact (not pieces), our specimens did not dry out at the end of imaging experiments. However, imaging the fibrocartilage in the air did have some consequences. The beneficial consequences were the ability to locate the surface accurately and a reduced partial volume effect (among tissue and saline) in the quantitative calculation. The adverse consequence could come from the magnetic susceptibility difference between air and liquids, which could affect the accuracy of T2

for the surface pixel. Our choice in imaging protocols was supported by the agreement between our μMRI and PLM results for the surface part of fibrocartilage.

4.5 Limitations in μMRI resolution

As the morphological structure becomes smaller, it becomes challenging to measure it accurately even with the fine resolution in μMRI. Using articular cartilage from canines, which was about twice as thick as cartilage in rabbits, we showed in several publications that the zonal thicknesses by μMRI are statistically significantly correlated with the zones by PLM. Using articular cartilage from rabbits, we noted recently that the thickness measurements of the thin zones (SZ and TZ) can be different between μMRI and PLM; we concluded that this difference "is likely caused by the difference in the imaging resolution (9.75μm in μMRI, 1.0μm in PLM). However, the correlations in the total tissue thickness and the thick radial zone are excellent (i.e., no statistical difference between μMRI and PLM zones were found)." In this study, we also observed thickness differences measured by μMRI and PLM (Table 3). Due to a finer resolution and a thin slice, the SZ and TZ measurements by PLM are considered to be accurate.

4.6 Conclusion

To the best of our knowledge, this was the first quantitative imaging study that characterized the morphological structures of articular cartilage in the patella and sesamoid fibrocartilage in the suprapatella of the rabbit quantitatively and at high in-plane resolutions. Certainly, these two different types of cartilage play different roles in joint motion biomechanically. Despite the thinness of these rabbit tissues, the high spatial resolutions in our μMRI and PLM are sufficient to resolve the depth (i.e., thickness) dependent tissue properties (Batool et al., 2020). The quantitative nature of the results

was used to explain the morphological structures of the tissues. The articular cartilage behaved similar to other hyaline cartilages, with three clearly distinguishable structural zones. The fibrocartilage had a thin surface layer that covers the rest of the tissue body, which has mostly random organization of collagen fibers hence no relaxation anisotropy in μMRI. The quantitative nature of our μMRI and PLM imaging provides an important set of baseline characteristics to future studies of arthritis research using animal models.

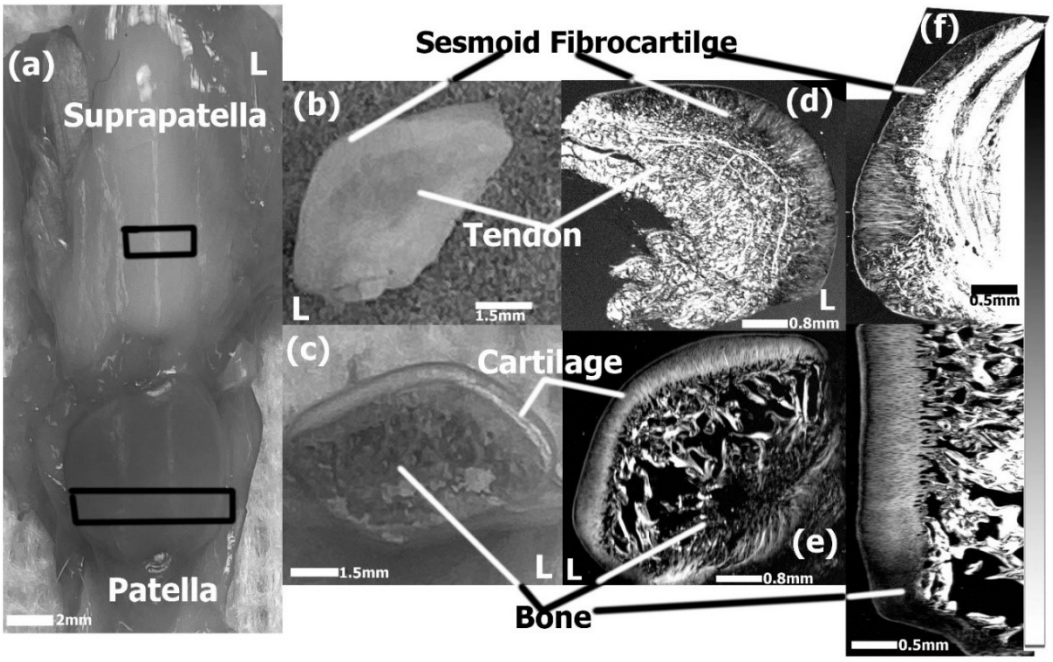

Figure 4.1 (a) A posterior view of opened knee joint, showing the suprapatella and patella. The rectangular boxes show the locations where the specimens were taken for μMRI (patellar cartilage) and PLM (both types of cartilage). (b) and (c) were the photos of a whole cross-sectional cut of suprapatella and patella, which were imaged under PLM as in (d) and (e) respectively (objectives: 2.5x and 1.25x). PLM images of a longitudinal histological cut of suprapatella (f) and patella (g), both with a 2.5x objectives. (L: lateral)

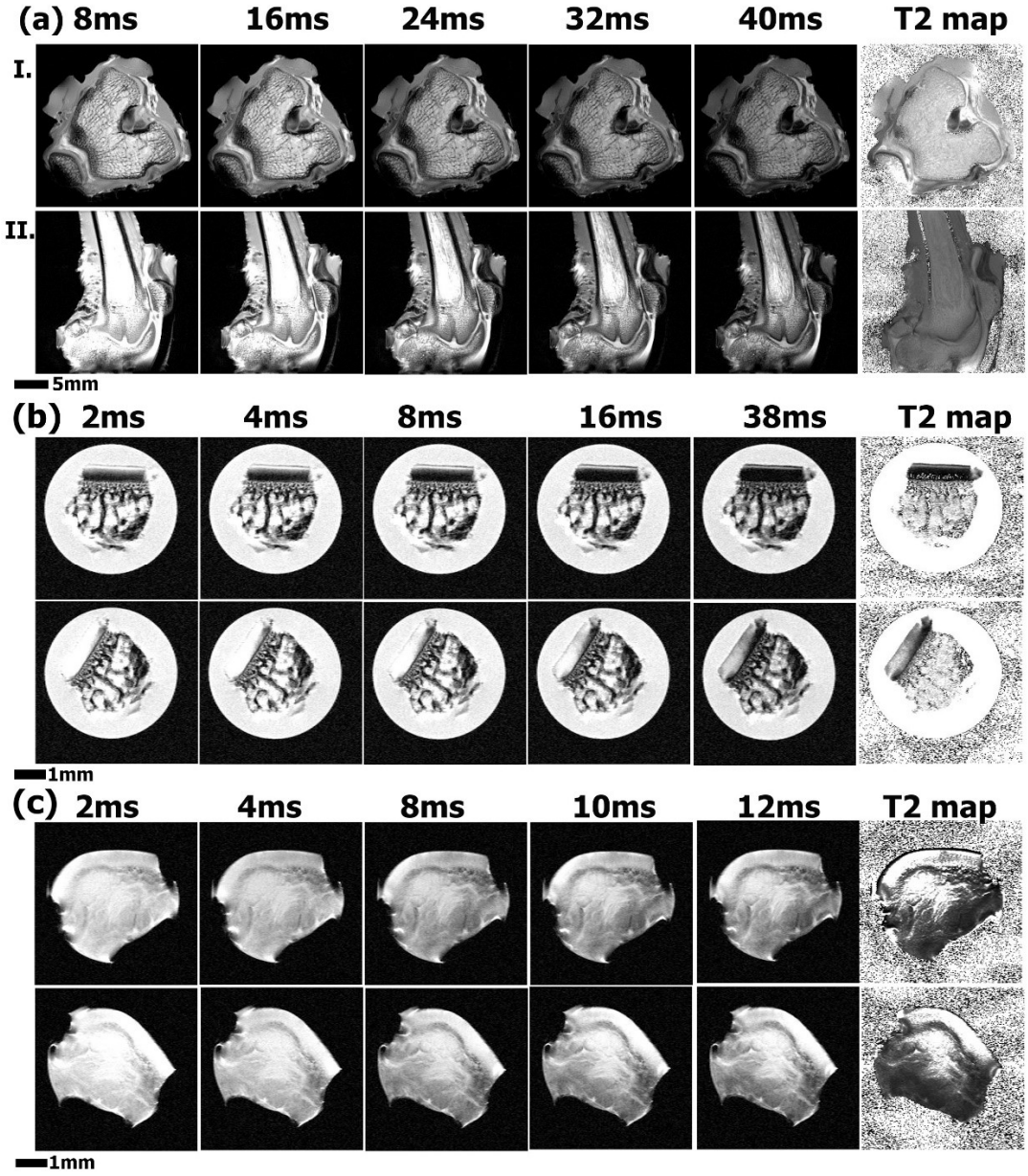

Figure 4.2 (a) T2-weighted intensity images for both axial and sagittal views of an intact knee joint, showing the patellofemoral joint at different echo times, with a pixel resolution of 97.6 μm. (b) and (c) are T2–weighted intensity images with a 19.5-μm resolution for patellar cartilage and suprapatellar fibrocartilage respectively, with two orientations of the specimen at 0º and 55º to the magnetic field B_0 (vertically up). All intensity images were displayed using the same upper and lower thresholds. The furthest right image in each row is the quantitative T2 image calculated based on the intensity images, in-unit of ms.

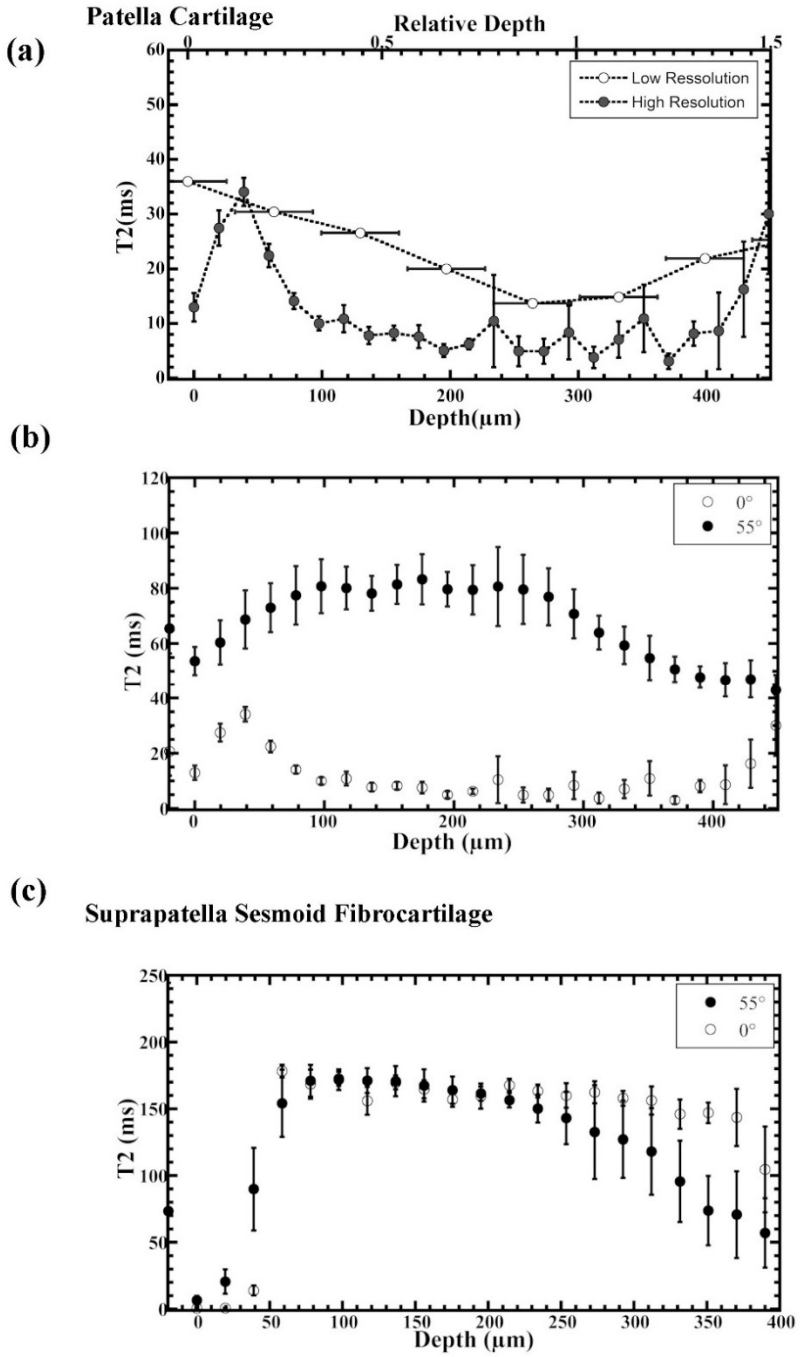

Figure 4.3 (a) The depth dependent T2 profiles for patellar cartilage at the pixel resolutions of 97.6 μm and 19.5 μm. (b) The depth dependent T2 profiles for patellar cartilage at the pixel resolution 19.5 μm between two orientations in the magnetic field. (c) The depth dependent T2 profiles for suprapatellar fibrocartilage at 19.5 μm/pixel. The horizontal bars in (a) represent the pixel size in the low-resolution MRI. The solid and open dots in (b) and (c) represent specimen orientations at 55º and 0º, respectively.

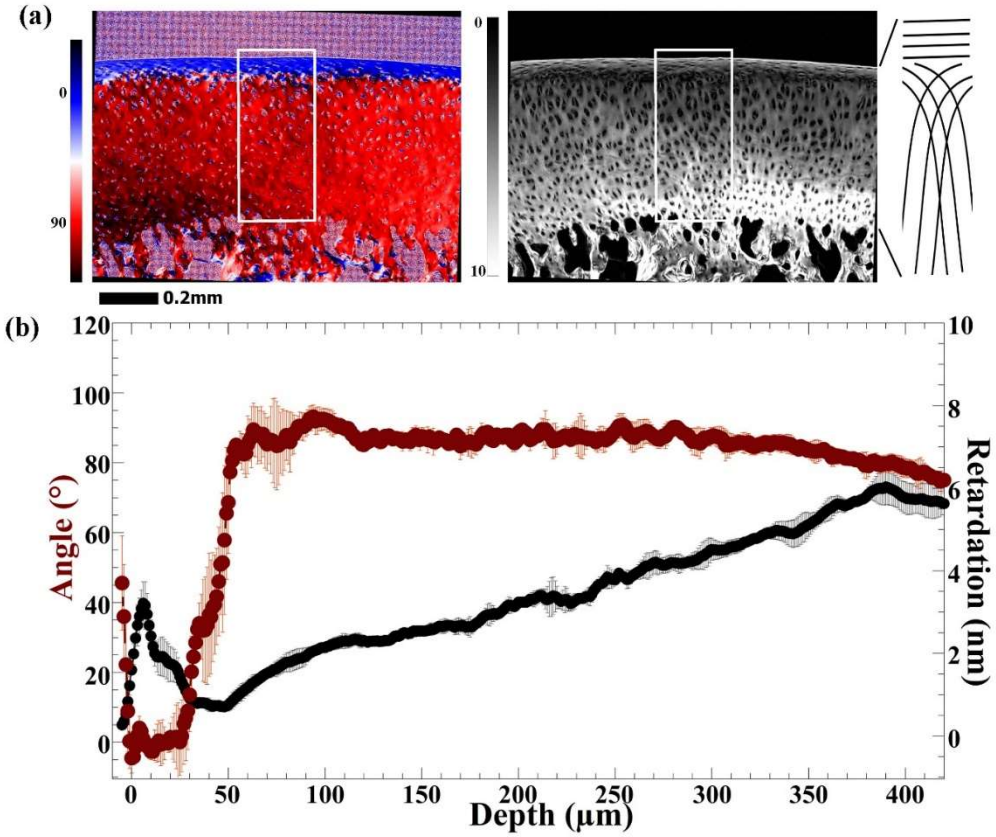

Figure 4.4 Quantitative PLM of patellar cartilage (a) 2D angle and retardation images at 1-μm pixel resolution, with its associated depth-dependent profile results in (b). The black oval-shaped dots in the retardation image are the locations where the chondrocytes in the cartilage used to exist (the cells were not histologically preserved). The red and blue colors in the 2D quantitative angle image demonstrate the perpendicular orientations of the collagen fibers between the superficial and radial fibers, at approximately 0º and 90º. The greyscale 2D image is the quantitative retardation, from 0 nm (black) to 10 nm (white). The rectangular boxes in the images show the locations where the depth-dependent profiles were taken. The schematic drawing next to the images is the interpretation of the quantitative results.

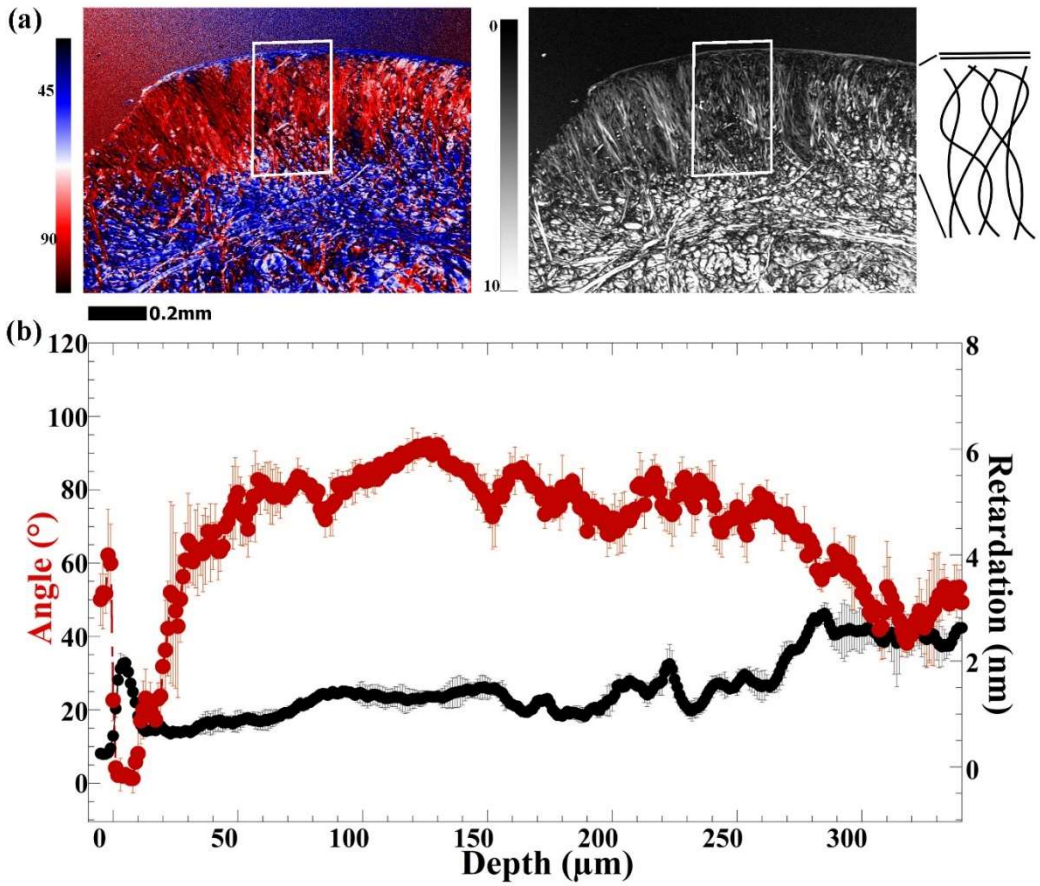

Figure 4.5 Quantitative PLM of suprapatellar fibrocartilage, (a) 2D angle and retardation images at 1-μm pixel resolution, with its associated depth-dependent profile results in (b). The scales in (a), are identical to those in Fig 4.4. The rectangular boxes in the images show the locations where the depth-dependent profiles were taken. The schematic drawing next to the images is the interpretation of the quantitative results.

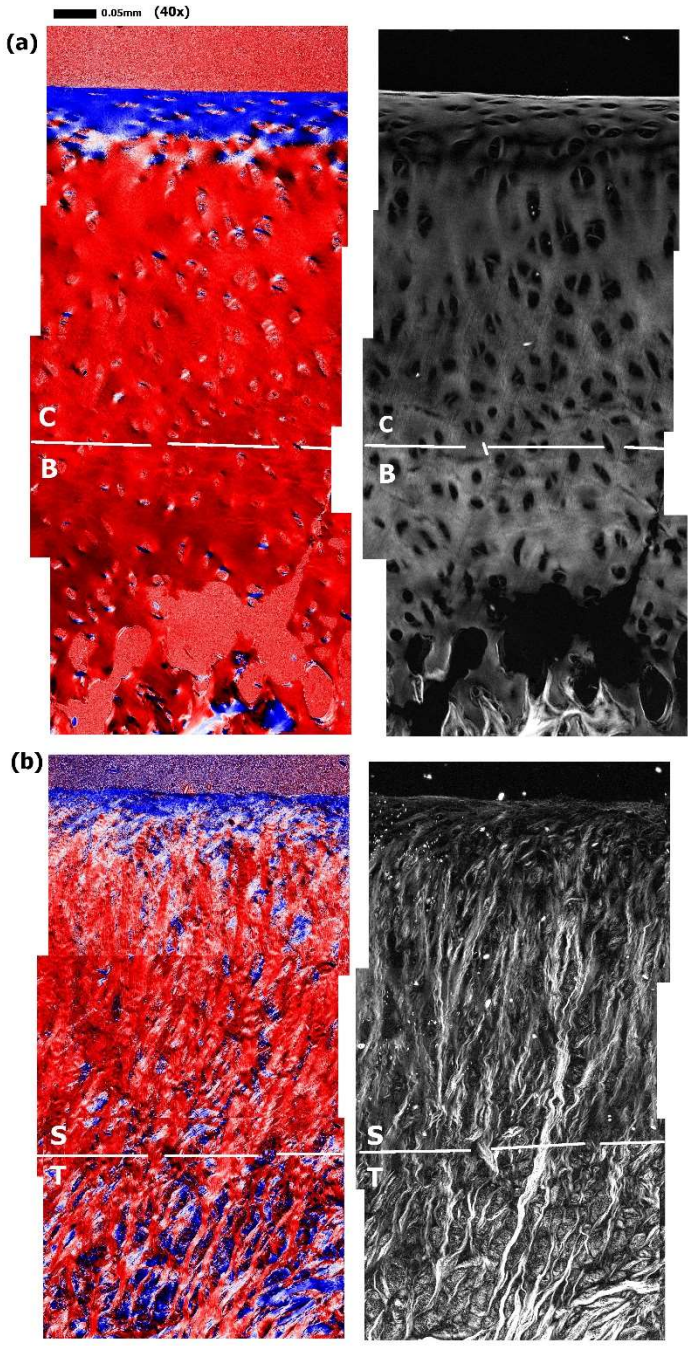

Figure 4.6 Quantitative PLM images of patella (a) and suprapatellar fibrocartilage (b) at 0.25-µm pixel resolution. The display thresholds of these images are identical to the images in Fig 5a and Fig 5b. (C cartilage, B bone, S suprapatella, T tendon)

Table 4.1 Zonal thicknesses of patellar cartilage (n = 4 specimens), where the division was based on the T2-0° profiles of patellar cartilage.

Specimen	Superficial Zone (μm)	Transitional Zone (μm)	Radial Zone (μm)	Total Thickness (μm)
LP 16	19.5	39.0	312.0	370.5
LP 18	39.0	39.0	331.5	409.5
LP 19	19.5	39.0	331.5	390.0
LP 23	19.5	58.0	331.5	409.0
Mean ± σ	24.4 ±4.9	43.8 ± 4.8	326.6 ± 4.9	394.8 ± 9.3
%	6	11	83	100

σ represents the standard error. % is the relative percent thickness of each zone based on the total thickness.

Table 4.2 Zonal averages of T2 relaxation values in patellar cartilage.

	T2 (ms) ± σ	
	0 ˚	55 ˚
SZ	20.76 ± 5.26	53.35 ± 9.65
TZ	38.51 ± 5.01	62.60 ± 6.80
RZ	11.7 ± 3.07	58.51 ± 7.93

Table 4.3 Correlations of (a) the averaged zonal thicknesses of patellar cartilage between μMRI (n = 3 specimens) and PLM (n = 9 histological sections from 3 μMRI specimens at 3 sections per specimen) and (b) the averaged total thickness of suprapatellar fibrocartilage based on direct approximated measurements from 2D images of μMRI (n = 3 cartilage specimens) and PLM (n = 9 histological sections from 3 μMRI specimens at 3 sections per specimen). In both cases, statistical comparisons using the t-test were performed.

Zone	μMRI (μm)	PLM (μm)	t-probability
(a) Patellar cartilage			
SZ	26.0 ± 6.5	41.2 ± 5.6	0.15
TZ	39.0 ± 0.0	38.0 ± 10.3	0.95
RZ	325.0 ± 6.5	371.4 ± 56.7	0.46
Total Tissue Thickness	390.0 ± 11.3	451.1 ± 66.2	0.47
(b) Suprapatellar cartilage			
Total Tissue Thickness	384.3 ± 20.4	377.2 ± 49.7	0.90

Data is in mean ± standard error confidence interval of 95%

CHAPTER FIVE

STRUCTURAL DIFFERENCES BETWEEN IMMATURE AND MATURE ARTICULAR CARTILAGE OF RABBITS BY MICROSCOPIC MRI AND POLARIZED LIGHT MICROSCOPY

5.1 Introduction

The rabbit cartilage has structural similarities to human cartilage and bridges the gap between small and large animal models required for preclinical research (Kingfisher, Volume 1 No. 2). The collagen fibers are the most abundant macromolecule in cartilage and defines the depth-dependent ultrastructure of the tissue (Shah et al., 2007). The chondrocytes are resident cells that play an exceptional role in the maintenance, repair, and development of the ECM (Levin et al., 2005). Through specific biologic activities of the chondrocytes, there is the growth of articular cartilage in distinct regions of the tissue, which may be mediated through an increase in matrix volume fraction or an increase in cell volume fraction by proliferation or hypertrophy (Jadin et al., 2005; Williams et al., 2008).

In this study we utilized MRI which is able to generate sufficient resolution to detect localized lesions at different depths of cartilage (Wang et al., 2015). Microscopic MRI (μMRI) was used to assess the articular cartilage at high resolution (Wang & Xia, 2012). The imaging pulse sequences used in this study were able to quantify T2 and T1ρ relaxation at microscopic resolution. T2 relaxation measured the decay in phase coherence among the nuclear spins in the transverse plane. T1ρ measured the reduction of the macroscopic magnetization when it is locked along a transverse axis, and is sensitive to slow-motion interactions between water and macromolecular proteins in biological tissues (Wang & Xia, 2012). In addition to the noninvasive imaging by μMRI, PLM was

used to study the cartilage at relatively higher resolutions, which provided quantifiable information on the cartilage tissue optical retardation and angular orientations (Xia et al., 2001).

The study in this chapter aimed to compare mature and immature articular cartilage quantitatively and qualitatively using different imaging techniques. Since the biomechanical properties of cartilage are maintained mostly by the ECM, tissue maturity is a significant factor that affects the biomechanical and biochemical properties of articular cartilage (Levin et al., 2005), which differ from fetal development to skeletal maturity (Xia. et al., 2016). It is, therefore, important to know the structural features of cartilage during different stages of its growth and development. We used rabbit cartilage from shoulder (humerus) and knee (femur) joints in this study.

5.2 Materials and Methods

5.2.1 Sample Preparation

Shoulder and knee joints were obtained from New Zealand white rabbits sacrificed from an unrelated biomedical study (the uses of animals were approved by the relevant institutional review committees). The intact carcasses were frozen immediately after sacrifice at -80 ˚C and later thawed at 4 ˚C before the joints were excised. Three immature rabbits aged 3–4 months and three mature rabbits aged 12–18 months were used in the study. From each animal, two cartilage-bone specimens were harvested from both a humeral head (Fig 5.1a) and a femoral condyle (Fig 5.1b), which gave the total number of specimens of 12. Each specimen, measuring approximately $3\times2\times2$ mm^3 (Fig 5.1c), was immersed in saline with protease inhibitor (PI). The cartilage-bone specimens

were individually sealed in glass tubes with PI saline for μMRI. After μMRI, all specimens were used for histology.

5.2.2 μMRI Methods

The μMRI equipment used in this study was a Bruker AVANCE III HD 300 NMR spectrometer, which has a 7-tesla, 89-mm superconducting magnet and a microscopic imager. All specimens were imaged individually for quantitative T2 and T1ρ relaxation times, with the normal axis of the specimen surface set at 0˚ and 55˚ with respect to the external magnetic field (B_0). These two orientations correspond to the maximum and minimum influence of the dipolar interaction to spin relaxation, based on the characteristics of its geometrical factor ($3\cos^2\theta - 1$) (Xia, 1998). The μMRI experiments used magnetization-prepared imaging protocols (Xia, 1998), where the echo time (TE) in the 2D mapping segment was kept constant at 7.19 ms. The TE values used in the quantitative T2 experiments, and the spin-lock durations used in quantitative T1ρ imaging, are summarized in Table 5.1. The slice thickness was 0.8 mm, and the repetition time (TR) was 1800 ms in both T2 and T1ρ imaging at all orientations. The field of view (FOV) was 3.4×3.4 mm for all specimens except mature femoral specimens, for which it was 3×3 mm. The 2D matrix was 256×128, which was reconstructed into 256×256 during quantitative analysis. These imaging parameters gave a pixel resolution for all cartilage specimens of 13.2 μm, except mature femoral cartilage at 11.7 μm. T1ρ imaging was carried out at the spinlock field of 2 kHz. The choice of 2 kHz was based on our previous studies on T1ρ (Wang and Xia, 2012), where the measurement was found to be approximately isotropic (hence less susceptible to the orientational differences of the specimens).

5.2.3 PLM Methods

All cartilage-bone specimens after μMRI were fixed in 10% buffered formalin and sent to Yale Pathology Tissue Services (New Haven, CT) for histological services. The paraffin method was used to treat the specimens; three 6-μm thick sections were made from each specimen. Histological sections were made on all specimens so that the histology slices coincided with the μMRI slices. All sections were imaged using a PLM system that consists of a digital imaging attachment mounted on a polarized light microscope (Xia et al., 2001). Imaging with 10x and 40x objectives produced 2D images with a pixel resolution of 1 μm and 0.25 μm, respectively. The final results from each PLM imaging were one pair of quantitative 2D images of optical retardation and angular orientation for each section (Oldenbourg & Mei, 1995).

5.2.4 Data Analysis

1D cross-sectional profiles were generated from 2D μMRI and PLM images, from the selected regions of interest (ROI) using the public domain software Image J (version 1.52a). The ROI was taken in such a way that similar locations from the PLM and μMRI images were used. 10 and 132 parallel neighboring columns on quantitative 2D images from μMRI and PLM were used to generate the 1D profiles. Depth dependent profiles with standard deviations were made using KaleidaGraph (version 4.5.4), whose student t-test function was used for statistical analysis between μMRI and PLM data. A t-probability < 0.05 was considered significant. The established tissue-sub-division criteria were used to determine the zonal thicknesses (Lee & Xia, 2013; Xia et al., 2001).

5.3 Results

5.3.1 Quantitative T2 and T1ρ Maps in μMRI

Fig 5.2 summarizes the μMRI results for both mature and immature tissues, where the laminar appearance of cartilage can be seen in all samples when their orientations are at 0˚ with respect to the external magnetic field B_0. For immature cartilage at 0˚orientation, cartilage and bone are visible in both humeral and femoral tissues (Fig 5.2a and 5.2c). For mature cartilage at 0˚ orientation, however, it is difficult to distinguish the deep cartilage from the bone in both humeral and femoral tissues (Fig 5.2b and 5.2d), even at the shortest TE (2 ms). When the tissue is oriented at 55˚ to the external magnetic field (i.e., at the magic angle), all cartilage samples appear homogenous as a result of the minimization of the dipolar interaction. Furthermore, when all imaging parameters are equal, the image intensity of mature tissue is lower than the intensity of immature tissue.

From the quantitative T2 and T1ρ images in Fig 5.2, the depth-dependent relaxation profiles of the humeral cartilage were extracted and compared in Fig 5.3, between immature and mature tissues. Several features of these profiles can be noted. First, the mature cartilage is about 25% thinner (based on Tables 5.2 and 5.4) than the immature cartilage. Second, the mature cartilage has lower T2 and T1ρ values than the immature cartilage, which is the reason why it is difficult to distinguish the deep cartilage from the bone in both humeral and femoral tissues in μMRI (Fig 5.2b and 5.2d). Third, T2 profiles of both mature and immature cartilage (Fig 5.3a and 5.3b) have a similar magic angle effect, which has a sharp peak at about 50 μm below the articular surface when the specimens were oriented at 0˚. In comparison, the T2 profiles of both mature

and immature cartilage lost this peak when the specimens were oriented at the magic angle (~55˚). This T2 anisotropy feature is similar to what has been observed in cartilage from large animals such as canines. Finally, the T1ρ profiles at 2 kHz spin-lock frequency do not have a significant difference between the 0˚ and 55˚ profiles, and both have higher values than the corresponding T2 profiles.

Fig 5.4 shows the depth dependent T2 and T1ρ profiles of the femoral cartilage from the knee joints, comparing immature and mature tissues. Nearly identical features can be found in the femoral cartilage, with one exception. In humeral cartilage (Fig 5.3), the peaks of the T2 0˚ profiles reach the values of the corresponding T2 55˚ profiles. The peaks of the T2 0˚ profiles in the femoral cartilage, in contrast, did not reach the values of the corresponding T2 55˚ profiles. The error bars in these quantitative plots (Fig 5.3, Fig 5.4) come from the depth-dependent row-averaging in data analysis, where the large error bars in the deep cartilage merely mean there were some miscalculated T2 or T1ρ values within the adjacent rows, commonly occurring at the regions where cartilage interfaces irregularly with the bone.

The zonal thicknesses in these cartilage specimens are summarized in Table 5.2. The zonal averaged T2 relaxation times are summarized in Table 5.3. From Table 5.2, the superficial zones and transitional zones of the immature cartilage show a slight increase in thickness as compared to mature cartilage in both humeral and femoral articular cartilage. When compared with the mature cartilage of both cartilage types, one notices a significant increase in the relative thickness of the radial zone in immature cartilage for both cartilage types (about an average of 27% increment). At 0˚, the transitional zones in the immature cartilage types are seen to have increased T2 values as compared to the

mature cartilage types with varied T2 values for the rest of the zones (Table 5.3). Also at 55˚, there is a general increase in T2 values in the immature cartilage types in all zones as compared to the mature cartilage types.

5.3.2 Quantitative Retardation and Angle Maps in PLM

Fig 5.5 shows the 2D angle and retardation images and their depth-dependent profiles of humeral cartilage, comparing immature and mature tissues. In these types of quantitative angle images, the blue and red colors represent the fibril orientations that are 90˚ apart. One can see that both immature and mature cartilage have a well-recognized fibril transition of ~90˚ between the surface fibers and the deep fibers, which is consistent with similar data from large animals. In the quantitative retardation images, larger values mean better organization among the fibers. One can easily tell that the retardation profiles of mature cartilage in rabbits have features that are consistent with mature tissue from larger animals such as canines, which have the lowest dip at 50 μm below the articular surface, representing the middle of the transitional zone. At the same time, the peak at the deep tissue, about 300μm in-depth, represents the tidemark that separates the uncalcified cartilage from the rest of the deep tissue that interfaces with the subchondral bone. In comparison, the retardation profile of the immature cartilage has an ill-defined dip in the transitional zone and no clear tidemark in the deep tissue. Similar observations can be found in femoral cartilage when comparing immature and mature tissues, as shown in Fig 5.6.

The thicknesses of the cartilage as measured by μMRI and PLM are summarized in Table 5.4. In general, there were large differences in thickness between the immature and mature tissue, for both humeral and femoral cartilage. Statistically, the t-probabilities

are significant for the differences between the immature and mature femoral tissues by μMRI and PLM (t-probability < 0.05), while those for humeral cartilages were weaker.

Fig 5.7 shows a selection of the higher resolution angle and retardation images obtained by the 40x objective (hence 0.25 μm per pixel), from the same tissue sections shown in Fig 5.5 and Fig 5.6, on which the cellular structures are now visible. Since the particular histology procedure did not preserve the cellular details, the black 'holes' inside the articular cartilage in the retardation images are the locations where the cells and cell clusters used to reside. (The same cellular regions are not obviously recognizable in the angle images due to the algorithm in the quantitative calculation.) Several features can be identified from these high-resolution optical images. First, there is a clear difference in the sizes of cells or cellular clusters between the surface tissue and the deep tissue, where the cellular sizes are smaller in the surface tissue. Second, since the long axis of the cell and cell clusters follow the fibril orientation of the territorial matrix in cartilage, one can easily determine a 90˚ zonal orientation of the collagen fibers in the arched territorial matrix by the orientation of the cellular clusters between the surface tissue and deep tissue. Finally, higher retardation values can be found in the proximity of cells and cellular clusters, which indicates the presence of a cocoon-shaped fibril structure surrounding each cell or each group of cells. (The same cocoon-shaped fibril structure could also be seen if we enlarge the quantitative angle images, in which the values of the fibril angle change in the order of blue-white-red-black colors.)

5.4 Discussion

The development of articular cartilage involves the formation of specific structural patterns in the cellular organization (Flandry & Hommel, 2011) and other tissue

components such as the collagen network and proteoglycans. The high-resolution imaging modalities used in this study allow us to determine the structure of cartilage through their cells and the ECM components.

5.4.1 Immature vs. Mature Cartilage

In both humeral and femoral cartilage, the immature cartilage viewed from the joint had a translucent, dark-pinkish appearance as compared to mature cartilage, which appeared more solid and bright pink (Fig 5.1). This might be from depletion of iron in mature tissues resulting from an increased level of hepcidin (Fairweather-Tait et al., 2014).

The MRI images from the mature cartilage appeared darker in intensity than the immature tissue, even at the shortest echo time of 2 ms (Fig 5.2b, 5.2d). From the point of view of MRI, the dark images were due to the short T2 values in the tissue, which were evident from the T2 profiles (Fig 5.3, Fig 5.4), where the T2 of mature cartilage had lower values than the immature cartilage. Since T2 is sensitive to the motional dynamics of water molecules in the tissue, which is determined by the interactions between water and macromolecules (proteoglycans and collagen fibers), short T2 means tight interactions between water and macromolecules. This conclusion is supported by the PLM retardation images and profiles (Fig 5.5, Fig 5.6), where the retardation of the mature cartilage is about 50% higher than the immature cartilage. Since the retardation values in PLM are proportional to the fibril content (concentration, packing density, etc.) in cartilage, our imaging data collectively demonstrated that the mature cartilage has higher fibril content than the immature cartilage, which is consistent with the previous results (Jadin et al., 2005).

The second MRI parameter used in this study, T1ρ relaxation time, is known to be sensitive to a different aspect of molecular motion, which has motion frequencies in the range of tens of kHz, higher than those influencing the T2 relaxation. In this study, for the same tissue, T1ρ relaxation time behaved as expected, which included having values higher than the corresponding T2 relaxation, and having little anisotropy between 0˚ and 55˚ when the spin lock frequency was at 2 kHz (Wang & Xia, 2011). Comparing T1ρ data between the immature and mature tissues, however, we see that the immature tissue had higher T1ρ values, which is consistent with T2 values being higher in the immature tissues (i.e., more water, less organized fibril structure).

PLM is the gold standard in the studies of collagen-rich connective tissues such as articular cartilage (Alhadlaq et al., 2007). In our digital setup, two quantitative images are calculated for each tissue section on a pixel-by-pixel basis, which generates a 2D map of retardation that quantifies the collagen organization, and a 2D map of angle that quantifies the collagen orientation (Xia et al., 2001). The retardation profile in the mature tissue had a nearly linear increase from its lowest point (which is the middle of the transitional zone) towards the cartilage-bone interface, where the peak in the deep cartilage signals the tidemark (c.f., Figs 5.5 and 5.6). This feature is similar to what has been observed in other large animals (Lee & Xia, 2013). The retardation profile in immature tissue, also had a nearly linear increase from its lowest point towards the cartilage-bone interface, had a less steep profile (hence less variation in fibril organization) and lacked a clearly recognizable peak in the deep cartilage (which signals the tidemark). These differences show the tissue maturation process under the adaptive use of joints for load bearing (Williamson et al., 2001).

5.4.2 Femoral vs. Humeral Cartilage

Despite differences between mature and immature cartilage, the femoral cartilage showed more differences compared to the humeral cartilage. In both mature and immature humeral cartilage (Fig 5.3), the T2 0˚ peaks in the transitional zone reached the T2 55˚ values, which can be explained by the classical three-zone fibril structure and are consistent with the characteristics of other mature cartilage such as from canines (Xia et al., 2001). In contrast, in both mature and immature femoral cartilage (Fig 5.4), the peak values of the T2 0˚ profiles (which occur in the middle of the transitional zone) did not reach the peak values of the T2 55˚ profiles, which show the morphological differences between the two kinds of cartilage (humeral vs femoral). Consequently, the minimization of the dipolar interaction in μMRI at the magic angle (55˚) was not able to remove completely the influence of the relaxation characteristics in femoral cartilage. Further experiments are needed to differentiate the various physical mechanisms that influence spin relaxation in femoral cartilage.

In addition, while humeral cartilage has a set of features more consistent and uniform over the joint surface, femoral cartilage has more variation. For example, comparing Fig 5.5 and Fig 5.6, one can see that even over the length of the specimen, the image and profiles of the femoral cartilage have different features between the left and right end of the specimen (merely 3 mm in length). These differences between humeral and femoral cartilage might be the consequence of different loading patterns of the individual joints during the maturation.

5.4.3 μMRI vs. PLM

Two different microscopic imaging techniques were used in this study. Based on the same physics principles as in clinical MRI, μMRI is extremely sensitive to different molecular motions in soft tissues, which can be quantified by the relaxation times. In comparison, PLM is the gold standard in histology and is capable of quantifying the fibril organization and orientation based on the optical birefringent information. Between the two imaging techniques, μMRI is totally non-invasive and non-destructive, while PLM is destructive and can image only thin sections. In addition, the principles of imaging are totally different between μMRI and PLM, where PLM enjoys higher optical resolution.

This study found that immature cartilage was on average thicker than mature cartilage for both the humerus and femur, which is evident from the profiles both by μMRI (Fig 5.3, Fig 5.4) and PLM (Fig 5 .5, Fig 5.6). Since PLM has a higher image resolution, it offers a better determination of the tissue thickness. For the mature tissue, the thickness of the non-calcified cartilage is commonly determined from its articular surface to its tidemark in PLM (Xia et al., 2001), which signals the front of mineralization where cartilage interfaces with the underlining subchondral bone (Williams et al., 2008). In immature cartilage, however, the lack of the tidemark results in a less accurate determination of the non-calcified tissue thickness in PLM; we measured the total tissue until the cartilage and bone interface, which might slightly overestimate the total thickness.

A note could be made here with regard to the quantitative relaxation measurements. In MRI, quantitative relaxation maps are obtained by acquiring several intensity images, each with a different relaxation weighting (i.e., different delay times in

the pulse sequence). The selection of a finite number of delay times (for T1 and T2) or spin-lock durations (for T1ρ) in any quantitative MRI is always a compromise, given that the tissue's relaxation values are depth-dependent, and it is only possible timewise to do 3–6 weighted images. If the delay time is short, then the long relaxation values will be poorly determined; in contrast, if the delay time is long, the short relaxation values will be poorly determined. The pulse sequences and parameters in this experiment were established in one of our previous studies (Mahar *et al.*, 2018). We have done sufficient preliminary experiments to know this set of weightings is adequate.

5.5 Conclusion

Immature and mature cartilage have significant structural differences in terms of their T2 and T1ρ relaxation times, thicknesses, cellular and physical appearances, and optical properties. For studies and models involving MRI, any pulse sequence with shorter echo delays (e.g., UTE, or ultra-short-echo) could be more beneficial if the cartilage bone interface is of concern. Any detailed determination of the ECM and cellular architectures would benefit from the employment of optical birefringence in PLM at higher resolution. Better knowledge of the characteristic differences between immature and mature cartilage could lead to an improved understanding of developmental biology and special needs in translational research that involves rabbit models.

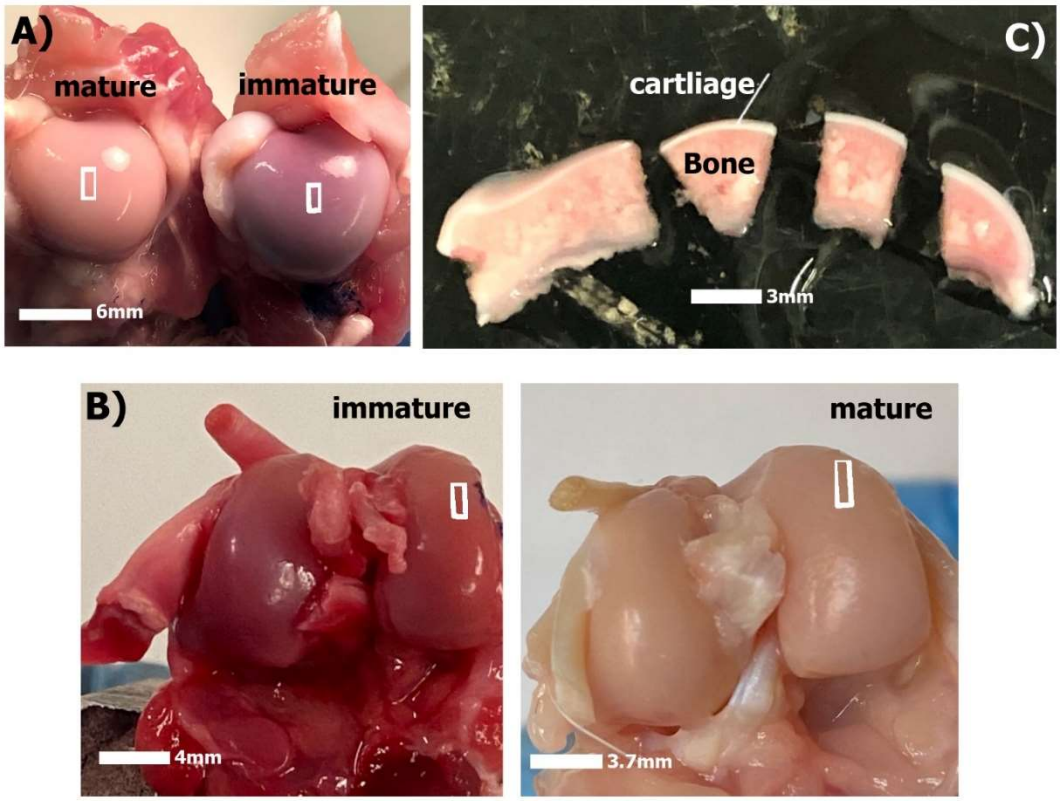

Figure 5.1 Photos of rabbit immature and mature joints. (a) Humeral heads from the shoulder joints and (b) femoral heads from the knee joints. (c) Several cartilage-bone blocks were harvested from both humeri and femurs for high-resolution imaging. The rectangular boxes in (a) and (b) indicate where the sample blocks were taken from the joint surfaces.

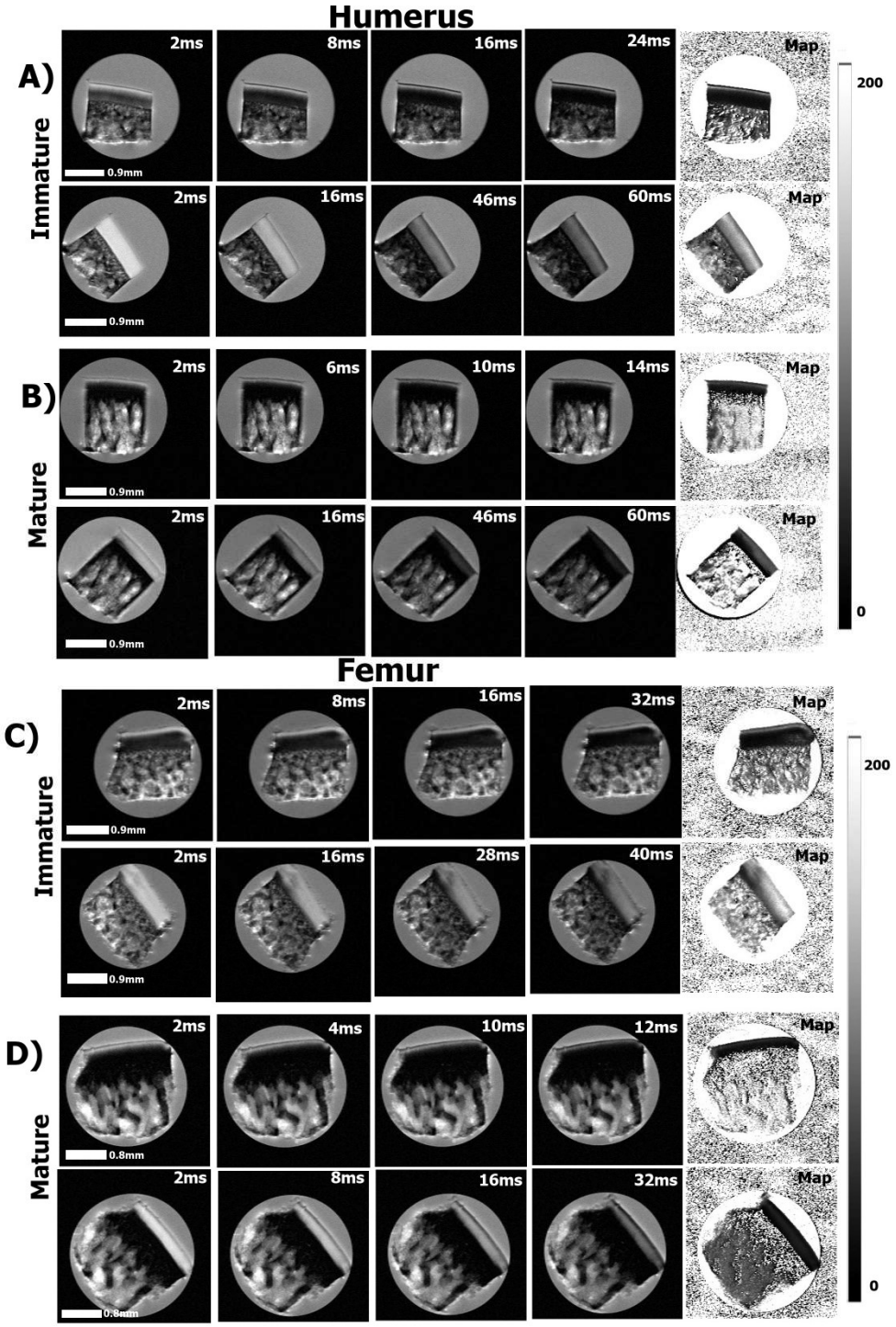

Figure 5.2 MRI images of immature (a, c) and mature (b, d) cartilage blocks from humeri (a, b) and femurs (c, d) at 0˚ and 55˚ orientations to the magnetic field (B_0), which points vertically up, respectively. The first four columns contain T2 weighted intensity images, while the last column contains the calculated T2 images. All relevant images are plotted on the same greyscale.

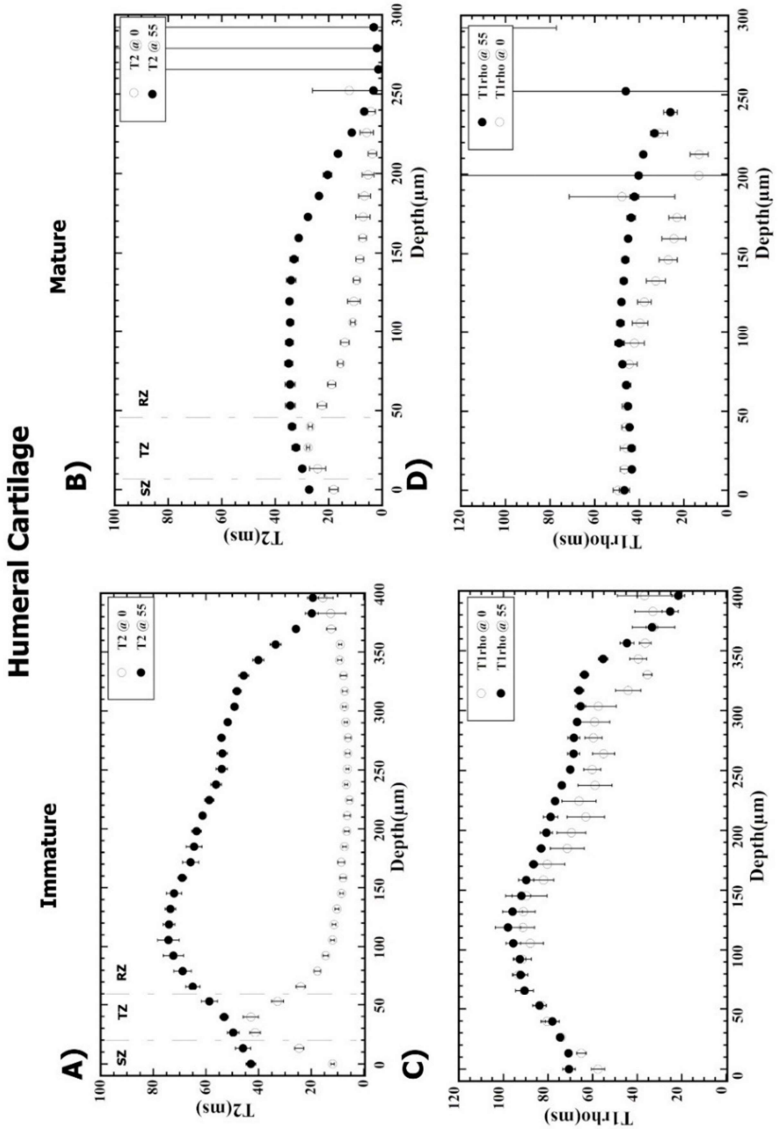

Figure 5.3 T2 (a, b) and T1ρ (c, d) depth-dependent profiles of immature (a, c) and mature (b, d) cartilage of the humerus at 0˚ and 55˚ orientations to B_0, respectively. Note that each of these profiles was from a single image, where 10 and 132 parallel neighboring columns on quantitative images were averaged to generate the 1D profiles. The error bars were from the column averaging.

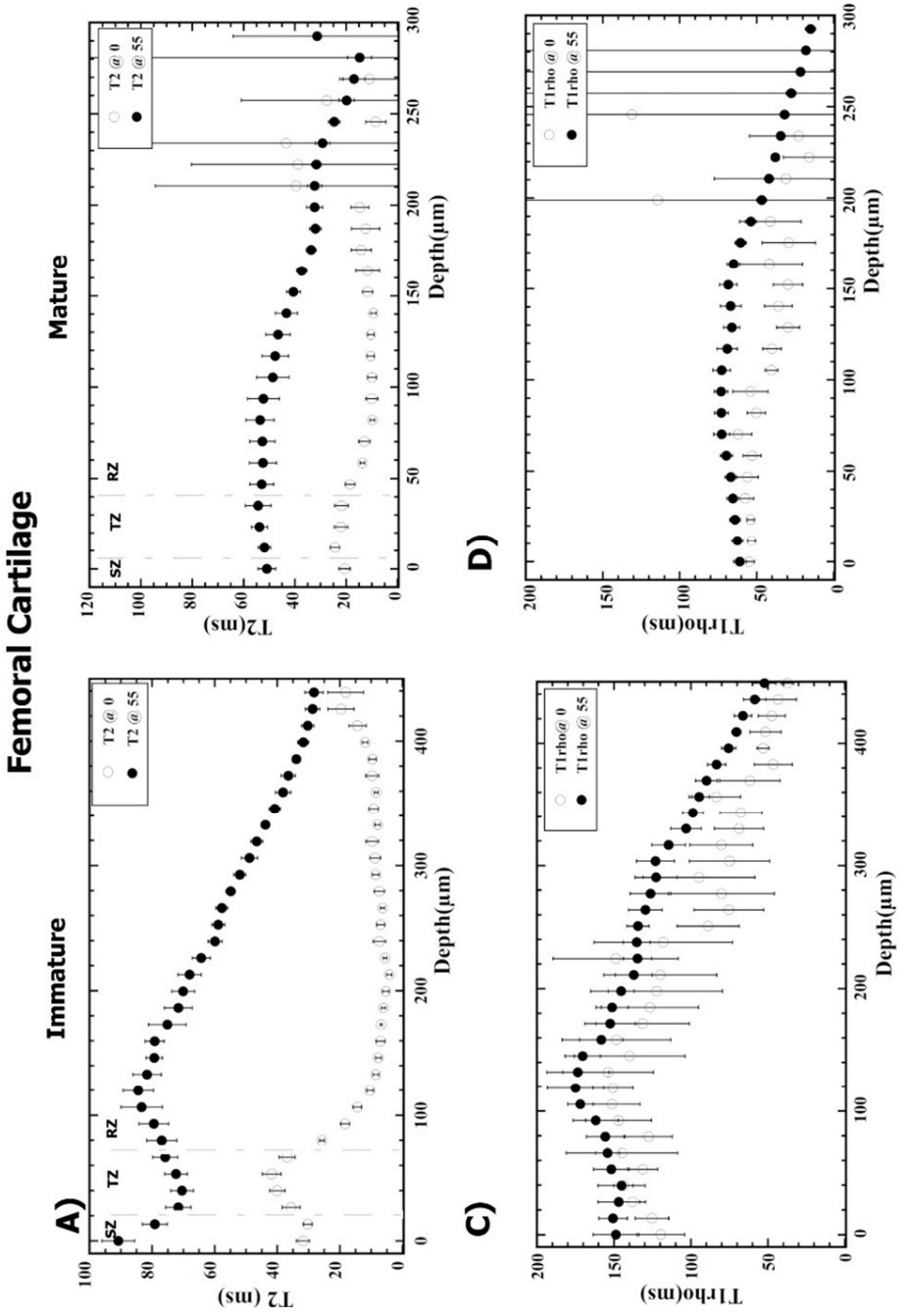

Figure 5.4 T2 (a, b) and T1⟩(c, d) depth-dependent profile of immature (a, c) and mature (b, d) cartilage of femurs at 0˚ and 55˚ orientations B_0, respectively. (Each of these profiles was from a single image, as in Fig 5.3.)

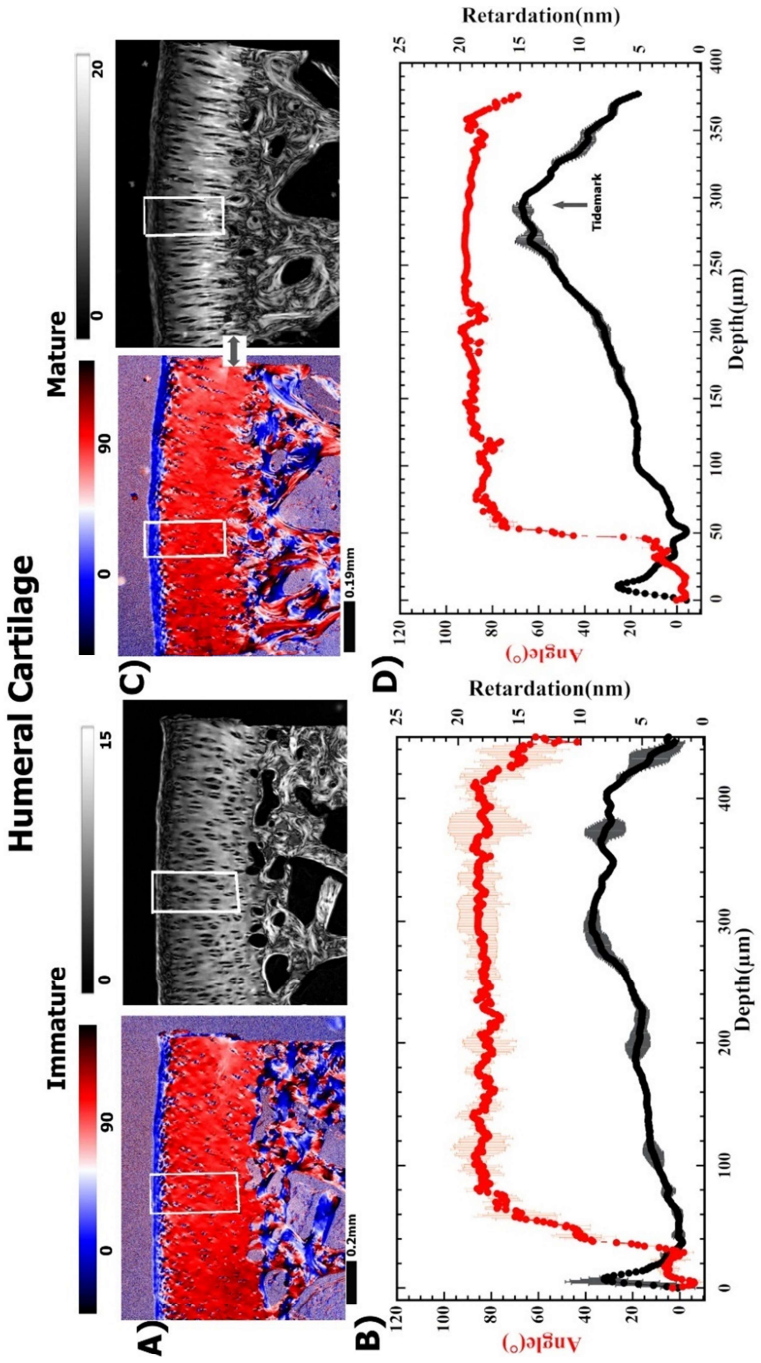

Figure 5.5 2D angle and retardation images (a, c) of immature and mature humeral cartilage and their depth-dependent profiles (b, d). The rectangular boxes on 2D images indicate where the regions of interest (ROI) were taken for the profile analysis.

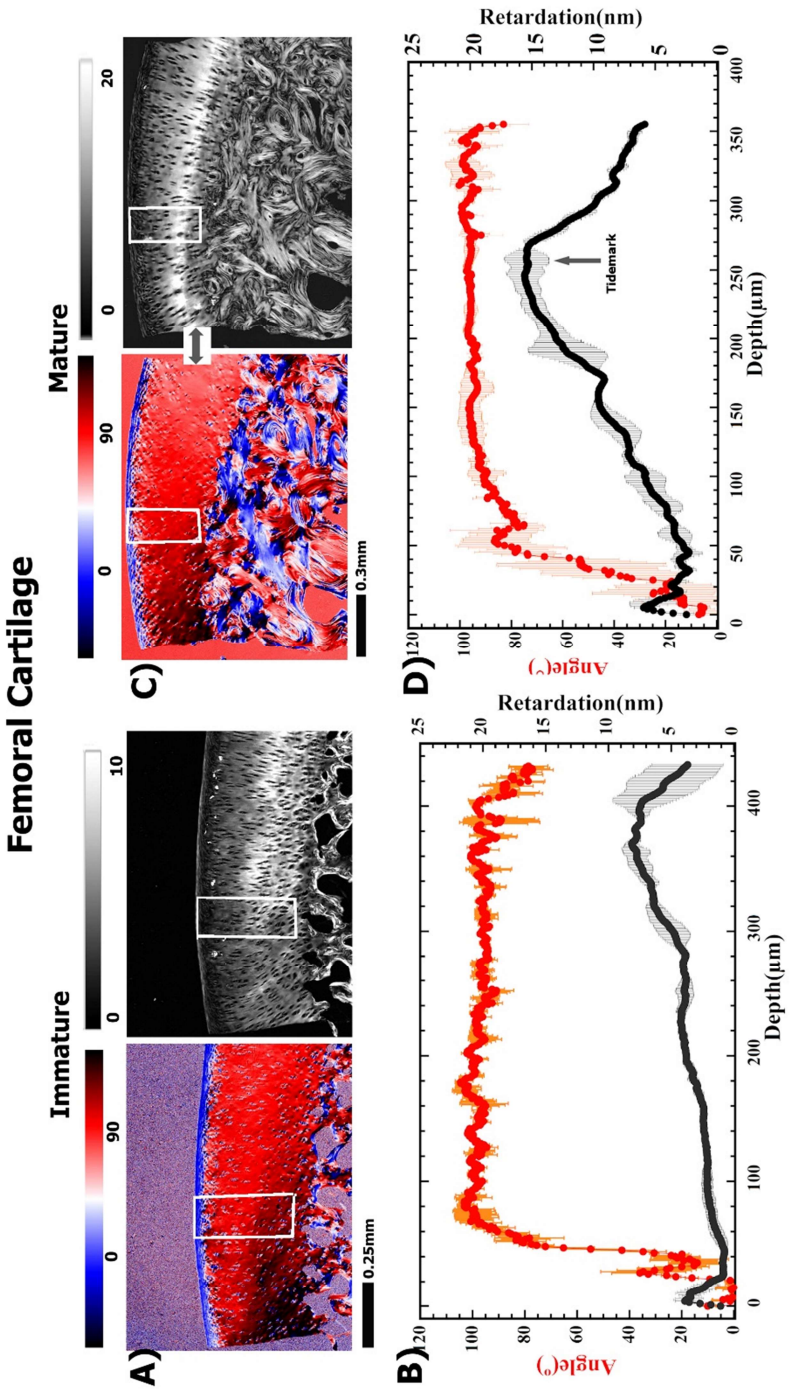

Figure 5.6 2D angle and retardation images (a, c) of immature and mature femoral cartilage and their depth-dependent profiles (b, d). The rectangular boxes on 2D images indicate where the regions of interest (ROI) were taken for the

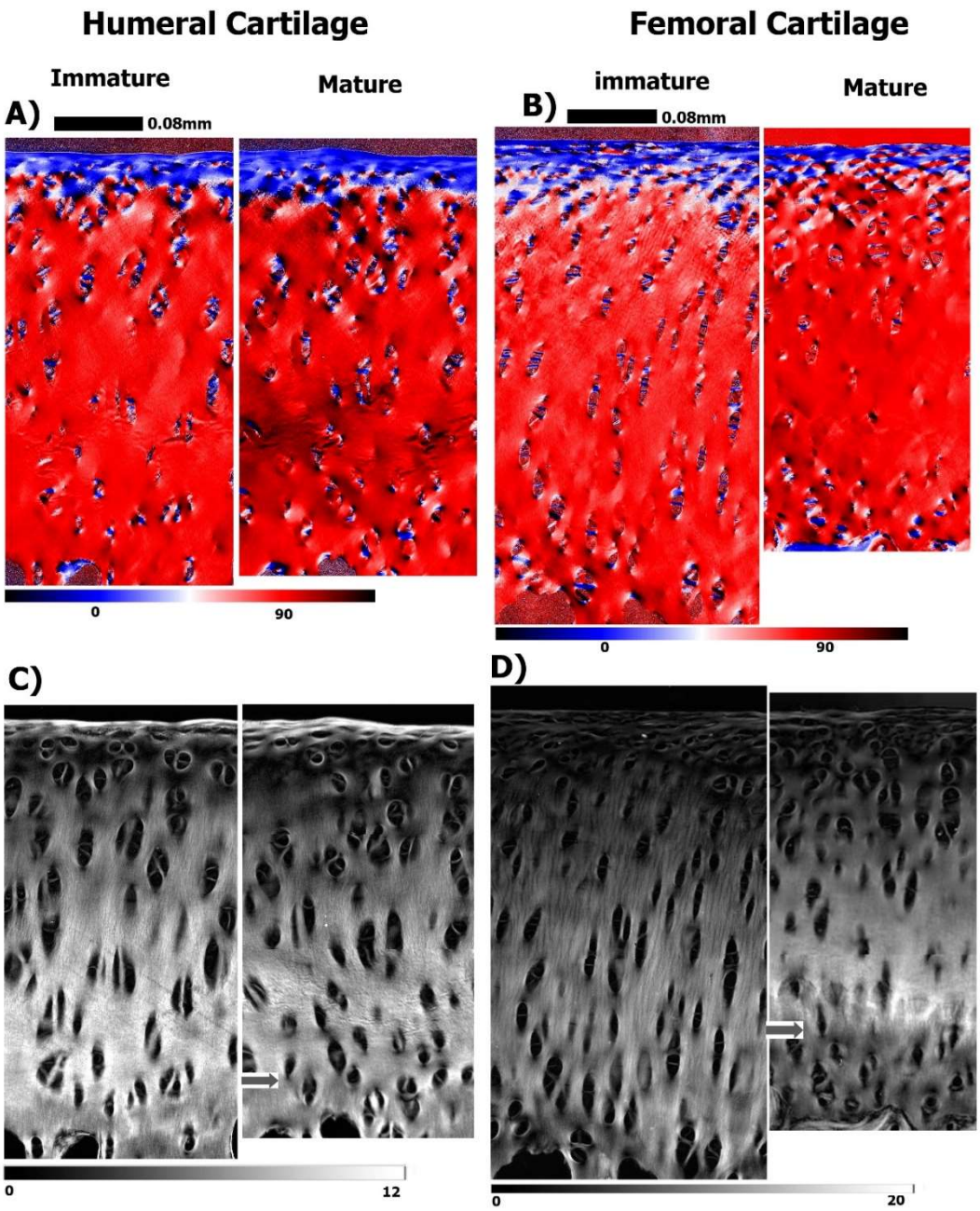

Figure 5.7 (a) and (b) are 2D angle images, and (c) and (d) are retardation images of the same cartilage sections at higher resolution (0.25 μm per pixel) for both humeral (a, c) and femoral (b, d) cartilage. The arrows indicate an estimate of tidemarks.

Table 5.1 Echo Times (TE) used in quantitative T2 and T1ρ imaging experiments

Cartilage	Orientation	T2 Experiments		T1ρExperiments (spin-lock = 2 kHz)	
		Immature TE (ms)	Mature TE (ms)	Immature TE (ms)	Mature TE (ms)
Humeral	0˚	2, 8, 16, 24	2, 6, 10, 14	2, 16, 46, 80	2, 16, 46, 60
	55˚	2, 16, 46, 60	2, 16, 46, 60	2, 16, 46, 80	2, 16, 46, 60
Femoral	0˚	2, 8, 16, 32	2, 4, 10, 12	2, 16, 46, 60	2, 16 46, 60
	55˚	2, 16, 28, 40	2, 8, 16, 32	2, 16, 46, 60	2, 16, 46, 60

Table 5.2 Averaged zonal thicknesses based on T2 profiles. σ represents the standard error. % is the relative percent thickness of each zone based on the total tissue thickness.

Cartilage Specimens	Superficial Zone (μm)	Transitional Zone (μm)	Radial Zone (μm)	Total Thickness (μm)
Humeral				
A) Immature				
23LS	26.4	52.8	303.6	382.8
13RS	26.4	26.4	250.8	303.6
18RS	39.6	39.6	264.0	343.2
Mean ± σ	30.8 ± 4.4	39.6 ± 7.6	272.8 ± 115.9	343.2 ± 22.9
%	9	12	79	100
B) Mature				
1305LS	26.4	26.4	198.0	237.6
1305RS	13.2	39.6	184.8	250.8
BMH3LS	11.7	35.1	234.0	280.8
Mean ± σ	17.1 ± 4.7	33.7 ± 3.9	205.6 ± 14.7	256.4 ± 12.7
%	7	13	80	100
Femoral				
C) Immature				
16RF	26.4	39.6	330.0	396.0
11RF	35.1	35.1	234.0	304.0
16LF	29.1	48.5	388.0	465.0
Mean ± σ	30.2 ± 2.6	41.1 ± 3.9	317.0 ± 44.9	388.3 ± 46.7
%	8	11	81	100
D) Mature				
1305LF	11.7	23.4	175.5	210.6
BMH3LF	23.4	35.1	198.9	187.2
BMH3RF	23.4	35.1	128.7	163.8
Mean ± σ	19.5 ± 3.9	31.2 ± 3.9	167.7 ± 20.6	218.0 ± 20.6
%	9	14	79	100

Table 5.3 Zonal averaged T2 and T1ρ values of cartilage based on the orientation-dependent profiles shown in Fig 5.3 and Fig 5.4.

	T2 (ms)				T1ρ (ms)			
	Immature		Mature		Immature		Mature	
	0˚	55 ˚	0˚	55 ˚	0 ˚	55 ˚	0˚	55 ˚
(A) Humeral cartilage								
SZ	17.0 ± 1.7	57.3 ± 6.9	20.4 ± 6.6	44.5 ± 10.9	59.65 ± 1.7	70.2 ± 1.4	47.0 ± 4.9	45.0 ± 1.6
TZ	35.5 ± 3.4	49.7 ± 3.5	24.80 ± 6.89	46.43 ± 10.1	82.4 ± 3.4	81.6 ± 2.5	45.2 ± 1.9	47.0 ± 0.3
RZ	8.95 ± 0.4	49.0 ± 5.0	8.6 ± 1.7	36.43 ± 6.4	67.0 ± 3.2	76.8 ± 3.4	35.4 ± 1.7	42.5 ± 2.5
(B) Femoral cartilage								
SZ	33.8 ± 5.4	77.5 ± 6.4	16.3 ± 2.1	32.7 ± 9.5	129.6 ± 7.1	147.9 ± 2.8	54.0 ± 0.8	63.1 ± 1.4
TZ	47.8 ± 11.6	68.2 ± 1.3	19.0 ± 2.3	37.6 ± 8.0	138.6 ± 3.2	149.8 ± 7.8	57.9 ± 2.1	65.8 ± 1.4
RZ	10.50 ± 2.9	54.4 ± 12.4	10.9 ± 1.0	39.2 ± 3.5	107.8 ± 10.5	136.5 ± 2.0	39.2 ± 3.0	62.8 ± 6.0

Table 5.4 Correlations of average total thickness in mature and immature tissues between MRI and PLM

	μMRI Total Thickness (μm)	PLM Total Thickness (μm)	t probability
A) Humeral Cartilage			
Immature	343.2 ± 22.9	381.0 ± 31.0	0.53
Mature	256.4 ± 12.7	259.0 ± 9.0	0.73
t probability	0.2	0.06	
B) Femoral Cartilage			
Immature	388.0 ± 46.7	410.0 ± 10.0	0.65
Mature	218.0 ± 20.6	249.0 ± 31.0	0.38
t probability	0.01	0.04	

CHAPTER SIX

CHARACTERISTICS OF DISTAL FEMORAL ARTICULAR CARTILAGE IN SIX WEEKS POST-TRAUMATIC OSTEOARTHRITIS BY A SUB-CRITICAL IMPACT

6.1 Introduction

Post-traumatic osteoarthritis (PTOA) is costly and accounts for approximately 12% of all symptomatic osteoarthritis (OA) cases in the United States (Brown et al., 2006). PTOA affects the younger and active population making its onset occur early and costing more than the typical OA (Carbone & Rodeo, 2017). It is most frequent in knee joints and has symptoms characterized by damage to articular cartilage and subchondral bone, pain, and stiffness in the joint (Benedek, 2006; Watt et al., 2019). The study in this chapter focuses on the sub-critical damage to the articular cartilage of the knee joint using a post-traumatic disease progression rabbit model.

The pathogenesis of PTOA is not yet fully understood (Kramer et al., 2011; Marks, 2014). For example, the onset of PTOA is unpredictable clinically as it is diagnosed at the symptomatic phase which may occur early or over a long period of time after being triggered by the initial trauma (Punzi et al., 2016). In addition, some anti-inflammatory therapeutics were recently proposed for the prevention and delay of the disease (Khella et al., 2021a), which would require the successful validation of predictive markers to the progressive nature of PTOA (Punzi et al., 2016). It is therefore crucial to carry out the preclinic PTOA study during its early stages through various mechanical events, to fully understand the characteristic pathogenesis of cartilage degradation in trauma-Induced joint degradation.

In this study, we show both qualitative and quantitative characteristics of articular cartilage during the early stages of OA through the application of one sub-critical impact to the knee of the rabbit joint. We achieved this goal using microscopic Magnetic Resonance Imaging (μMRI) and Polarized Light Microscopy (PLM) techniques. MRI is a non-invasive procedure known to be exceptional in the detection of pathological processes of the knee joint at higher resolutions (Nissman et al., 2008) when compared to plain radiography. We utilized the anisotropy of T2 relaxation in this study, which has the sensitivity to the dynamics of water molecules in the tissue and reflects the organization of the collagen matrix in the tissue (Mantebea et al., 2021; Wang & Xia, 2012; Xia, 1998). In addition, PLM the gold standard in clinical histology, was used to examine the fibril structure in cartilage tissues via their birefringent properties (Xia et al., 2001). Quantitative measurement by Inductively Coupled Plasma-optical emission spectrometry (ICP-OES) was also performed to determine the concentration of minerals in the cartilage, which complements the imaging results (Wang et al., 2013).

6.2 Materials and Methods

6.2.1 The Impact Model

A total of twelve female mature rabbits were used in this study. The ages of the rabbits were 6 months and older and each weighed approximately 3-4kg. The rabbits were randomly grouped into two: 0 week post-surgical group (control group, N=6) and 6 weeks post-surgical group (N=6). An impact device with a metal hemispherical indenter tip was built in-house to deliver an impact to the knee (Leucht et al., 2012). The amount of a single impact was calibrated using several pressure sensor films (Fujifilm Prescale, via Sensor Products Inc., Madison, NJ 07940), to be approximately 30MPa. Under the

surgical condition, an incision was made to the joint capsule following a medial parapatellar incision to the skin. The patella was subluxated and a single impact was applied to the medial aspect of the femur as shown in Fig 6.1A (inside the dotted rectangular shape on the femur). The surgical procedures were performed at the Beaumont Research Institute. For the 0 week (control) group, one knee from each animal (right knee) was impacted and the contralateral knee (left knee) was non-impacted. The rabbits from this control group were sacrificed immediately after the impact and the joints excised. For the 6 weeks group, an identical surgical and impact procedure was performed; the impact site was sutured back subsequently. The rabbits were sacrificed six weeks after the impact. Notes and pictures on the visual observations of the joints were taken during sample preparation and before imaging.

6.2.2 Specimen Preparation

During specimen harvesting, blocks of articular cartilage still attached to the underlying bone were cut from 12 impacted and 12 contralateral femurs in both 0 week and 6 weeks groups (dotted box in Fig 6.1A). A total of 24 samples were harvested for this study: 6 impacted femurs (0 week), 6 each contralateral femur from the 0 week group, 6 impacted femur (6 weeks), and 6 contralateral femurs from the 6 weeks group. All cartilage blocks were taken consistently from approximately the same location on the medial femoral condyles for all joints. The cartilage-bone blocks, each measuring 2 x 3 x 2 mm, were sealed in individual glass tubes that contained saline with protease inhibitor (PI).

6.2.3 Imaging Techniques

All cartilage-bone specimens in the sealed glass tubes were imaged individually using Bruker AVANCE III HD 300 μMRI imager, with a 7-Tesla 89-mm superconducting magnet. The quantitative T2 imaging experiments used a magnetization-prepared pulse sequence (Xia, 1998). The T2 measurements were made while the normal axis of the cartilage surface was set to 0˚and 55˚ to the external magnetic field (B_0), which specifies the maximum and minimum influences of the dipolar interaction to spin relaxation (Xia, 1998). For all experiments, the slice thickness was kept at 0.8mm; the field of view (FOV) was 3 x 3 mm. The matrix size for imaging was 256 x 128 and was reconstructed during the quantitative analysis to 256 x 256, which resulted in the transverse resolution at 11.7μm/pixel. The image-formation segment had a constant echo time (TE) of 7.19ms and a repetition time (TR) of 1800ms; the T2 contrast segment had a series of varying TEs, which were 2, 4, 6, and 12ms for the 0˚ specimen orientation and 2, 8, 16, and 32ms for the 55˚ orientation.

All cartilage-bone specimens after μMRI were sent to an external histological service for tissue process (Yale Pathology Tissue Services, New Haven, CT). Briefly, the specimens were fixed in 10% buffered formalin and treated with the paraffin method. Three histological sections (6 μm thickness) from each specimen were made in the middle of the tissue block, approximately at the same slice location in μMRI. The sections were then imaged using a polarized light microscopy (PLM) system, which was described in a previous paper (Xia et al., 2001). The intensity images from this PLM system are sensitive to the birefringent property of the cartilage; two 2D quantitative images of each section can be constructed from a series of intensity images each at

different polarization, one azimuth image in the unit of degree and one retardation image in the unit of nanometers.

6.2.4 ICP-OES Experiments

To determine the glycosaminoglycan (GAG) concentration in cartilage, additional forty-eight cartilage specimens from the locations adjacent to the impact/imaging location were harvested from all 0 week and 6 weeks joints, approximately at the anterior and posterior locations of both impacted and non-impacted femurs. These adjacent specimens were weighed wet (ww) using an analytical balance three times for accuracy. The specimens were then dried in an oven for three hours, and subsequently weighed again as dry weights (dw). The water percent was calculated using the weights ((ww-dw)/ww %) for each specimen. The tissue was then liquefied by concentrated 100 μL of nitric acid (HNO3) overnight and subsequently diluted to 4.85 mL of ultra-pure water. An internal standard was added to the aqueous samples (50 uL) making a total volume of 5 mL. A Perkin Elmer inductively coupled plasma optical emission spectrometer (ICP-OES) Optima 7000 DV (Waltham, MA) was used to measure Sodium concentration in mg/L for the calculation of GAG concentration (mg/ml) using Donnan equations (Jacques, 2013; Lesperance et al., 1992; Shapiro et al., 2000; Wang et al., 2013; Zheng & Xia, 2010) . In all cases, a calibration curve, and QC samples was ran for every ten samples with the curve calibration of 0.999 correlation averagely.

6.2.5 Data and statistical analysis

In the analysis of quantitative 2D T2 images from the μMRI experiments, the depth-dependent profiles from a 10-pixel width of the region of interest (ROI) from the middle of the tissue were extracted and averaged using a public domain software ImageJ

(v1.25a) and a commercial software KaleidaGraph (v 4.5.4). In the analysis of quantitative 2D angle and retardation images from the PLM experiments, similar approaches and software were used with an ROI of 117 pixels at similar locations as in the μMRI procedure. The widths of the tissue averaged in both μMRI, and PLM were approximately the same (117 μm). The total thickness of cartilage was measured from the 2D intensity images in μMRI at 55˚ and the zonal thickness by the 1D depth-dependent profiles based on T2 at 0˚ based on earlier established criteria (Lee & Xia, 2013). For a more accurate comparison, the radial zone was divided into two (RZ1 and RZ2) and the bulk relaxation times for T2 were averaged over the entire tissue from the region of selected zones. A one-way ANOVA with Bonferroni correction was performed to test a pair-wise difference between control, OA, impact, and nonimpact for bulk and zonal parameters. A p-value of less than 0.05 was considered statistically significant. To enable direct comparison of the articular cartilage with variations in thickness, the depth-dependent profiles were normalized to 0 to 1, with 0 indicating the surface of the cartilage and 1 indicating the cartilage bone boundary.

6.3 Results

6.3.1 Visual Observation

The average width of the femur across the condyles at the point where the cartilage block was measured at approximately 1.5 cm, and the medial condyle measured at approximately 0.6 cm. The femoral cartilage of the impacted joint after 6week post-surgery was intact without significant sign of cartilage destruction, similar to the cartilage in the impacted 0 week joint (control). The femoral cartilage of the 6 weeks joint showed localization of ‘dark red to purple’ color change on the anterior aspect of the femur in

both impacted and non-impacted joints (Fig 6.1C). It should be noted that Fig 6.1B of the 0 week joint has an overall 'blood-red' appearance resulting from fresh oxygenated blood of immediate post-surgical procedure.

6.3.2 μMRI Measurement

Fig 6.2 shows the 2D MRI intensity images at both 0˚ and 55˚ orientations together with one corresponding T2 map at 0˚ orientation. Visually, the impact and non-impacted cartilage of the 0 week (Fig 6.2A) and 6 weeks (Fig 6.2B) samples looked similar with little changes in their cartilage thickness (summarized in Table 6.1). From the quantitative T2 images, the depth-dependent profiles of T2 were extracted out from all images, which were subdivided into the cartilage structural zones based on our published methods (Lee & Xia, 2013; Mantebea et al., 2021; Xia, 2000a; Xia et al., 2001). Fig 6.3 shows the correlation among the whole-profile averaged T2 values between the impacted and non-impacted samples for both 0 week and 6 weeks at the 55˚ orientation. While there was no difference in T2 between the non-impact and the impact control samples, there was a clear increase in T2 relaxation in the 6 weeks samples, where the impact T2 is higher than the non-impact T2 ($p=0.06$).

Fig 6.4 shows the zonal averaged T2 correlation between the impacted and non-impacted samples for both 0 week and 6 weeks. At the 55˚ orientation (Fig 6.4A), the zonal correlations show a significant T2 increase in both SZ and TZ ($p=0.003$) and a less significant increase in the RZ. At the 0˚ orientation (Fig 6.4B), although the zonal T2 have lower values due to the influence of dipolar interaction, a similar trend in the T2 correlation can be found. (RZ 2 at 0˚ was not analyzed due to extremely short T2 values causing an increase in noise influences in that region (Badar & Xia, 2022)). Table 6.2

summarizes the correlation in T2 relaxation between the impacted and non-impacted cartilage for both 0 week and 6 weeks samples. Table 6.2 in addition, summarizes are the measurements of the fitted line slopes for both groups of samples, where a steeper slope means T2 has increased. The slope of the solid diagonal in both Fig 6.3 and Fig 6.4 is 1.

6.3.3 PLM Measurement

Fig 6.5 shows the quantitative 2D angle (Fig 6.5A) and retardation (Fig 6.5B) images at a 1μm/pixel resolution, which enables the assessment of the architectural integrity of collagens in cartilage. One visual difference between the 0 week and 6 weeks groups can be noted: when compared to the 0 week samples, the cartilage surface in almost all the 6 weeks impacted samples shows reduced total thickness and less uniform fibril orientations. This is illustrated visually by the 2D angle image of the 6 weeks impacted sample having the thinnest blue region in the surface (i.e., the least amount of uniform fibers in parallel with the articular surface) as well as the 2D retardation image of the 6 weeks impacted sample has the lowest gray values in the surface (i.e., reduced retardation values), collectively indicating the fibril structures in the surface part of the articular cartilage have changed in the 6 weeks impacted group. These changes are statistically significant (Table 6.1) in the impacted joint as compared to the contralateral joint. In addition, there seems to be an increase in the volume of the individual chondrocytes in the majority of the samples in the 6 weeks groups. Note that there was no significant difference in the weights and ages between these two groups of rabbits.

Fig 6.6 compares the depth-dependent angle profiles between the 0 week and 6week of the impacted (Fig 6.6A) and the non-impacted cartilage (Fig 6.6C), which further supports the observations in the 2D images (Fig 6.5) by showing the diminishing

in the thickness at the superficial zone in the 6week impact cartilage samples as indicated in the arrow in Fig 6.6A. The corresponding depth-dependent retardation profiles show the reduction of the retardation values at the surface for the 6week impact samples (Fig 6.6B, pointed by the surface arrow), consistent with the observations in the 2D images (Fig 5.5) and supporting the observation of a reduced/disrupted surface structure. There is also a noticeable increase in the retardation values around the tidemark region, pointed out by the upwards arrow in Fig 6.6B. The values of the minimum and maximum retardations are summarized in Table 6.3. While the maximum retardation values are comparable, the 6 weeks impacted samples have an evidently smaller values in the minimum retardation region.

Table 6.4 summarized the ICP biochemistry analysis for the cartilage harvested from the locations adjacent to the impact/imaging locations from all 0 week and 6 weeks joints, approximately at the anterior and posterior locations of both impacted and non-impacted femurs. There were no significant differences among the bulk biochemical measurements of water percentage, GAG (mg/ml) and calcium concentration (mg/L), which further indicates the tissue degradation in this study was minor, i.e., at the very early stages of the progression.

6.4 Discussion

MRI has been used extensively in the research and clinal fields for the detection and management of osteoarthritis. In musculoskeletal application, clinical MRI does not have the resolution to detect the early stages of the degradation in osteoarthritic cartilage. μMRI, which shares the same physics principles and engineering architecture with clinical MRI, has the ability to study intact tissue blocks and live specimens non-

invasively and non-destructively, hence is widely used in preclinical studies in biomedicine. In this study, we combined μMRI with the quantitative optical imaging (PLM) to study the early stages of cartilage degradation that was triggered by a sub-critical impact, using a PTOA rabbit model. The use of μMRI is essential in this project due to the rather thin thickness of the rabbit cartilage (300-400 μm). The use of PLM further enhances the μMRI data with its optical resolution(Alhadlaq et al., 2004). The quantitative data from these microscopic imaging techniques are invaluable in monitoring the progression of OA irrespective of the cause in preclinical studies (Felson & Hodgson, 2014).

6.4.1 Early PTOA

When the resultant external trauma (e.g., a direct impact) is substantial but not catastrophic, the relevant tissues and joints in individual animals in an identically specified group could develop different and diverse responses in the subsequent post-traumatic period at the molecular and chemical levels, which include both progressive degeneration and remodeling or repair (Athanasiou et al., 1991). In this study, the trauma to the femoral head was caused by a single and direct hit with deliberate low pressure (~30 MPa). The design of this study was to use a pressure that would not cause significantly visible damage (hole) to the cartilage. After the impact, no substantial damage was visible on the articular surfaces of the impacted in the 0 week group (Fig 6.2A). At the 6 weeks post-trauma time point, however, there were signs of inflammation in the anterior aspect of the femur, around the patellar groove in both impacted and non-impacted joints, as reddening and signs of bruising is observed (Fig 6.2C). This

observation is consistent with the understanding to the causal role of inflammation in OA progression (Khella et al., 2021b).

Since both impacted and non-impacted femurs showed signs of bruising, the observation cannot be placed solely on the unintended damage and internal bleeding from the surgical procedure, but possibly to a reactive or inflammatory response to the immediate or acute phase of OA degradation, related to the mechanical stimuli through intraarticular bleeding (DeHaven, 1980). The signs of degradation in the non-impacted femurs might also be the consequence of changed gait patterns in the animals. In addition, we noted that the inflammatory sign did not occur on the central aspect of the medial condyle where the impact was made but rather on the anterior femur, which indicates OA as a localized process. That is, the early response and progression for OA does not occur uniformly over the entire cartilage surface at a time. This topographical variation in the response to impact inflammation could be due to the fact that loading is known to affect the metabolic activities of chondrocytes (Korhonen et al., 2008) as well as from the motional overloading of the non-impacted joint after any single-side injury. This topographical variation in the response to impact inflammation would also increase the challenges in an accurate determination of the early degradation in the affected joints.

6.4.2 OA Detection by MRI Technique

The intensity images in MRI between the 0 week and 6 weeks groups showed no significant changes in terms of cartilage lamination and cartilage thickness. This lack of visual differences illustrated a minimal damage to cartilage, which was the consequence of our intentionally sub-critical impact. Even using one of the highest transverse resolutions (11.7 μm/pixel) in this μMRI study, the voxel-averaged collagen fibers

remained unchanged during early osteoarthritis (Alhadlaq et al., 2004). The topographical nature of cartilage on the femoral joint further masks any detection sensitivity of MRI, when the intensity images are examined (Badar et al., 2021).

In contrast, our quantitative T2 results showed subtle changes in cartilage due to the impact. Based on extensive previous studies from many research groups (Baum et al., 2012; Friedrich et al., 2009), the values of T2 relaxation time have been linked to the progression of osteoarthritis, especially its values at the magic angle (55˚) due to the minimization of the dipolar interaction (Xia, 1998). In this study based on the T2 values at 55˚, the bulk T2 value for cartilage was higher in the 6 weeks group than in the 0 week group (Fig 6.3). This supports the understanding that an increase in hydration of the cartilage matrix is an early event in cartilage fatigue that signals the disruption of the collagen matrix (Lee et al., 2015). The changes in hydration in the superficial and transitional zones were the major contributing factor to the differences in the bulk cartilage (Fig 6.4), which illustrates a non-uniform degradation over the tissue thickness – i.e., the surface tissue degrades earlier than the deep tissue in this type of impact-induced osteoarthritis. The deep (radial) zones, which are the thickest sub-tissue zone in non-calcified cartilage, are the most difficult region to be examined by both clinical MRI and μMRI, largely due to their collagen structure and molecular composition. Past studies in the canine model of OA also showed that the deep cartilage would be the last region to be degraded by the osteoarthritic process (Alhadlaq et al., 2004).

An additional possible finding is that the applied impact, although sub-critical, had caused some minor damage to the subchondral bone plate, which could weaken the integrity of non-calcified cartilage. Any degradation in the subchondral bone plate could

have complex consequences to the health of cartilage, including the increased mineralization and other degradation (Batool et al., 2022; Bonucci & Gomez, 2012; Olmez & Schumacher, 1999). For example, the degradation of the cartilage matrix is known to be a possible critical factor for matrix calcification and a crystal deposition may occur without severe cartilage degradation (Terkeltaub, 2002). The potential mineralization of the deep cartilage, which shortens the T2 values, unfortunately increases the difficulties in the detection of the deep degradation by μMRI. Further studies of this deep region may require the use of some additional tools, such as microscopic computed tomography (μCT), which could sense the variations of the minerals in calcified cartilage and the subchondral bone plate.

6.4.3 OA Detection by PLM Technique

PLM technique has a higher spatial resolution (about 1 μm/pixel or higher) in imaging and PLM uses optical birefringence to examine quantitatively the collagen network in articular cartilage (Alhadlaq et al., 2007). In this study, the surface cartilage in the 6 weeks impact group was found to have a reduced zonal thickness in the angle map (thinner and noisy blue colors in the top right image in Fig 6.5A) in addition to a variable retardation value in the surface region (the reduced brightness in the gray-scale image on the top figure of Fig 6.5B) compared to the 0 week impact group. These two measurements illustrate collectively the most profound disruption of the surface collagens in the 6 weeks impact group. This subtle disruption of the cartilage surface in early OA is a significant biomarker and agrees with some previous studies of OA in canine cartilage (Alhadlaq et al., 2004). Our study showed a strong statistical difference in the SZ thickness between the control and OA, which was more significant in the impacted joint ($p=0.0002$) than in the

non-impacted joint (p=0.2). This is expected due to direct injury applied to the impacted joint. This result attests to the high ability of PLM to detect minute structural changes even when the trigger event (i.e., impact) is sub-critical.

In addition to the observed disruption in the surface collagen network, the 2D PLM images in the 6 weeks group qualitatively showed increased cellular volume, especially in the deep cartilage (comparing the two left images with the two right images in Fig 6.5B). It is interesting to note that this increase in the cellular volume could also be observed in the non-impact joints (between the two lower images in Fig 6.5B). It is believed that in PTOA progression, there is the initiation of intra-articular pathogenic processes, such as apoptosis of articular chondrocytes during the initial traumatic event (Punzi et al., 2016). Although we do not know the precise nature of this cellular change in the 6week groups, any change in the chondrocyte environment can affect the maintenance of the cartilage through mediation in homeostasis and reduce the ability of cells to repair (Lieberthal et al., 2015). Irrespective of minor disruption occurring in the 6 weeks cartilage tissue, there could still be the possibility of apoptosis occurring through the caspase pathway (Murray et al., 2004).

6.4.4 Experimental Notes

Any study of a group of individuals (animals or humans) must face a number of challenging factors that are difficult to control or uniformize. In OA studies, these factors could include age, weight, genetics, and difference in behavior towards repetitive use of the affected joints; all of which could influence the outcome of any quantitative study. In PTOA studies, an additional factor is the precise amount and topographical location of the impact. To the best of our ability and control, we individually put the animals to

different groups, and we monitored the specifics of the individual animals. We do not observe any trend in the influence of the age and weight of the animals on the experimental data in this study.

The fundamental limitation for any imaging study of cartilage degradation is the mismatch between the thickness of articular cartilage and the spatial resolution in imaging. Since a clinical MRI scanner is the preferred tool in hospitals for the soft tissue imaging, we use μMRI in this study, which shares the same physics and engineering as the clinical MRI. Although the transverse resolution in our μMRI is likely the highest in any MRI study of cartilage, it is still barely sufficient to study the *zonal* variations in the femoral cartilage in the rabbit model. When larger animals are used, the resolution in MRI can be relaxed, as was elaborated in the scaling law in MRI of cartilage (Xia, 2007).

In addition to the mismatch between the cartilage thickness vs imaging resolution, topographical variation in cartilage characteristics over any *single* joint surface is also a challenging factor in imaging study of OA (Badar et al., 2021). Some joints have more complicated topographical variations than some other joints (e.g., the knee joint has more complex topographies than the same in humeral and hip heads). Although we tried our best to impact at and harvest from the same location in the femur, minor uncertainty must exist, which could further mask the detection sensitivity when a group of animals are studied individually.

6.5 Conclusion

Using a single sub-critical impact to the femoral cartilage, we confirmed the development of cartilage degradation in a rabbit model, which can be detected by both μMRI and PLM. Quantitatively, there was an increase in the bulk T2 values in cartilage

which can be related to an increase of water mobility and content in the cartilage matrix, especially at the surface. PLM complements the μMRI in the detection of changes in the surface cartilage thickness and collagen organization. The data confirmed that the degradation to cartilage was localized to the surface tissue in this low-impact PTOA model of rabbit.

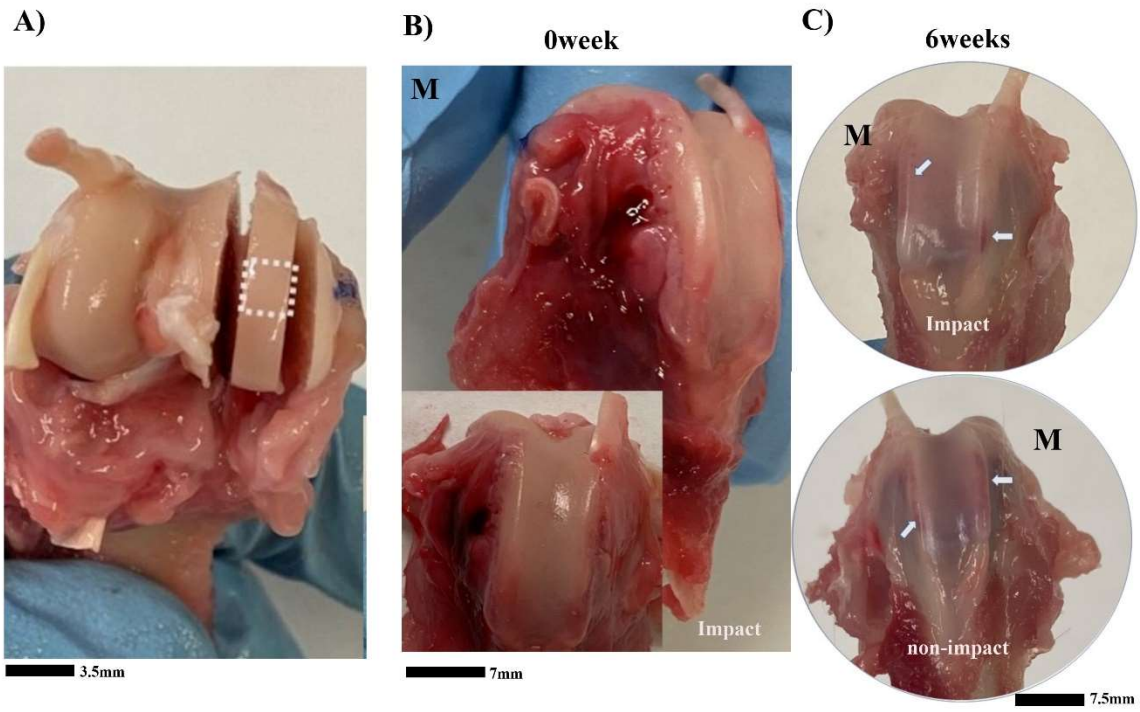

Figure 6.1 Photo of A) the cut slice of the femur with the dotted box showing where cartilage block was taken from the medial side, B) the anterior surface of the femur of a 0 week post-impact joint, and C) is a photo of a similar location of a 6week post-impact from impact and non-impacted joint. The white arrows in C) show color changes on the joint surface. M represents the medial side of the joint

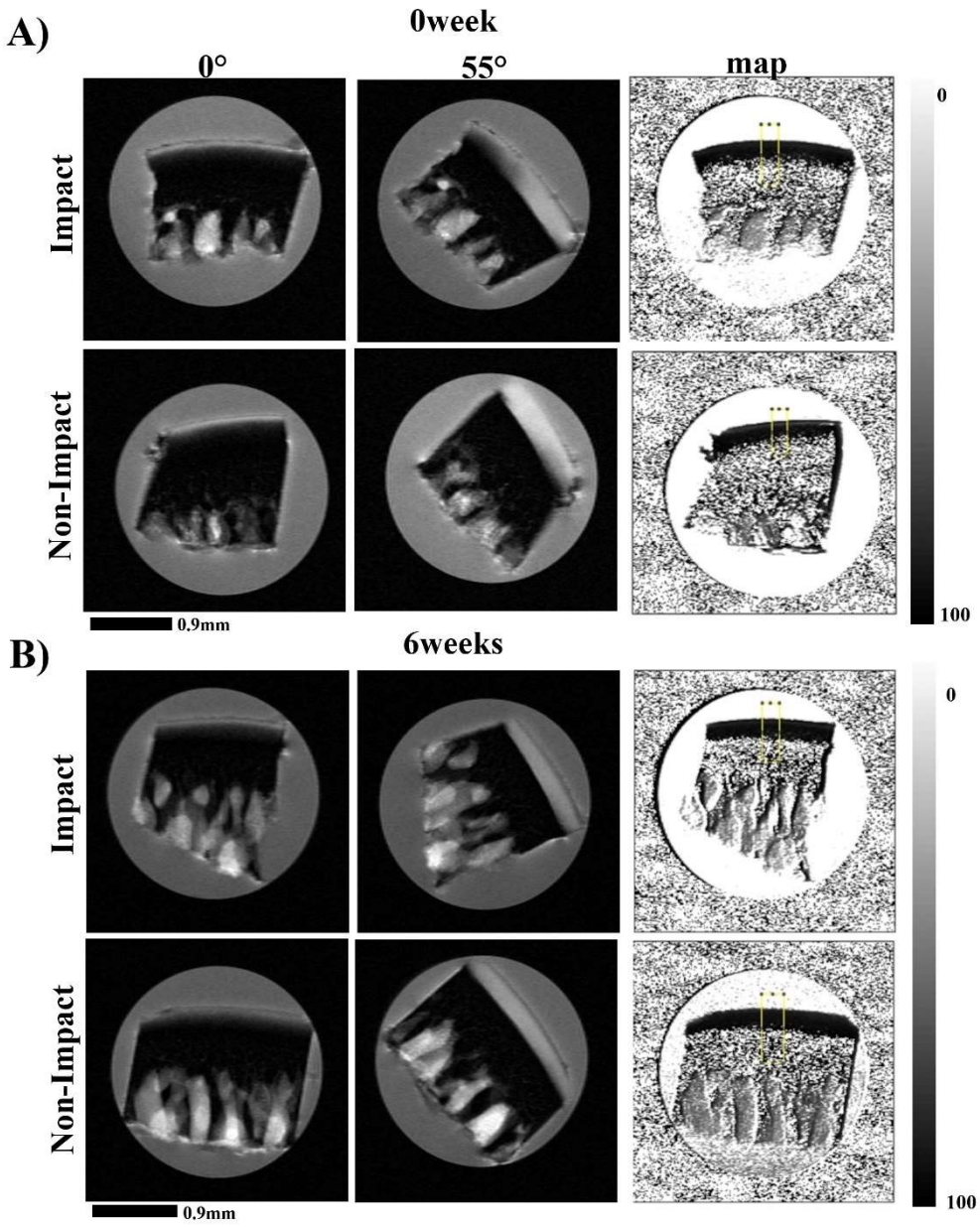

Figure 6.2 2D intensity images from μMRI T2 experiments. A) shows the intensity images of 0 week cartilage blocks from impact and non-impact joint and B) shows the intensity images from 6 weeks of cartilage blocks from impact and non-impact joint. The quantitative T2 maps are shown on the rightmost panel. Similar cartilage characteristics are observed in both sample groups

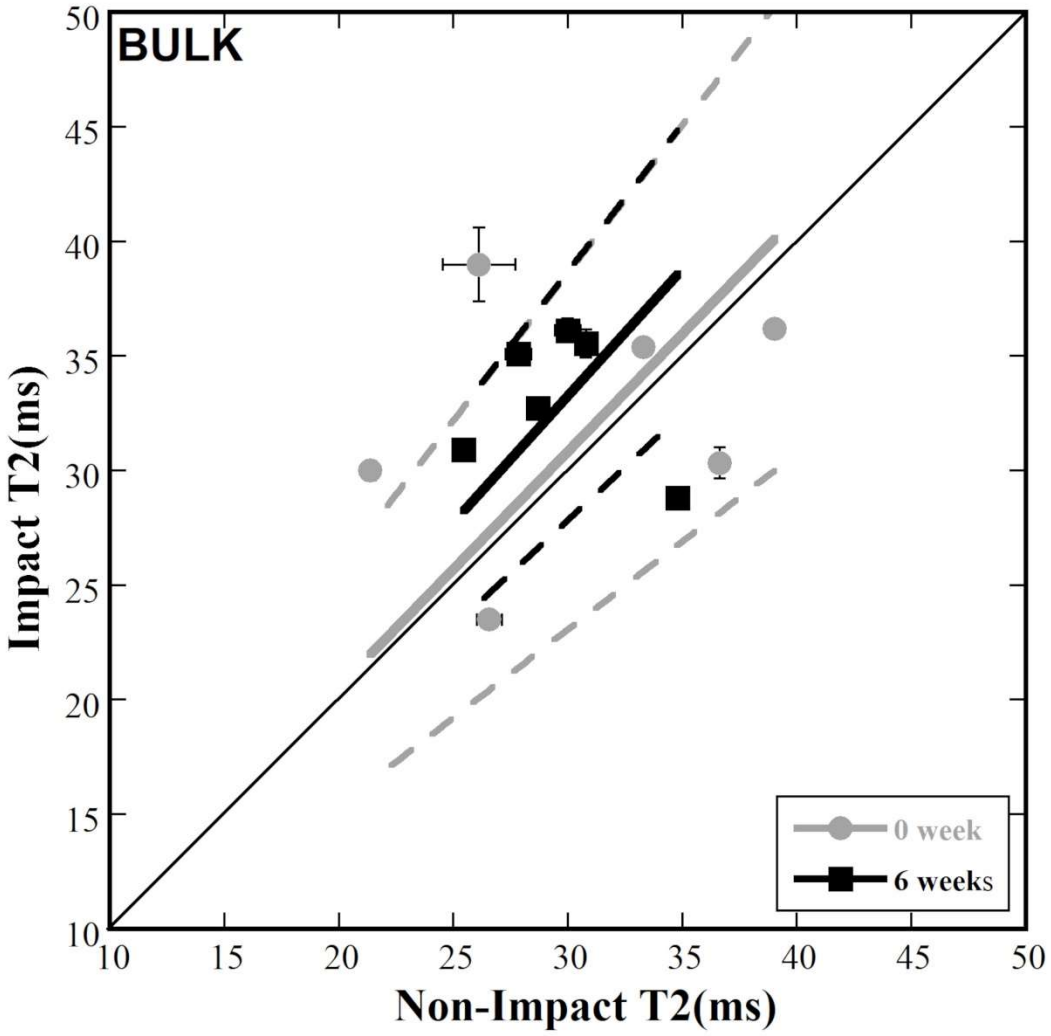

Figure 6.3 Averaged bulk T2 values of cartilage between impact and non-impact joints for 0 week and 6 weeks samples with their surface oriented at a magic angle (55˚) to the external magnetic field (B_o). Note a general increase in 6 weeks samples (fitted with a black solid line) in bulk than in 0 week samples (fitted with a grey solid line). Corresponding dashed lines represent the 95% confidence intervals for the average T2 mean values of the individual samples (markers).

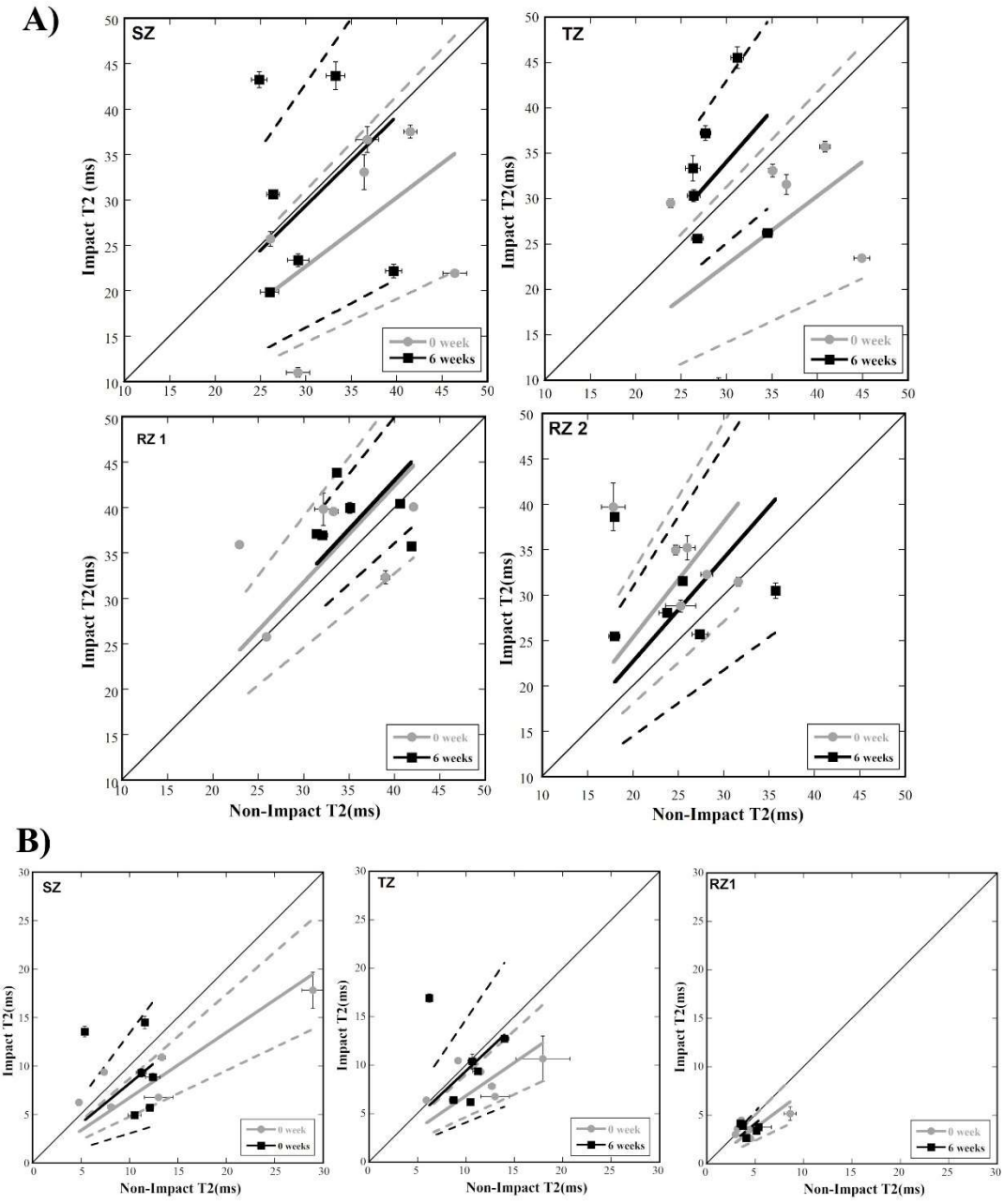

Figure 6.4 Averaged zonal T2 values of cartilage between impact and non-impact joints for 0 week and 6week samples with their surface oriented at A) at magic angle (55˚) to the external magnetic field (B_o), B) at 0˚ to B_o. The 6 weeks samples are fitted with the black solid lines and 0 week with grey solid lines. Corresponding dashed line fits represent the 95% confidence intervals for the average T2 mean values of the individual samples (markers).

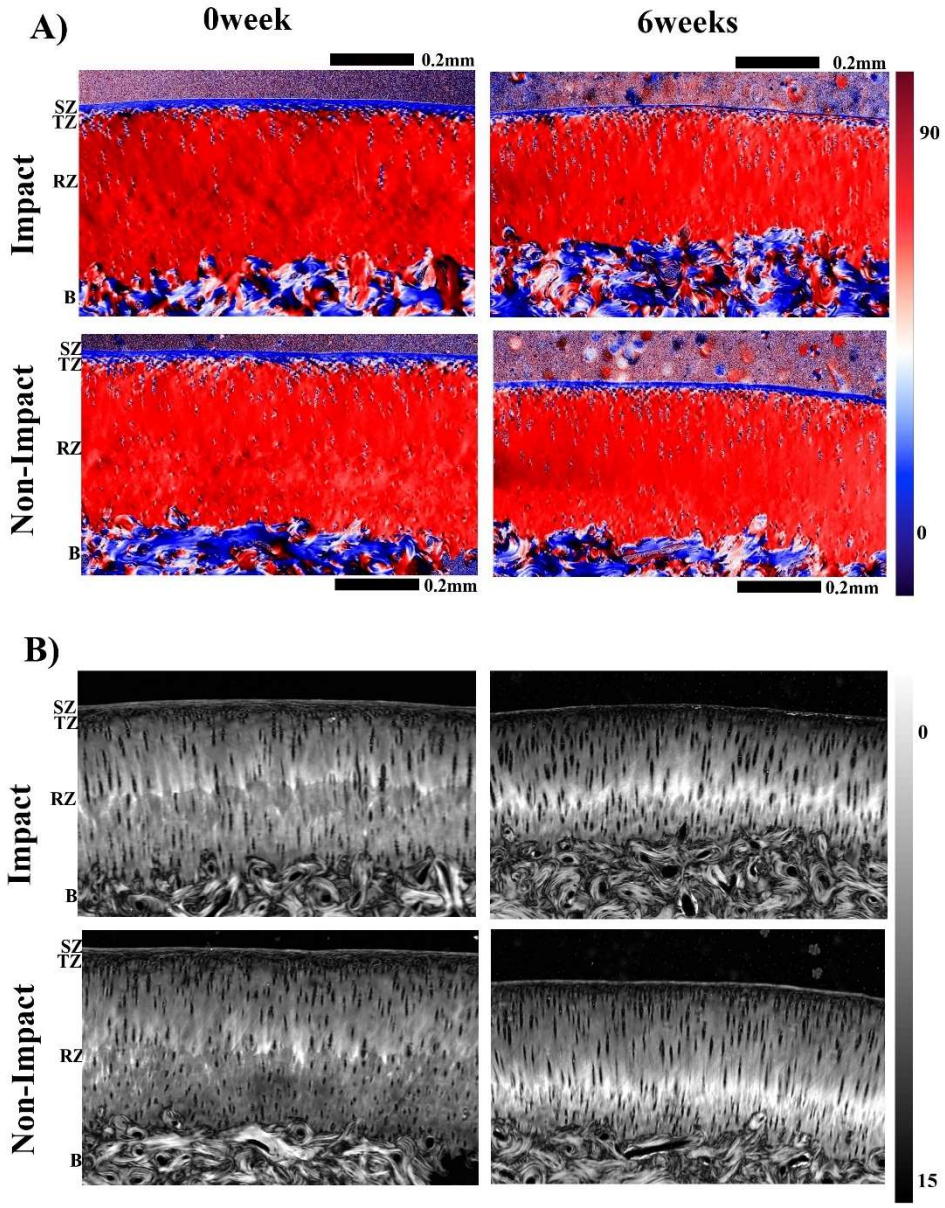

Figure 6.5 2D images of angle (A) and retardation (B) PLM technique at higher resolution 1µm/pixel for 0 week and 6 weeks samples of impact and non-impact joints. SZ, TZ, and RZ represent superficial, transitional, and radial zones.

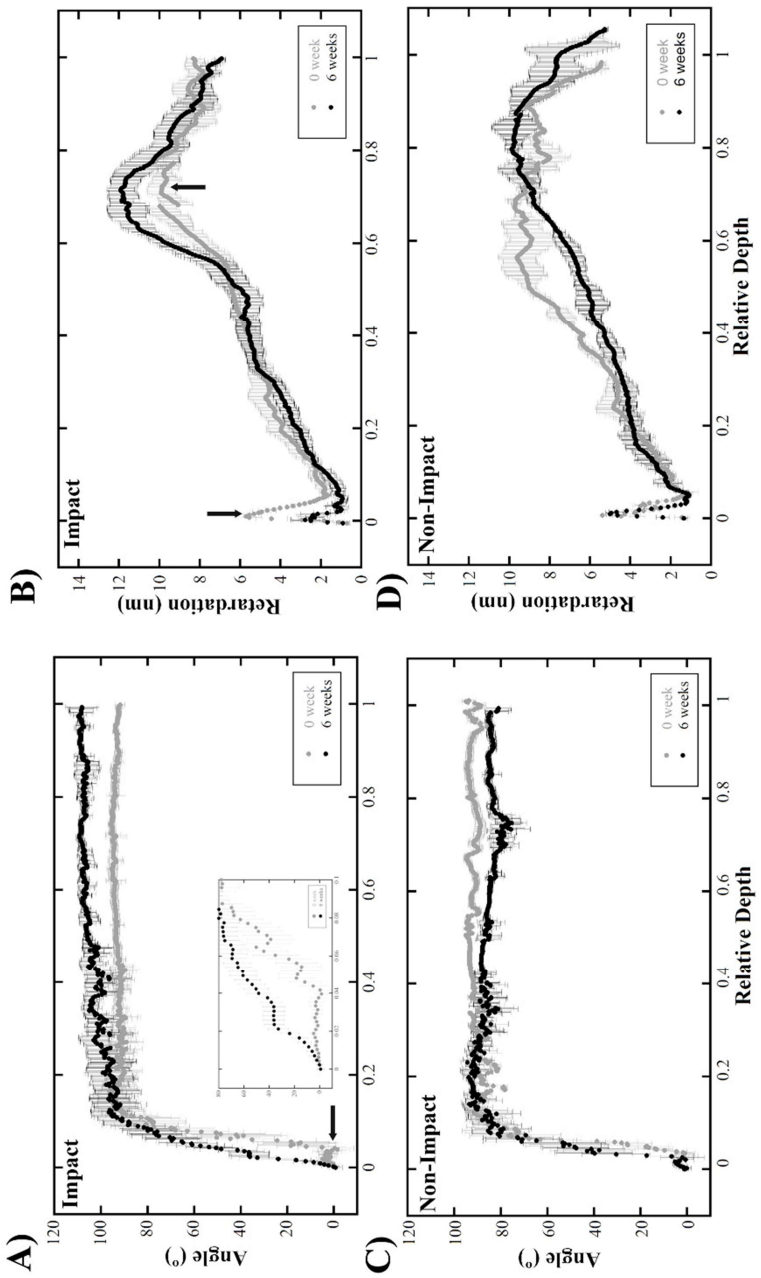

Figure 6.6 Averaged depth-dependent profiles of the angle in the impacted A) and non-impacted C) joints for 0week and 6weeks cartilage blocks. Arrow in A) shows a reduction in SZ thickness of the impact SZ thickness. Averaged depth-dependent profiles of the retardation in the impact B) and non-impacted D) for 0week and 6weeks of cartilage blocks. In B), the surface arrow points to the reduction of the retardation in the 6week group, while the deep arrow points to the estimated tide mark of the cartilage.

Table 6.1 Correlation of cartilage thickness between 0 week and 6 weeks samples from the impacted and non-impacted femurs. The p-values (PV) are for each comparison (the bold font indicates the significant difference).

	SZ (μm)			Total Tissue (μm)		
	0 week	6 weeks	PV	0 week	6 weeks	PV
μMRI Impact	14.6±2.3	11.7±0.01	1.0	298.2±17.4	286±17.0	1.0
μMRI Non-impact	17.5±2.7	19.4±1.2	1.0	313.9±24.0	306.1±16.6	1.0
PV	1.0	0.09		1.0	1.0	
PLM Impact	19.2±0.4	7.7±1.3	**0.0002**	433.0±19.4	412.0±13.0	1.0
PLM Non-impact	16.5±1.2	12.3±0.4	0.2	400.0±16.8	394.0±25.0	1.0
PV	0.1	0.1		1.0	1.0	

Table 6.2 Comparison of the averaged zonal T2 values between 0 week and 6 weeks, and between impact and non-impact femoral cartilage in μMRI. The p-values (PV) are for each comparison (the bold font indicates the significant difference).

ZONE	IMPACT T2 (ms)			NON-IMPACT T2 (ms)			SLOPE	
	0 week	6 weeks	PV	0 week	6 weeks	PV	0 week	6 weeks
A) 55˚								
BULK	30.15± 0.84	32.66± 0.51	0.06	31.89± 0.98	30.23± 0.40	0.56	1.02	1.10
SZ	26.56± 1.48	30.48± 4.3	**0.003**	35.98± 1.47	29.89± 2.30	**0.002**	0.68	0.94
TZ	26.30± 1.34	31.39± 1.04	**0.003**	34.77± 1.14	28.81± 0.47	**0.003**	0.75	1.13
RZ1	34.73± 0.77	39.02± 1.22	**0.005**	32.64± 1.20	35.77± 1.80	**0.01**	1.06	1.07
RZ2	32.54± 0.48	29.98± 0.60	0.06	24.62± 0.40	24.70± 0.41	1.0	1.02	1.10
B) 0˚								
SZ	7.81± 0.30	9.47± 0.41	**0.05**	9.35± 0.55	10.54± 0.37	0.3	0.67	0.82
TZ	8.15± 0.21	10.34± 0.50	**0.001**	10.44± 0.47	10.20± 0.34	1.0	0.68	0.94
RZ	3.44± 0.11	3.66± 0.09	1.0	3.81± 0.10	4.23± 0.23	0.3	0.74	0.83

Table 6.3 Comparison between 0 week and 6 weeks impacted, and non-impacted femoral cartilage (n=24) for PLM parameters.

	IMPACT			NON-IMPACT		
Parameter	0 week	6 weeks	PV	0 week	6 weeks	PV
Min retardation(nm)	1.66±0.14	1.09±0.08	0.4	1.56±0.18	1.57±0.32	1.0
Max retardation(nm)	10.20±0.27	11.52±0.23	0.8	8.21±0.82	8.09±1.27	1.0

Table 6.4 Biochemical analysis by the ICP-OES method, between impacted and non-impacted 0 week, and 6 weeks femoral cartilage (n=10). PV corresponds to the p-value.

	IMPACT	NON-IMPACT	PV	IMPACT	NON-IMPACT	PV
	0 week	0 week		6 weeks	6 weeks	
Water (%)	74.5 ± 1.7	77.4±2.0	0.3	77.8±1.4	76.3±2.5	0.6
GAG (mg/mL)	88.5±8.4	79.5±6.1	0.4	68.2±6.1	71.7±7.8	0.7
Calcium (mg/L)	3.2±1.0	1.73±0.4	0.2	4.3±0.7	2.5 ±0.7	0.09

CHAPTER SEVEN

SUMMARY AND FUTURE CONSIDERATIONS

Diagnosis of osteoarthritis commonly employs the use of imaging techniques such as CT and MRI, which assumes the cartilage degradation is the starting point of the disease. MRI has the potential to examine soft tissue non-invasively and without radiation and hazardous risks. In clinical OA investigations, the early detection by MRI is challenging due to a limited ability to identify small and localized structural changes by routine clinical scanners (1.5 to 3.0 T). Persons with OA especially in the knee in clinical practice often exhibit structural findings that are in the advanced stages at the time of the first diagnosis. To target the disease at the early stages of its progression, in-depth knowledge of cartilage structure must be well understood.

Preclinical studies involving osteoarthritis use animal models to achieve a level of certitude in the diagnosis and treatment of the disease. It has the potential to produce high-resolution images by the use of micro imaging techniques. The rabbit model has been one of the available options due to the closeness of its biology to humans, and its relatively low costs. The three studies contained in this dissertation make use of the rabbit model using μMRI and PLM.

In the first study (Chapter 4), the mostly overlooked structures of the patellofemoral joint of the knee, which include the prominent and largest sesamoid bone; patella (hyaline cartilage), and sesamoid fibrocartilage; suprapatella (fibrocartilage), were studied. The articular cartilage of the patella showed the classic three-zone structure; these zones are similar to the zones in the articular cartilage of the femorotibial joint of the knee. The fibrocartilage showed two distinct structures: superficial (parallel fibers),

and a deep zone (random fibers). The patellar cartilage was more anisotropic compared to the suprapatellar cartilage, which was isotropic by T2 relaxation. These features exhibit the structures' role in weight-bearing and compression and the imaging anatomic features of hyaline and fibrocartilage types were established.

The second study (Chapter 5) dealt with the changes of articular cartilage during maturation. Age is a major risk factor in OA; it plays a major role in the animal model such as population selection, experiment design, diagnosis, and treatment. The immature cartilage was found to be thicker relatively in all cartilage zones compared to mature cartilage. T2 values tend to decrease in mature cartilage than in immature cartilage reflecting lower water content or stiffer cartilage. These features allow recommendations in the choice of imaging parameters, pulse sequence selection, and tissue engineering.

Finally, in the third study (Chapter 6), the structural changes of the cartilage in the disease state were investigated as early as six weeks after an induced impact under subcritical pressure. Loading is known to be a driving force in OA disease progression. T2 values of 6-week post-impact cartilage were increased on average indicating an increase in hydration key feature in OA. PLM images from histological sections of cartilage showed reduced thickness in the superficial zone of the 6-week post-impact cartilage. This change in thickness explained the subtle disruption of cartilage collagen fibers in the early detection of the disease.

Based on these studies, high-resolution imaging is required in imaging tissues with focal changes at the microscopic level. Imaging intraarticular structures at higher resolution can detect evidence of OA at the early stages. The evidence of cartilage destruction in subcritical pressure explains the role in which loading plays in OA

progression. In preclinical studies, applying different ranges of impact in several experiments will provide stronger evidence of early changes in OA regardless of the risk factor. Other features of the disease can coexist between articular cartilage destruction and weakness of other structures in the early stages of the disease which are acted upon by loading. Some structures like ligaments, synovium, and tendons can be considered during any comprehensive investigation. Conclusively, considering other risk factors (age, gender and variation in pressure magnitude) will offer an opportunity to increase the success rate in the effective detection of early osteoarthritis.

APPENDIX

COPYRIGHT LETTERS OF PERMISSION TO REPRODUCE

Permission for Figure 2.1

SPRINGER NATURE LICENSE
TERMS AND CONDITIONS

Mar 11, 2022

This Agreement between Hannah Mantebea ("You") and Springer Nature ("Springer Nature") consists of your license details and the terms and conditions provided by Springer Nature and Copyright Clearance Center.

License Number	5265950238243
License date	Mar 11, 2022
Licensed Content Publisher	Springer Nature
Licensed Content Publication	European Journal of Human Genetics
Licensed Content Title	Genetics of the patella
Licensed Content Author	Mark E. Samuels et al
Licensed Content Date	Jan 21, 2019
Type of Use	Thesis/Dissertation
Requestor type	academic/university or research institute
Format	electronic
Portion	figures/tables/illustrations
Number of figures/tables/illustrations	1
High-res required	no

Will you be translating?	no
Circulation/distribution	1 - 29
Author of this Springer Nature content	no
Title	early detection of osteoarthritis
Institution name	oakland university
Expected presentation date	Dec 2022
Order reference number	1133
Portions	figure 1
Requestor Location	Hannah Mantebea 1794-1810 N Squirrel Rd physics department AUBURN HILLS, MI 48326 United States Attn: oakland university
Total	0.00 USD

Terms and Conditions

Springer Nature Customer Service Centre GmbH
Terms and Conditions

This agreement sets out the terms and conditions of the licence (the **Licence**) between you and **Springer Nature Customer Service Centre GmbH** (the **Licensor**). By clicking 'accept' and completing the transaction for the material (**Licensed Material**), you also confirm your acceptance of these terms and conditions.

1. Grant of License

1. 1. The Licensor grants you a personal, non-exclusive, non-transferable, world-wide licence to reproduce the Licensed Material for the purpose specified in your order only. Licences are granted for the specific use requested in the order and for no other use, subject to the conditions below.

1. 2. The Licensor warrants that it has, to the best of its knowledge, the rights to license reuse of the Licensed Material. However, you should ensure that the material you are requesting is original to the Licensor and does not carry the copyright of another entity (as credited in the published version).

1. 3. If the credit line on any part of the material you have requested indicates that it was reprinted or adapted with permission from another source, then you should also seek permission from that source to reuse the material.

2. Scope of Licence

2. 1. You may only use the Licensed Content in the manner and to the extent permitted by these Ts&Cs and any applicable laws.

2. 2. A separate licence may be required for any additional use of the Licensed Material, e.g. where a licence has been purchased for print only use, separate permission must be obtained for electronic re-use. Similarly, a licence is only valid in the language selected and does not apply for editions in other languages unless additional translation rights have been granted separately in the licence. Any content owned by third parties are expressly excluded from the licence.

2. 3. Similarly, rights for additional components such as custom editions and derivatives require additional permission and may be subject to an additional fee. Please apply to Journalpermissions@springernature.com/bookpermissions@springernature.com for these rights.

2. 4. Where permission has been granted **free of charge** for material in print, permission may also be granted for any electronic version of that work, provided that the material is incidental to your work as a whole and that the electronic version is essentially equivalent to, or substitutes for, the print version.

2. 5. An alternative scope of licence may apply to signatories of the STM Permissions Guidelines, as amended from time to time.

3. Duration of Licence

3. 1. A licence for is valid from the date of purchase ('Licence Date') at the end of the relevant period in the below table:

Scope of Licence	Duration of Licence
Post on a website	12 months
Presentations	12 months
Books and journals	Lifetime of the edition in the language purchased

4. Acknowledgement

4. 1. The Licensor's permission must be acknowledged next to the Licenced Material in print. In electronic form, this acknowledgement must be visible at the same time as the figures/tables/illustrations or abstract, and must be hyperlinked to the journal/book's

homepage. Our required acknowledgement format is in the Appendix below.

5. Restrictions on use

5. 1. Use of the Licensed Material may be permitted for incidental promotional use and minor editing privileges e.g. minor adaptations of single figures, changes of format, colour and/or style where the adaptation is credited as set out in Appendix 1 below. Any other changes including but not limited to, cropping, adapting, omitting material that affect the meaning, intention or moral rights of the author are strictly prohibited.

5. 2. You must not use any Licensed Material as part of any design or trademark.

5. 3. Licensed Material may be used in Open Access Publications (OAP) before publication by Springer Nature, but any Licensed Material must be removed from OAP sites prior to final publication.

6. Ownership of Rights

6. 1. Licensed Material remains the property of either Licensor or the relevant third party and any rights not explicitly granted herein are expressly reserved.

7. Warranty

IN NO EVENT SHALL LICENSOR BE LIABLE TO YOU OR ANY OTHER PARTY OR ANY OTHER PERSON OR FOR ANY SPECIAL, CONSEQUENTIAL, INCIDENTAL OR INDIRECT DAMAGES, HOWEVER CAUSED, ARISING OUT OF OR IN CONNECTION WITH THE DOWNLOADING, VIEWING OR USE OF THE MATERIALS REGARDLESS OF THE FORM OF ACTION, WHETHER FOR BREACH OF CONTRACT, BREACH OF WARRANTY, TORT, NEGLIGENCE, INFRINGEMENT OR OTHERWISE (INCLUDING, WITHOUT LIMITATION, DAMAGES BASED ON LOSS OF PROFITS, DATA, FILES, USE, BUSINESS OPPORTUNITY OR CLAIMS OF THIRD PARTIES), AND
WHETHER OR NOT THE PARTY HAS BEEN ADVISED OF THE POSSIBILITY OF SUCH DAMAGES. THIS LIMITATION SHALL APPLY NOTWITHSTANDING ANY FAILURE OF ESSENTIAL PURPOSE OF ANY LIMITED REMEDY PROVIDED HEREIN.

8. Limitations

8. 1. ***BOOKS ONLY:*** Where **'reuse in a dissertation/thesis'** has been selected the following terms apply: Print rights of the final author's accepted manuscript (for clarity, NOT the published version) for up to 100 copies, electronic rights for use only on a personal website or institutional repository as defined by the Sherpa guideline (www.sherpa.ac.uk/romeo/).

8. 2. For content reuse requests that qualify for permission under the STM Permissions Guidelines, which may be updated from time to time, the STM Permissions Guidelines

supersede the terms and conditions contained in this licence.

9. Termination and Cancellation

9. 1. Licences will expire after the period shown in Clause 3 (above).

9. 2. Licensee reserves the right to terminate the Licence in the event that payment is not received in full or if there has been a breach of this agreement by you.

Appendix 1 — Acknowledgements:

For Journal Content:
Reprinted by permission from [**the Licensor**]: [**Journal Publisher** (e.g. Nature/Springer/Palgrave)] [**JOURNAL NAME**] [**REFERENCE CITATION** (Article name, Author(s) Name), [**COPYRIGHT**] (year of publication)

For **Advance Online Publication papers:**
Reprinted by permission from [**the Licensor**]: [**Journal Publisher** (e.g. Nature/Springer/Palgrave)] [**JOURNAL NAME**] [**REFERENCE CITATION** (Article name, Author(s) Name), [**COPYRIGHT**] (year of publication), advance online publication, day month year (doi: 10.1038/sj.[JOURNAL ACRONYM].)

For Adaptations/Translations:
Adapted/Translated by permission from [**the Licensor**]: [**Journal Publisher** (e.g. Nature/Springer/Palgrave)] [**JOURNAL NAME**] [**REFERENCE CITATION** (Article name, Author(s) Name), [**COPYRIGHT**] (year of publication)

Note: For any republication from the British Journal of Cancer, the following credit line style applies:

Reprinted/adapted/translated by permission from [**the Licensor**]: on behalf of Cancer Research UK: : [**Journal Publisher** (e.g. Nature/Springer/Palgrave)] [**JOURNAL NAME**] [**REFERENCE CITATION** (Article name, Author(s) Name), [**COPYRIGHT**] (year of publication)

For **Advance Online Publication** papers:
Reprinted by permission from The [**the Licensor**]: on behalf of Cancer Research UK: [**Journal Publisher** (e.g. Nature/Springer/Palgrave)] [**JOURNAL NAME**] [**REFERENCE CITATION** (Article name, Author(s) Name), [**COPYRIGHT**] (year of publication), advance online publication, day month year (doi: 10.1038/sj.[JOURNAL ACRONYM])

For Book content:
Reprinted/adapted by permission from [**the Licensor**]: [**Book Publisher** (e.g. Palgrave Macmillan, Springer etc) [**Book Title**] by [**Book author**(s)] [**COPYRIGHT**] (year of publication)

Other Conditions:

Version 1.3

Questions? customercare@copyright.com or +1-855-239-3415 (toll free in the US) or +1-978-646-2777.

Permission for Figure 2.2

Creative Commons Attribution 4.0 International Public License

By exercising the Licensed Rights (defined below), You accept and agree to be bound by the terms and conditions of this Creative Commons Attribution 4.0 International Public License ("Public License"). To the extent this Public License may be interpreted as a contract, You are granted the Licensed Rights in consideration of Your acceptance of these terms and conditions, and the Licensor grants You such rights in consideration of benefits the Licensor receives from making the Licensed Material available under these terms and conditions.

Section 1 – Definitions.

a. **Adapted Material** means material subject to Copyright and Similar Rights that is derived from or based upon the Licensed Material and in which the Licensed Material is translated, altered, arranged, transformed, or otherwise modified in a manner requiring permission under the Copyright and Similar Rights held by the Licensor. For purposes of this Public License, where the Licensed Material is a musical work, performance, or sound recording, Adapted Material is always produced where the Licensed Material is synched in timed relation with a moving image.

b. **Adapter's License** means the license You apply to Your Copyright and Similar Rights in Your contributions to Adapted Material in accordance with the terms and conditions of this Public License.

c. **Copyright and Similar Rights** means copyright and/or similar rights closely related to copyright including, without limitation, performance, broadcast, sound recording, and Sui Generis Database Rights, without regard to how the rights are labeled or categorized. For purposes of this Public License, the rights specified in Section 2(b)(1)-(2) are not Copyright and Similar Rights.

d. **Effective Technological Measures** means those measures that, in the absence of proper authority, may not be circumvented under laws fulfilling obligations under Article 11 of the WIPO Copyright Treaty adopted on December 20, 1996, and/or similar international agreements.

e. **Exceptions and Limitations** means fair use, fair dealing, and/or any other exception or limitation to Copyright and Similar Rights that applies to Your use of the Licensed Material.

f. **Licensed Material** means the artistic or literary work, database, or other material to which the Licensor applied this Public License.

g. **Licensed Rights** means the rights granted to You subject to the terms and conditions of this Public License, which are limited to all Copyright and Similar Rights that apply to Your use of the Licensed Material and that the Licensor has authority to license.

h. **Licensor** means the individual(s) or entity(ies) granting rights under this Public License.

i. **Share** means to provide material to the public by any means or process that requires permission under the Licensed Rights, such as reproduction, public display, public performance, distribution, dissemination, communication, or importation, and to make material available to the public including in ways that members of the public may access the material from a place and at a time individually chosen by them.

j. **Sui Generis Database Rights** means rights other than copyright resulting from Directive 96/9/EC of the European Parliament and of the Council of 11 March 1996 on the legal protection of databases, as amended and/or succeeded, as well as other essentially equivalent rights anywhere in the world.

k. **You** means the individual or entity exercising the Licensed Rights under this Public License. **Your** has a corresponding meaning.

Section 2 – Scope.

a. **License grant**.

1. Subject to the terms and conditions of this Public License, the Licensor hereby grants You a worldwide, royalty-free, non-sublicensable, non-exclusive, irrevocable license to exercise the Licensed Rights in the Licensed Material to:

    A. reproduce and Share the Licensed Material, in whole or in part; and

    B. produce, reproduce, and Share Adapted Material.

2. Exceptions and Limitations. For the avoidance of doubt, where Exceptions and Limitations apply to Your use, this Public License does not apply, and You do not need to comply with its terms and conditions.

3. Term. The term of this Public License is specified in Section 6(a).

4. Media and formats; technical modifications allowed. The Licensor authorizes You to exercise the Licensed Rights in all media and formats whether now known or hereafter created, and to make technical modifications necessary to do so. The Licensor waives and/or agrees not to assert any right or authority to forbid You from making technical modifications necessary to exercise the Licensed Rights, including technical modifications necessary to circumvent Effective Technological Measures. For purposes of this Public License, simply making modifications authorized by this Section 2(a)(4) never produces Adapted Material.

5. Downstream recipients.

    A. Offer from the Licensor – Licensed Material. Every recipient of the Licensed Material automatically receives an offer from the Licensor to exercise the Licensed Rights under the terms and conditions of this Public License.

    B. No downstream restrictions. You may not offer or impose any additional or different terms or conditions on, or apply any Effective Technological Measures to, the Licensed Material if doing so restricts exercise of the Licensed Rights by any recipient of the Licensed Material.

6. No endorsement. Nothing in this Public License constitutes or may be construed as permission to assert or imply that You are, or that Your use of the Licensed Material is, connected with, or sponsored, endorsed, or granted official status by, the Licensor or others designated to receive attribution as provided in Section 3(a)(1)(A)(i).

b. **Other rights**.

1. Moral rights, such as the right of integrity, are not licensed under this Public License, nor are publicity, privacy, and/or other similar personality rights; however, to the extent possible, the Licensor waives and/or agrees not to assert any such rights held by the Licensor to the limited extent necessary to allow You to exercise the Licensed Rights, but not otherwise.

2. Patent and trademark rights are not licensed under this Public License.

3. To the extent possible, the Licensor waives any right to collect royalties from You for the exercise of the Licensed Rights, whether directly or through a collecting society under any voluntary or waivable statutory or compulsory licensing scheme. In all other cases the Licensor expressly reserves any right to collect such royalties.

Section 3 – License Conditions.

Your exercise of the Licensed Rights is expressly made subject to the following conditions.

a. **Attribution**.

1. If You Share the Licensed Material (including in modified form), You must:

    A. retain the following if it is supplied by the Licensor with the Licensed Material:

i. identification of the creator(s) of the Licensed Material and any others designated to receive attribution, in any reasonable manner requested by the Licensor (including by pseudonym if designated);

ii. a copyright notice;

iii. a notice that refers to this Public License;

iv. a notice that refers to the disclaimer of warranties;

v. a URI or hyperlink to the Licensed Material to the extent reasonably practicable;

B. indicate if You modified the Licensed Material and retain an indication of any previous modifications; and

C. indicate the Licensed Material is licensed under this Public License, and include the text of, or the URI or hyperlink to, this Public License.

2. You may satisfy the conditions in Section 3(a)(1) in any reasonable manner based on the medium, means, and context in which You Share the Licensed Material. For example, it may be reasonable to satisfy the conditions by providing a URI or hyperlink to a resource that includes the required information.

3. If requested by the Licensor, You must remove any of the information required by Section 3(a)(1)(A) to the extent reasonably practicable.

4. If You Share Adapted Material You produce, the Adapter's License You apply must not prevent recipients of the Adapted Material from complying with this Public License.

Section 4 – Sui Generis Database Rights.

Where the Licensed Rights include Sui Generis Database Rights that apply to Your use of the Licensed Material:

a. for the avoidance of doubt, Section 2(a)(1) grants You the right to extract, reuse, reproduce, and Share all or a substantial portion of the contents of the database;

b. if You include all or a substantial portion of the database contents in a database in which You have Sui Generis Database Rights, then the database in which You have Sui Generis Database Rights (but not its individual contents) is Adapted Material; and

c. You must comply with the conditions in Section 3(a) if You Share all or a substantial portion of the contents of the database.

For the avoidance of doubt, this Section 4 supplements and does not replace Your obligations under this Public License where the Licensed Rights include other Copyright and Similar Rights.

Section 5 – Disclaimer of Warranties and Limitation of Liability.

a. Unless otherwise separately undertaken by the Licensor, to the extent possible, the Licensor offers the Licensed Material as-is and as-available, and makes no representations or warranties of any kind concerning the Licensed Material, whether express, implied, statutory, or other. This includes, without limitation, warranties of title, merchantability, fitness for a particular purpose, non-infringement, absence of latent or other defects, accuracy, or the presence or absence of errors, whether or not known or discoverable. Where disclaimers of warranties are not allowed in full or in part, this disclaimer may not apply to You.

b. To the extent possible, in no event will the Licensor be liable to You on any legal theory (including, without limitation, negligence) or otherwise for any direct, special, indirect, incidental, consequential, punitive, exemplary, or other losses, costs, expenses, or damages arising out of this Public License or use of the Licensed Material, even if the Licensor has been advised of the possibility of such losses, costs, expenses, or damages. Where a limitation of liability is not allowed in full or in part, this limitation may not apply to You.

c. The disclaimer of warranties and limitation of liability provided above shall be interpreted in a manner that, to the extent possible, most closely approximates an absolute disclaimer and waiver of all liability.

Section 6 – Term and Termination.

a. This Public License applies for the term of the Copyright and Similar Rights licensed here. However, if You fail to comply with this Public License, then Your rights under this Public License terminate automatically.

b. Where Your right to use the Licensed Material has terminated under Section 6(a), it reinstates:

   1. automatically as of the date the violation is cured, provided it is cured within 30 days of Your discovery of the violation; or

   2. upon express reinstatement by the Licensor.

   For the avoidance of doubt, this Section 6(b) does not affect any right the Licensor may have to seek remedies for Your violations of this Public License.

c. For the avoidance of doubt, the Licensor may also offer the Licensed Material under separate terms or conditions or stop distributing the Licensed Material at any time; however, doing so will not terminate this Public License.

d. Sections 1, 5, 6, 7, and 8 survive termination of this Public License.

Section 7 – Other Terms and Conditions.

a. The Licensor shall not be bound by any additional or different terms or conditions communicated by You unless expressly agreed.

b. Any arrangements, understandings, or agreements regarding the Licensed Material not stated herein are separate from and independent of the terms and conditions of this Public License.

Section 8 – Interpretation.

a. For the avoidance of doubt, this Public License does not, and shall not be interpreted to, reduce, limit, restrict, or impose conditions on any use of the Licensed Material that could lawfully be made without permission under this Public License.

b. To the extent possible, if any provision of this Public License is deemed unenforceable, it shall be automatically reformed to the minimum extent necessary to make it enforceable. If the provision cannot be reformed, it shall be severed from this Public License without affecting the enforceability of the remaining terms and conditions.

c. No term or condition of this Public License will be waived and no failure to comply consented to unless expressly agreed to by the Licensor.

d. Nothing in this Public License constitutes or may be interpreted as a limitation upon, or waiver of, any privileges and immunities that apply to the Licensor or You, including from the legal processes of any jurisdiction or authority.

Permission for Figure 3.3

JOHN WILEY AND SONS LICENSE
TERMS AND CONDITIONS

Mar 09, 2022

This Agreement between Hannah Mantebea ("You") and John Wiley and Sons ("John Wiley and Sons") consists of your license details and the terms and conditions provided by John Wiley and Sons and Copyright Clearance Center.

License Number	5264901379704
License date	Mar 09, 2022
Licensed Content Publisher	John Wiley and Sons
Licensed Content Publication	Journal of Magnetic Resonance Imaging
Licensed Content Title	Spin echo magnetic resonance imaging
Licensed Content Author	Bernd André Jung, Matthias Weigel
Licensed Content Date	Mar 22, 2013
Licensed Content Volume	37
Licensed Content Issue	4
Licensed Content Pages	13
Type of use	Dissertation/Thesis
Requestor type	University/Academic
Format	Electronic

Portion	Figure/table
Number of figures/tables	1
Will you be translating?	No
Title	early detection of osteoarthritis
Institution name	oakland university
Expected presentation date	Dec 2022
Order reference number	2233
Portions	figure 3
Requestor Location	Hannah Mantebea 1794-1810 N Squirrel Rd physics department AUBURN HILLS, MI 48326 United States Attn: oakland university
Publisher Tax ID	EU826007151
Total	0.00 USD

Terms and Conditions

TERMS AND CONDITIONS

This copyrighted material is owned by or exclusively licensed to John Wiley & Sons, Inc. or one of its group companies (each a"Wiley Company") or handled on behalf of a society with which a Wiley Company has exclusive publishing rights in relation to a particular work (collectively "WILEY"). By clicking "accept" in connection with completing this licensing transaction, you agree that the following terms and conditions apply to this transaction (along with the billing and payment terms and conditions established by the Copyright Clearance Center Inc., ("CCC's Billing and Payment terms and conditions"), at the time that you opened your RightsLink account (these are available at any time at http://myaccount.copyright.com).

Terms and Conditions

- The materials you have requested permission to reproduce or reuse (the "Wiley Materials") are protected by copyright.

- You are hereby granted a personal, non-exclusive, non-sub licensable (on a stand-alone basis), non-transferable, worldwide, limited license to reproduce the Wiley Materials for the purpose specified in the licensing process. This license, **and any CONTENT (PDF or image file) purchased as part of your order,** is for a one-time use only and limited to any maximum distribution number specified in the license. The first instance of republication or reuse granted by this license must be completed within two years of the date of the grant of this license (although copies prepared before the end date may be distributed thereafter). The Wiley Materials shall not be used in any other manner or for any other purpose, beyond what is granted in the license. Permission is granted subject to an appropriate acknowledgement given to the author, title of the material/book/journal and the publisher. You shall also duplicate the copyright notice that appears in the Wiley publication in your use of the Wiley Material. Permission is also granted on the understanding that nowhere in the text is a previously published source acknowledged for all or part of this Wiley Material. Any third party content is expressly excluded from this permission.

- With respect to the Wiley Materials, all rights are reserved. Except as expressly granted by the terms of the license, no part of the Wiley Materials may be copied, modified, adapted (except for minor reformatting required by the new Publication), translated, reproduced, transferred or distributed, in any form or by any means, and no derivative works may be made based on the Wiley Materials without the prior permission of the respective copyright owner.**For STM Signatory Publishers clearing permission under the terms of the STM Permissions Guidelines only, the terms of the license are extended to include subsequent editions and for editions in other languages, provided such editions are for the work as a whole in situ and does not involve the separate exploitation of the permitted figures or extracts,** You may not alter, remove or suppress in any manner any copyright, trademark or other notices displayed by the Wiley Materials. You may not license, rent, sell, loan, lease, pledge, offer as security, transfer or assign the Wiley Materials on a stand-alone basis, or any of the rights granted to you hereunder to any other person.

- The Wiley Materials and all of the intellectual property rights therein shall at all times remain the exclusive property of John Wiley & Sons Inc, the Wiley Companies, or their respective licensors, and your interest therein is only that of having possession of and the right to reproduce the Wiley Materials pursuant to Section 2 herein during the continuance of this Agreement. You agree that you own no right, title or interest in or to the Wiley Materials or any of the intellectual property rights therein. You shall have no rights hereunder other than the license as provided for above in Section 2. No right, license or interest to any trademark, trade name, service mark or other branding ("Marks") of WILEY or its licensors is granted hereunder, and you agree that you shall not assert any such right, license or interest with respect thereto

- NEITHER WILEY NOR ITS LICENSORS MAKES ANY WARRANTY OR REPRESENTATION OF ANY KIND TO YOU OR ANY THIRD PARTY, EXPRESS, IMPLIED OR STATUTORY, WITH RESPECT TO THE MATERIALS OR THE ACCURACY OF ANY INFORMATION CONTAINED IN THE MATERIALS, INCLUDING, WITHOUT LIMITATION, ANY IMPLIED WARRANTY OF MERCHANTABILITY, ACCURACY, SATISFACTORY

QUALITY, FITNESS FOR A PARTICULAR PURPOSE, USABILITY, INTEGRATION OR NON-INFRINGEMENT AND ALL SUCH WARRANTIES ARE HEREBY EXCLUDED BY WILEY AND ITS LICENSORS AND WAIVED BY YOU.

- WILEY shall have the right to terminate this Agreement immediately upon breach of this Agreement by you.
- You shall indemnify, defend and hold harmless WILEY, its Licensors and their respective directors, officers, agents and employees, from and against any actual or threatened claims, demands, causes of action or proceedings arising from any breach of this Agreement by you.
- IN NO EVENT SHALL WILEY OR ITS LICENSORS BE LIABLE TO YOU OR ANY OTHER PARTY OR ANY OTHER PERSON OR ENTITY FOR ANY SPECIAL, CONSEQUENTIAL, INCIDENTAL, INDIRECT, EXEMPLARY OR PUNITIVE DAMAGES, HOWEVER CAUSED, ARISING OUT OF OR IN CONNECTION WITH THE DOWNLOADING, PROVISIONING, VIEWING OR USE OF THE MATERIALS REGARDLESS OF THE FORM OF ACTION, WHETHER FOR BREACH OF CONTRACT, BREACH OF WARRANTY, TORT, NEGLIGENCE, INFRINGEMENT OR OTHERWISE (INCLUDING, WITHOUT LIMITATION, DAMAGES BASED ON LOSS OF PROFITS, DATA, FILES, USE, BUSINESS OPPORTUNITY OR CLAIMS OF THIRD PARTIES), AND WHETHER OR NOT THE PARTY HAS BEEN ADVISED OF THE POSSIBILITY OF SUCH DAMAGES. THIS LIMITATION SHALL APPLY NOTWITHSTANDING ANY FAILURE OF ESSENTIAL PURPOSE OF ANY LIMITED REMEDY PROVIDED HEREIN.
- Should any provision of this Agreement be held by a court of competent jurisdiction to be illegal, invalid, or unenforceable, that provision shall be deemed amended to achieve as nearly as possible the same economic effect as the original provision, and the legality, validity and enforceability of the remaining provisions of this Agreement shall not be affected or impaired thereby.
- The failure of either party to enforce any term or condition of this Agreement shall not constitute a waiver of either party's right to enforce each and every term and condition of this Agreement. No breach under this agreement shall be deemed waived or excused by either party unless such waiver or consent is in writing signed by the party granting such waiver or consent. The waiver by or consent of a party to a breach of any provision of this Agreement shall not operate or be construed as a waiver of or consent to any other or subsequent breach by such other party.
- This Agreement may not be assigned (including by operation of law or otherwise) by you without WILEY's prior written consent.
- Any fee required for this permission shall be non-refundable after thirty (30) days from receipt by the CCC.
- These terms and conditions together with CCC's Billing and Payment terms and conditions (which are incorporated herein) form the entire agreement between you and WILEY concerning this licensing transaction and (in the absence of fraud) supersedes all prior agreements and representations of the parties, oral or written. This Agreement may not be amended except in writing signed by both parties. This Agreement shall be binding upon and inure to the benefit of the parties' successors, legal representatives,

and authorized assigns.

- In the event of any conflict between your obligations established by these terms and conditions and those established by CCC's Billing and Payment terms and conditions, these terms and conditions shall prevail.
- WILEY expressly reserves all rights not specifically granted in the combination of (i) the license details provided by you and accepted in the course of this licensing transaction, (ii) these terms and conditions and (iii) CCC's Billing and Payment terms and conditions.
- This Agreement will be void if the Type of Use, Format, Circulation, or Requestor Type was misrepresented during the licensing process.
- This Agreement shall be governed by and construed in accordance with the laws of the State of New York, USA, without regards to such state's conflict of law rules. Any legal action, suit or proceeding arising out of or relating to these Terms and Conditions or the breach thereof shall be instituted in a court of competent jurisdiction in New York County in the State of New York in the United States of America and each party hereby consents and submits to the personal jurisdiction of such court, waives any objection to venue in such court and consents to service of process by registered or certified mail, return receipt requested, at the last known address of such party.

WILEY OPEN ACCESS TERMS AND CONDITIONS

Wiley Publishes Open Access Articles in fully Open Access Journals and in Subscription journals offering Online Open. Although most of the fully Open Access journals publish open access articles under the terms of the Creative Commons Attribution (CC BY) License only, the subscription journals and a few of the Open Access Journals offer a choice of Creative Commons Licenses. The license type is clearly identified on the article.

The Creative Commons Attribution License

The Creative Commons Attribution License (CC-BY) allows users to copy, distribute and transmit an article, adapt the article and make commercial use of the article. The CC-BY license permits commercial and non-

Creative Commons Attribution Non-Commercial License

The Creative Commons Attribution Non-Commercial (CC-BY-NC)License permits use, distribution and reproduction in any medium, provided the original work is properly cited and is not used for commercial purposes.(see below)

Creative Commons Attribution-Non-Commercial-NoDerivs License

The Creative Commons Attribution Non-Commercial-NoDerivs License (CC-BY-NC-ND) permits use, distribution and reproduction in any medium, provided the original work is properly cited, is not used for commercial purposes and no modifications or adaptations are made. (see below)

Use by commercial "for-profit" organizations

Use of Wiley Open Access articles for commercial, promotional, or marketing purposes requires further explicit permission from Wiley and will be subject to a fee.

Further details can be found on Wiley Online Library
http://olabout.wiley.com/WileyCDA/Section/id-410895.html

Other Terms and Conditions:

v1.10 Last updated September 2015

Questions? customercare@copyright.com or +1-855-239-3415 (toll free in the US) or +1-978-646-2777.

Permission to produce chapter 5 in its entirety

JOHN WILEY AND SONS LICENSE
TERMS AND CONDITIONS

Dec 19, 2022

This Agreement between Hannah Mantebea ("You") and John Wiley and Sons ("John Wiley and Sons") consists of your license details and the terms and conditions provided by John Wiley and Sons and Copyright Clearance Center.

License Number	5452521421064
License date	Dec 19, 2022
Licensed Content Publisher	John Wiley and Sons
Licensed Content Publication	Journal of Anatomy
Licensed Content Title	Structural differences between immature and mature articular cartilage of rabbits by microscopic MRI and polarized light microscopy
Licensed Content Author	Hannah Mantebea, Syeda Batool, Amanveer Singh, et al
Licensed Content Date	Jan 3, 2022
Licensed Content Volume	240
Licensed Content Issue	6
Licensed Content Pages	11

Type of use	Dissertation/Thesis
Requestor type	Author of this Wiley article
Format	Electronic
Portion	Full article
Will you be translating?	No
Title	early detection of osteoarthritis
Institution name	oakland university
Expected presentation date	Dec 2022
Order reference number	120
Requestor Location	Hannah Mantebea 2645 beacon hills ct apt 206 AUBURN HILLS, MI 48326 United States Attn: oakland university
Publisher Tax ID	EU826007151
Total	0.00 USD

Terms and Conditions

TERMS AND CONDITIONS

This copyrighted material is owned by or exclusively licensed to John Wiley & Sons, Inc. or one of its group companies (each a"Wiley Company") or handled on behalf of a society with which a Wiley Company has exclusive publishing rights in relation to a particular work

(collectively "WILEY"). By clicking "accept" in connection with completing this licensing transaction, you agree that the following terms and conditions apply to this transaction (along with the billing and payment terms and conditions established by the Copyright Clearance Center Inc., ("CCC's Billing and Payment terms and conditions"), at the time that you opened your RightsLink account (these are available at any time at http://myaccount.copyright.com).

Terms and Conditions

- The materials you have requested permission to reproduce or reuse (the "Wiley Materials") are protected by copyright.
- You are hereby granted a personal, non-exclusive, non-sub licensable (on a stand-alone basis), non-transferable, worldwide, limited license to reproduce the Wiley Materials for the purpose specified in the licensing process. This license, **and any CONTENT (PDF or image file) purchased as part of your order,** is for a one-time use only and limited to any maximum distribution number specified in the license. The first instance of republication or reuse granted by this license must be completed within two years of the date of the grant of this license (although copies prepared before the end date may be distributed thereafter). The Wiley Materials shall not be used in any other manner or for any other purpose, beyond what is granted in the license. Permission is granted subject to an appropriate acknowledgement given to the author, title of the material/book/journal and the publisher. You shall also duplicate the copyright notice that appears in the Wiley publication in your use of the Wiley Material. Permission is also granted on the understanding that nowhere in the text is a previously published source acknowledged for all or part of this Wiley Material. Any third party content is expressly excluded from this permission.
- With respect to the Wiley Materials, all rights are reserved. Except as expressly granted by the terms of the license, no part of the Wiley Materials may be copied, modified, adapted (except for minor reformatting required by the new Publication), translated, reproduced, transferred or distributed, in any form or by any means, and no derivative works may be made based on the Wiley Materials without the prior permission of the respective copyright owner.**For STM Signatory Publishers clearing permission under the terms of the STM Permissions Guidelines only, the terms of the license are extended to include subsequent editions and for editions in other languages, provided such editions are for the work as a whole in situ and does not involve the separate exploitation of the permitted figures or extracts,** You may not alter, remove or suppress in any manner any copyright, trademark or other notices displayed by the Wiley Materials. You may not license, rent, sell, loan, lease, pledge, offer as security, transfer or assign the Wiley Materials on a stand-alone basis, or any of the rights granted to you hereunder to any other person.
- The Wiley Materials and all of the intellectual property rights therein shall at all times remain the exclusive property of John Wiley & Sons Inc, the Wiley Companies, or their respective licensors, and your interest therein is only that of having possession of and the right to reproduce the Wiley Materials pursuant to Section 2 herein during the continuance of this Agreement. You agree that you own no right, title or interest in or to the Wiley Materials or any of the intellectual property rights therein. You shall have no rights hereunder other than the license as provided for above in Section 2. No right, license or interest to any trademark, trade name, service mark or other branding ("Marks") of WILEY or its licensors is granted hereunder, and you agree that you shall

not assert any such right, license or interest with respect thereto

- NEITHER WILEY NOR ITS LICENSORS MAKES ANY WARRANTY OR REPRESENTATION OF ANY KIND TO YOU OR ANY THIRD PARTY, EXPRESS, IMPLIED OR STATUTORY, WITH RESPECT TO THE MATERIALS OR THE ACCURACY OF ANY INFORMATION CONTAINED IN THE MATERIALS, INCLUDING, WITHOUT LIMITATION, ANY IMPLIED WARRANTY OF MERCHANTABILITY, ACCURACY, SATISFACTORY QUALITY, FITNESS FOR A PARTICULAR PURPOSE, USABILITY, INTEGRATION OR NON-INFRINGEMENT AND ALL SUCH WARRANTIES ARE HEREBY EXCLUDED BY WILEY AND ITS LICENSORS AND WAIVED BY YOU.

- WILEY shall have the right to terminate this Agreement immediately upon breach of this Agreement by you.

- You shall indemnify, defend and hold harmless WILEY, its Licensors and their respective directors, officers, agents and employees, from and against any actual or threatened claims, demands, causes of action or proceedings arising from any breach of this Agreement by you.

- IN NO EVENT SHALL WILEY OR ITS LICENSORS BE LIABLE TO YOU OR ANY OTHER PARTY OR ANY OTHER PERSON OR ENTITY FOR ANY SPECIAL, CONSEQUENTIAL, INCIDENTAL, INDIRECT, EXEMPLARY OR PUNITIVE DAMAGES, HOWEVER CAUSED, ARISING OUT OF OR IN CONNECTION WITH THE DOWNLOADING, PROVISIONING, VIEWING OR USE OF THE MATERIALS REGARDLESS OF THE FORM OF ACTION, WHETHER FOR BREACH OF CONTRACT, BREACH OF WARRANTY, TORT, NEGLIGENCE, INFRINGEMENT OR OTHERWISE (INCLUDING, WITHOUT LIMITATION, DAMAGES BASED ON LOSS OF PROFITS, DATA, FILES, USE, BUSINESS OPPORTUNITY OR CLAIMS OF THIRD PARTIES), AND WHETHER OR NOT THE PARTY HAS BEEN ADVISED OF THE POSSIBILITY OF SUCH DAMAGES. THIS LIMITATION SHALL APPLY NOTWITHSTANDING ANY FAILURE OF ESSENTIAL PURPOSE OF ANY LIMITED REMEDY PROVIDED HEREIN.

- Should any provision of this Agreement be held by a court of competent jurisdiction to be illegal, invalid, or unenforceable, that provision shall be deemed amended to achieve as nearly as possible the same economic effect as the original provision, and the legality, validity and enforceability of the remaining provisions of this Agreement shall not be affected or impaired thereby.

- The failure of either party to enforce any term or condition of this Agreement shall not constitute a waiver of either party's right to enforce each and every term and condition of this Agreement. No breach under this agreement shall be deemed waived or excused by either party unless such waiver or consent is in writing signed by the party granting such waiver or consent. The waiver by or consent of a party to a breach of any provision of this Agreement shall not operate or be construed as a waiver of or consent to any other or subsequent breach by such other party.

- This Agreement may not be assigned (including by operation of law or otherwise) by you without WILEY's prior written consent.

- Any fee required for this permission shall be non-refundable after thirty (30) days from receipt by the CCC.

- These terms and conditions together with CCC's Billing and Payment terms and conditions (which are incorporated herein) form the entire agreement between you and WILEY concerning this licensing transaction and (in the absence of fraud) supersedes all prior agreements and representations of the parties, oral or written. This Agreement may not be amended except in writing signed by both parties. This Agreement shall be binding upon and inure to the benefit of the parties' successors, legal representatives, and authorized assigns.

- In the event of any conflict between your obligations established by these terms and conditions and those established by CCC's Billing and Payment terms and conditions, these terms and conditions shall prevail.

- WILEY expressly reserves all rights not specifically granted in the combination of (i) the license details provided by you and accepted in the course of this licensing transaction, (ii) these terms and conditions and (iii) CCC's Billing and Payment terms and conditions.

- This Agreement will be void if the Type of Use, Format, Circulation, or Requestor Type was misrepresented during the licensing process.

- This Agreement shall be governed by and construed in accordance with the laws of the State of New York, USA, without regards to such state's conflict of law rules. Any legal action, suit or proceeding arising out of or relating to these Terms and Conditions or the breach thereof shall be instituted in a court of competent jurisdiction in New York County in the State of New York in the United States of America and each party hereby consents and submits to the personal jurisdiction of such court, waives any objection to venue in such court and consents to service of process by registered or certified mail, return receipt requested, at the last known address of such party.

WILEY OPEN ACCESS TERMS AND CONDITIONS

Wiley Publishes Open Access Articles in fully Open Access Journals and in Subscription journals offering Online Open. Although most of the fully Open Access journals publish open access articles under the terms of the Creative Commons Attribution (CC BY) License only, the subscription journals and a few of the Open Access Journals offer a choice of Creative Commons Licenses. The license type is clearly identified on the article.

The Creative Commons Attribution License

The Creative Commons Attribution License (CC-BY) allows users to copy, distribute and transmit an article, adapt the article and make commercial use of the article. The CC-BY license permits commercial and non-

Creative Commons Attribution Non-Commercial License

The Creative Commons Attribution Non-Commercial (CC-BY-NC)License permits use, distribution and reproduction in any medium, provided the original work is properly cited and is not used for commercial purposes.(see below)

Creative Commons Attribution-Non-Commercial-NoDerivs License

REFERENCE

Abulhasan, J. F., & Grey, M. J. (2017). Anatomy and physiology of knee stability. *Journal of Functional Morphology and Kinesiology*, *2*(4). https://doi.org/10.3390/jfmk2040034

Alhadlaq, H. A., Xia, Y., Hansen, F. M., Les, C. M., & Lust, G. (2007). Morphological changes in articular cartilage due to static compression: polarized light microscopy study. *Connective Tissue Research*, *48*(2), 76–84. https://doi.org/10.1080/03008200601130950

Alhadlaq, H. A., Xia, Y., Moody, J. B., & Matyas, J. R. (2004). Detecting structural changes in early experimental osteoarthritis of tibial cartilage by microscopic magnetic resonance imaging and polarised light microscopy. *Annals of the Rheumatic Diseases*, *63*(6), 709–717. https://doi.org/10.1136/ard.2003.011783

Alnahdi, A. H., Zeni, J. A., & Snyder-Mackler, L. (2012). Muscle impairments in patients with knee osteoarthritis. *Sports Health*, *4*(4), 284–292. https://doi.org/10.1177/1941738112445726

Arzi, B., Wisner, E. R., Huey, D. J., Kass, P. H., Hu, J., & Athanasiou, K. A. (2015). *Naturally-occuring osteoarthritis in the domestic rabbit: possible implications for bioengineeering research*. *41*(1), 20–25. https://doi.org/10.1038/laban0112-20.Naturally-occurring

Athanasiou, K. A., Rosenwasser, M. P., Buckwalter, J. A., Malinin, T. I., & Mow, V. C. (1991). Interspecies comparisons of in situ intrinsic mechanical properties of distal femoral cartilage. *Journal of Orthopaedic Research*, *9*(3), 330–340. https://doi.org/10.1002/jor.1100090304

Badar, F., Lee, J., Qu, X., & Xia, Y. (2021). Topographical and zonal patterns of T2 relaxation in osteoarthritic tibial cartilage by low- and high-resolution MRI. *Magnetic Resonance Imaging*, *78*(October 2020), 98–108. https://doi.org/10.1016/j.mri.2021.01.002

Badar, F., & Xia, Y. (2022). The interface region between articular cartilage and bone by μMRI and PLM at microscopic resolutions. *Microscopy Research and Technique*, *85*(4), 1483–1493. https://doi.org/10.1002/jemt.24011

Batool, S., Hammami, M., Mantebea, H., Badar, F., Xia, Y., Title, J., Number, A., Orcid, F., Commons, C., Open, S., Portal, A., Edit, S., Open, S., Portal, A., Charge, A. P., Open, S., Portal, A., & Approval, E. (2022). Location-Specific Study of Young Rabbit Femoral Cartilage by Quantitative μMRI and Polarized Light Microscopy. *Cartilage*, *13*(1), 194760352210851. https://doi.org/10.1177/19476035221085143

Batool, S., Mahar, R., Badar, F., Tetmeyer, A., & Xia, Y. (2020). Quantitative μMRI and PLM study of rabbit humeral and femoral head cartilage at sub-10 μm resolutions. *Journal of Orthopaedic Research*, *38*(5), 1052–1062. https://doi.org/10.1002/jor.24547

Baum, T., Stehling, C., Joseph, G. B., Carballido-Gamio, J., Schwaiger, B. J., Müller-Höcker, C., Nevitt, M. C., Lynch, J., McCulloch, C. E., & Link, T. M. (2012). Changes in knee cartilage T2 values over 24 months in subjects with and without risk factors for knee osteoarthritis and their association with focal knee lesions at baseline: data from the osteoarthritis initiative. *Journal of Magnetic Resonance Imaging : JMRI*, *35*(2), 370–378. https://doi.org/10.1002/jmri.22834

Benedek, T. G. (2006). A history of the understanding of cartilage. *Osteoarthritis and Cartilage*, *14*(3), 203–209. https://doi.org/10.1016/j.joca.2005.08.014

Benjamin, M., & Ralphs, J. R. (1998). Fibrocartilage in tendons and ligaments - An adaptation to compressive load. *Journal of Anatomy*, *193*(4), 481–494. https://doi.org/10.1017/S0021878298004300

Bland, Y. S., & Ashhurst, D. E. (1997). Fetal and postnatal development of the patella, patellar tendon and suprapatella in the rabbit ; changes in the distribution of the fibrillar collagens. *Journal of Anatomy*. 190(3) 372-342. https://doi.org/10.1017/S0021878296001720

Bonucci, E., & Gomez, S. (2012). Cartilage Calcification. *Advanced Topics in Biomineralization*, *February 2012*. https://doi.org/10.5772/31249

Brown, T., Johnston, R., Saltzman, C., Marsh, J., & Buckwalter, J. (2006). Posttraumatic Osteoarthritis: A First Estimate of Incidence, Prevalence, and Burden of Disease. *Journal of Orthopaedic Trauma*, *20*, 739–744. https://doi.org/10.1097/01.bot.0000246468.80635.ef

Buckwalter, J. A., Mankin, H. J., & Grodzinsky, A. J. (2005).Articular Cartilage and osteoarthritis *AAOS* 54, 466–480.

Camarero-Espinosa, S., Rothen-Rutishauser, B., Foster, E. J., & Weder, C. (2016). Articular cartilage: From formation to tissue engineering. *Biomater. Sci.*, *4*, 734–767.

Carballo, C. B., Nakagawa, Y., Sekiya, I., & Rodeo, S. A. (2017). Basic science of articular artilage. *Clin. Sports Med.*, *36*, 413–425.

Carbone, A., & Rodeo, S. (2017). Review of current understanding of post-traumatic osteoarthritis resulting from sports injuries. *Journal of Orthopaedic Research*, *35*(3), 397–405. https://doi.org/10.1002/jor.23341

Dare, D., & Rodeo, S. (2014). Mechanisms of post-traumatic osteoarthritis after ACL injury. *Current Rheumatology Reports*, *16*(10), 448. https://doi.org/10.1007/s11926-014-0448-1

Davies, R. L., & Kuiper, N. J. (2019). Regenerative Medicine: A Review of the evolution of autologous chondrocyte implantation (ACI) Therapy. *Bioengineering*, *6*(1), 1–16. https://doi.org/10.3390/bioengineering6010022

DeHaven, K. E. (1980). Diagnosis of acute knee injuries with hemarthrosis. *The American Journal of Sports Medicine*, *8*(1), 9–14. https://doi.org/10.1177/036354658000800102

Ellison, A., & Berg, E. (1985). Embryology, anatomy, and function of the anterior cruciate ligament. *Orthop. Clin. N. Am.*, *16*, 3–14.

Englund, M., Roemer, F. W., Hayashi, D., Crema, M. D., & Guermazi, A. (2012). Meniscus pathology, osteoarthritis and the treatment controversy. *Nature Reviews. Rheumatology*, *8*(7), 412–419. https://doi.org/10.1038/nrrheum.2012.69

Fairweather-Tait, S. J., Wawer, A. A., Gillings, R., Jennings, A., & Myint, P. K. (2014). Iron status in the elderly. *Mechanisms of Ageing and Development*, *136–137*, 22–28. https://doi.org/10.1016/j.mad.2013.11.005

Felson, D. T., & Hodgson, R. (2014). Identifying and treating preclinical and early osteoarthritis. *Rheumatic Disease Clinics of North America*, *40*(4), 699–710. https://doi.org/10.1016/j.rdc.2014.07.012

Fernandes, J. C., Martel-Pelletier, J., & Pelletier, J. P. (2002). The role of cytokines in osteoarthritis pathophysiology. *Biorheology*, *39(1-2)*, 237–246.

Flandry, F., & Hommel, G. (2011). Normal anatomy and biomechanics of the knee. *Sports Medicine and Arthroscopy Review*, *19*(2), 82–92. https://doi.org/10.1097/JSA.0b013e318210c0aa

Fox, A. J. S., Wanivenhaus, F., & Rodeo, S. A. (2012). The basic science of the patella: structure, composition, and function. *The Journal of Knee Surgery*, *25*(2), 127–141. https://doi.org/10.1055/s-0032-1313741

Friedrich, K. M., Shepard, T., de Oliveira, V. S., Wang, L., Babb, J. S., Schweitzer, M., & Regatte, R. (2009). T2 measurements of cartilage in osteoarthritis patients with meniscal tears. *AJR. American Journal of Roentgenology*, *193*(5), W411-5. https://doi.org/10.2214/AJR.08.2256

Funck-Brentano, T., & Cohen-Solal, M. (2015). Subchondral bone and osteoarthritis. *Current Opinion in Rheumatology*, *27*, 420–426.

Hajidah, D. H., & Dwihapsari, Y. (2021). Quantitative T2 magnetic resonance imaging: Analysis of the effect of echo time on images and signal to noise ratio on agarose. *AIP Conference Proceedings*, *2346*. https://doi.org/10.1063/5.0048234

Hash, T. W. (2013). Magnetic resonance imaging of the knee. *Sports Health*, *5*(1), 78–107. https://doi.org/10.1177/1941738112468416

Hitachi hightech. (n.d.). *Principle of ICP Optical Emission Spectrometry (ICP-OES) : Hitachi High-Tech GLOBAL*. Retrieved December 17, 2022, from https://www.hitachi-hightech.com/global/products/science/tech/ana/icp/descriptions/icp-oes.html

Hügle, T., & Geurts, J. (2017). What drives osteoarthritis?—synovial versus subchondral bone pathology. *Rheumatology*, *56*(9), 1461–1471. https://doi.org/10.1093/rheumatology/kew389

Ishiguro, N., Kojima, T., & Poole, A. R. (2002). Mechanism of cartilage destruction in osteoarthritis. *Nagoya Journal of Medical Science*, *65*(3–4), 73–84. https://doi.org/10.18999/nagjms.65.3-4.73

Jacques, S. L. (2013). Optical properties of biological tissues: a review. *Physics in Medicine and Biology*, *58*(11), R37- 61. https://doi.org/10.1088/0031-9155/58/11/R37

Jadin, K. D., Wong, B. L., Bae, W. C., Li, K. W., Williamson, A. K., Schumacher, B. L., Price, J. H., & Sah, R. L. (2005). Depth-varying density and organization of chondrocytes in immature and mature bovine articular cartilage assessed by 3D imaging and analysis. *Journal of Histochemistry and Cytochemistry*, *53*(9), 1109–1119. https://doi.org/10.1369/jhc.4A6511.2005

Johnson, V. L., & Hunter, D. J. (2014). The epidemiology of osteoarthritis. *Best Practice & Research. Clinical Rheumatology*, *28*(1), 5–15. https://doi.org/10.1016/j.berh.2014.01.004

Jung, B. A., & Weigel, M. (2013). Spin echo magnetic resonance imaging. *Journal of Magnetic Resonance Imaging*, *37*(4), 805–817. https://doi.org/10.1002/jmri.24068

Khella, C. M., Asgarian, R., Horvath, J. M., Rolauffs, B., & Hart, M. L. (2021a). Anti-inflammatory therapeutic approaches to prevent or delay post-traumatic osteoarthritis (PTOA) of the knee joint with a focus on sustained delivery approaches. *International Journal of Molecular Sciences*, *22*(15), 8005. https://doi.org/10.3390/ijms22158005

Khella, C. M., Asgarian, R., Horvath, J. M., Rolauffs, B., & Hart, M. L. (2021b). An evidence-based systematic review of human knee post-traumatic osteoarthritis (PTOA): Timeline of clinical presentation and disease markers, comparison of knee joint PTOA models and early disease implications. *International Journal of Molecular Sciences*, *22*(4), 1996. https://doi.org/10.3390/ijms22041996

Kidd, B. (2012). Mechanisms of pain in osteoarthritis. *HSS J.*, *8*, 26–28.

Kim, Y.-M., & Joo, Y.-B. (2012). Patellofemoral osteoarthritis. *Knee Surgery & Related Research*, *24*(4), 193–200. https://doi.org/10.5792/ksrr.2012.24.4.193

Kingfisher. (n.d.). *Kingfisher Biotech Circular Subject: Rabbit as an Animal Model*. Retrieved February 15, 2021, from https://www.kingfisherbiotech.com/newsletter/Rabbit_Animal_Model_Newsletter.pdf

Korhonen, R. K., Julkunen, P., Wilson, W., & Herzog, W. (2008). Importance of collagen orientation and depth-dependent fixed charge densities of cartilage on mechanical behavior of chondrocytes. *Journal of Biomechanical Engineering*, *130*(2), 21003. https://doi.org/10.1115/1.2898725

Kramer, W. C., Hendricks, K. J., & Wang, J. (2011). Pathogenetic mechanisms of posttraumatic osteoarthritis: Opportunities for early intervention. *International Journal of Clinical and Experimental Medicine*, *4*(4), 285–298.

Largo, R., Roman-Blas, J. A., Moreno-Rubio, J., Sánchez-Pernaute, O., Martínez-Calatrava, M. J., Castañeda, S., & Herrero-Beaumont, G. (2010). Chondroitin sulfate improves synovitis in rabbits with chronic antigen-induced arthritis. *Osteoarthritis and Cartilage*, *18*(SUPPL. 1), S17–S23. https://doi.org/10.1016/j.joca.2010.01.017

Lee, J. H., Badar, F., Kahn, D., Matyas, J., Qu, X., & Xia, Y. (2015). Loading-induced changes on topographical distributions of the zonal properties of osteoarthritic tibial cartilage - A study by magnetic resonance imaging at microscopic resolution. *Journal of Biomechanics*, *48*(13), 3625–3633 https://doi.org/10.1016/j.jbiomech.2015.08.011

Lee, J. H., & Xia, Y. (2013). Quantitative zonal differentiation of articular cartilage by microscopic magnetic resonance imaging, polarized light microscopy, and Fourier-transform infrared imaging. *Microscopy Research and Technique*, *76*(6), 625–632. https://doi.org/10.1002/jemt.22209

Lehneis, H. R. (1987). Bone and Cartilage : Structure and Biomechanics. *Orthodics and Prosthetics*, *41*(1), 37–40

Lesperance, L. M., Gray, M. L., & Burstein, D. (1992). Determination of fixed charge density in cartilage using nuclear magnetic resonance. *Journal of Orthopaedic Research : Official Publication of the Orthopaedic Research Society*, *10*(1), 1–13. https://doi.org/10.1002/jor.1100100102

Leucht, F., Dürselen, L., Hogrefe, C., Joos, H., Reichel, H., Schmitt, H., Ignatius, A., & Brenner, R. E. (2012). Development of a new biomechanically defined single impact rabbit cartilage trauma model for in vivo-studies. *Journal of Investigative Surgery*, *25*(4), 235–241. https://doi.org/10.3109/08941939.2011.630123

Levin, A. S., Chen, C. T. C., & Torzilli, P. A. (2005). Effect of tissue maturity on cell viability in load-injured articular cartilage explants. *Osteoarthritis and Cartilage*, *13*(6), 488–496. https://doi.org/10.1016/j.joca.2005.01.006

Li, J. J., Hosseini-Beheshti, E., Grau, G. E., Zreiqat, H., & Little, C. B. (2019). Stem cell-derived extracellular vesicles for treating joint injury and osteoarthritis. *Nanomaterials*, *9*(2), 1–21. https://doi.org/10.3390/nano9020261

Lieberthal, J., Sambamurthy, N., & Scanzello, C. R. (2015). Inflammation in joint injury and post-traumatic osteoarthritis. *Osteoarthritis and Cartilage*, *23*(11), 1825–1834. https://doi.org/10.1016/j.joca.2015.08.015

Mantebea, H., Batool, S., Hammami, M., & Xia, Y. (2021). Structural morphology of rabbit patella and suprapatella cartilage by microscopic mri and polarized light microscopy. *Cartilage*, *13*(2), 1–11. https://doi.org/10.1177/1947603521990882

Marks, R. (2014). Osteoarthritis and articular cartilage: biomechanics and novel treatment paradigms. *Advances in Aging Research*, *03*(04), 297–309. https://doi.org/10.4236/aar.2014.34039

Moro-oka, T., Matsuda, S., Miura, H., Nagamine, R., Urabe, K., Kawano, T., Higaki, H., & Iwamoto, Y. (2002). Patellar tracking and patellofemoral geometry in deep knee flexion. *Clin Orthop*, *394*, 161–168.

Mow, V. C., Kuei, S. C., Lai, W. M., & Armstrong, C. G. (1980). Biphasic creep and stress relaxation of articular cartilage in compression: theory and experiments. *Journal of Biomechanical Engineering*, *102*(1), 73. https://doi.org/10.1115/1.3138202

Murray, M. M., Zurakowski, D., & Vrahas, M. S. (2004). The death of articular chondrocytes after intra-articular fracture in humans. *The Journal of Trauma*, *56*(1), 128–131. https://doi.org/10.1097/01.TA.0000051934.96670.37

Nishimura, D. G. (1996). *Principles of magnetic resonance imaging.* Stanford Univ. http://books.google.com/books?id=uz9BAQAAIAAJ

Nissman, D. B., Hobbs, R. H., Pope, T. L., Geier, C. D., & Conway, W. F. (2008). Imaging the knee: Ligaments. *Applied Radiology*, *37*(12), 25–32.

Niu, J., Qi, Q., Niu, Y., Dong, C., Dong, Z., Cui, P., & Wang, F. (2017). Patella morphological alteration after patella instability in growing rabbits. *Journal of Orthopaedic Surgery and Research*, *12*(1), 106. https://doi.org/10.1186/s13018-017-0615-y

Novakofski, K. D., Pownder, S. L., Koff, M. F., Williams, R. M., Potter, H. G., & Fortier, L. A. (2016). High-resolution methods for diagnosing cartilage damage in vivo. *Cartilage*, *7*(1), 39–51. https://doi.org/10.1177/1947603515602307

Oldenbourg, R., & Mei, G. (1995). New polarized light microscope with precision universal compensator. J Microscopy. *J Microscopy*, *180*, 140-147.

Olmez, N., & Schumacher, H. R. J. (1999). Crystal deposition and osteoarthritis. *Current Rheumatology Reports*, *1*(2), 107–111. https://doi.org/10.1007/s11926-999-0006-4

Palmieri-Smith, R. M., & Thomas, A. C. (2009). A neuromuscular mechanism of posttraumatic osteoarthritis associated with ACL injury. *Exercise and Sport Sciences Reviews*, *37*(3), 147–153. https://doi.org/10.1097/JES.0b013e3181aa6669

Parvizi, J., & Kim, G. K. (2010). Cartilage. In *High Yield Orthopaedics* (pp. 80–81). Elsevier. https://doi.org/10.1016/B978-1-4160-0236-9.00050-X

Plewes, D. B., & Kucharczyk, W. (2012). Physics of MRI: A primer. *Journal of Magnetic Resonance Imaging*, *35*(5), 1038–1054. https://doi.org/10.1002/jmri.23642

Poole, A. R. (1999). An introduction to the pathophysiology of osteoarthritis. *Front Biosci*, *4*, D662–670.

Poole, A. R., Kojima, T., Yasuda, T., Mwale, F., Kobayashi, M., & Laverty, S. (2001). Composition and structure of articular cartilage: A template for tissue repair. *Clinical Orthopaedics and Related Research*, *391 SUPPL.* https://doi.org/10.1097/00003086-200110001-00004

Pritzker, K. P. H. (1994). Animal models for osteoarthritis: *Annals of the Rheumatic Diseases*, 53, 406–420.

Punzi, L., Galozzi, P., Luisetto, R., Favero, M., Ramonda, R., Oliviero, F., & Scanu, A. (2016). Post-traumatic arthritis: Overview on pathogenic mechanisms and role of inflammation. *RMD Open*, *2*(2), 1–9. https://doi.org/10.1136/rmdopen-2016-000279

Racine, J., & Aaron, R. K. (2014). Post-traumatic osteoarthritis after ACL injury. *Rhode Island Medical Journal (2013)*, *97*(11), 25–28.

Ralphs, J. R., Tyers, R. N. S., & Benjamin, M. (1992). Development of functionally distinct fibrocartilages at two sites in the quadriceps tendon of the rat: the suprapatella and the attachment to the patella. *Anatomy and Embryology*, *185*(2), 181–187. https://doi.org/10.1007/BF00185920

Regatte, R. R., Akella, S. V. S., Lonner, J. H., Kneeland, J. B., & Reddy, R. (2006). T1ρ mapping in human osteoarthritis (OA) cartilage: Comparison of T1ρ with T2. *Journal of Magnetic Resonance Imaging*, *23*(4), 547–553. https://doi.org/10.1002/jmri.20536

Riordan, E. A., Little, C., & Hunter, D. (2014). Pathogenesis of post-traumatic OA with a view to intervention. *Best Practice & Research. Clinical Rheumatology*, *28*(1), 17–30. https://doi.org/10.1016/j.berh.2014.02.001

Samuels, M. E., Regnault, S., & Hutchinson, J. R. (2017). Evolution of the patellar sesamoid bone in mammals. *PeerJ*, *5*, e3103. https://doi.org/10.7717/peerj.3103

Shah, M. R., Kaplan, K. M., Meislin, R. J., & Bosco, J. A. (2007). Articular cartilage restoration of the knee. *Bulletin of the NYU Hospital for Joint Diseases*, *65*(1), 51–60.

Shapiro, E. M., Borthakur, A., Dandora, R., Kriss, A., Leigh, J. S., & Reddy, R. (2000). Sodium visibility and quantitation in intact bovine articular cartilage using high field (23)Na MRI and MRS. *Journal of Magnetic Resonance (San Diego, Calif. : 1997)*, *142*(1), 24–31. https://doi.org/10.1006/jmre.1999.1932

Snoeker, B., Turkiewicz, A., Magnusson, K., Frobell, R., Yu, D., Peat, G., & Englund, M. (2020). Risk of knee osteoarthritis after different types of knee injuries in young adults: A population-based cohort study. *British Journal of Sports Medicine*, *54*(12), 725–730. https://doi.org/10.1136/bjsports-2019-100959

Spector, T. D., & MacGregor, A. J. (2004). Risk factors for osteoarthritis: genetics. *Osteoarthritis and Cartilage*, *12 Suppl A*, S39-44. https://doi.org/10.1016/j.joca.2003.09.005

Tecklenburg, K., Dejour, D., Hoser, C., & Fink, C. (2006). Bony and cartilaginous anatomy of the patellofemoral joint. *Knee Surgery, Sports Traumatology, Arthroscopy*, *14*(3), 235–240. https://doi.org/10.1007/s00167-005-0683-0

Terkeltaub, R. A. (2002). What does cartilage calcification tell us about osteoarthritis? *Journal of Rheumatology*, *29*(3), 411–415.

Thomas, B., Bhat, K., & Mapara, M. (2012). Rabbit as an animal model for experimental research. *Dental Research Journal*, *9*(1), 111. https://doi.org/10.4103/1735-3327.92960

Tischer, T., Milz, S., Maier, M., Schieker, M., & Benjamin, M. (2002). An immunohistochemical study of the rabbit suprapatella, a sesamoid fibrocartilage in the quadriceps tendon containing aggrecan. *Journal of Histochemistry and Cytochemistry*, *50*(7), 955–960. https://doi.org/10.1177/002215540205000709

Umlauf, D., Frank, S., Pap, T., & Bertrand, J. (2010). Cartilage biology, pathology, and repair. *Cellular and Molecular Life Sciences*, *67*(24), 4197–4211. https://doi.org/10.1007/s00018-010-0498-0

Valdes, A. M., Doherty, S. A., Muir, K. R., Wheeler, M., Maciewicz, R. A., Zhang, W., & Doherty, M. (2013). The genetic contribution to severe post-traumatic osteoarthritis. *Annals of the Rheumatic Diseases*, *72*(10), 1687–1690. https://doi.org/10.1136/annrheumdis-2012-202562

Wang, N., Badar, F., & Xia, Y. (2015). MRI properties of a unique hypo-intense layer in degraded articular cartilage. *Physics in Medicine and Biology*, *60*(22), 8709–8721. https://doi.org/10.1088/0031-9155/60/22/8709

Wang, N., Chopin, E., & Xia, Y. (2013). The effects of mechanical loading and gadolinium concentration on the change of T1 and quantification of glycosaminoglycans in articular cartilage by microscopic MRI. *Physics in Medicine and Biology*, *58*(13), 4535–4547. https://doi.org/10.1088/0031-9155/58/13/4535

Wang, N., & Xia, Y. (2011). Dependencies of multi-component T2 and T1rho relaxation on the anisotropy of collagen fibrils in bovine nasal cartilage. *J Magn Reson*, *212*, 124–132.

Wang, N., & Xia, Y. (2012). Orientational dependent sensitivities of T 2 and T 1ρ towards trypsin degradation and Gd-DTPA 2- presence in bovine nasal cartilage. *Magnetic Resonance Materials in Physics, Biology and Medicine*, *25*(4), 297–304. https://doi.org/10.1007/s10334-011-0288-1

Watt, F. E., Corp, N., Kingsbury, S. R., Frobell, R., Englund, M., Felson, D. T., Levesque, M., Majumdar, S., Wilson, C., Beard, D. J., Lohmander, L. S., Kraus, V. B., Roemer, F., Conaghan, P. G., Mason, D. J., Adams, J., Blank, M., Batt, M., Biggs, P., … Bierma-Zeinstra, S. (2019). Towards prevention of post-traumatic osteoarthritis: report from an international expert working group on considerations for the design and conduct of interventional studies following acute knee injury. *Osteoarthritis and Cartilage*, *27*(1), 23–33. https://doi.org/10.1016/j.joca.2018.08.001

Williams, G. M., Klisch, S. M., & Sah, R. L. (2008). Bioengineering cartilage growth, maturation, and form. *Pediatric Research*, *63*(5), 527–534. https://doi.org/10.1203/PDR.0b013e31816b4fe5

Williamson, A. K., Chen, A. C., & Sah, R. L. (2001). Compressive properties and function-composition relationships of developing bovine articular cartilage. *Journal of Orthopaedic Research*, *19*(6), 1113–1121. https://doi.org/10.1016/S0736-0266(01)00052-3

Wolman, M. (1975). Polarized light microscopy as a tool of diagnostic pathology. A review. *Journal of Histochemistry and Cytochemistry*, *23*(1), 21–50. https://doi.org/10.1177/23.1.1090645

Xia., Y., Momot., K.I., Chen., Z., Chen., C.T., Khan., D., & Badar., F., (2016). CHAPTER 1:Introduction to cartilage , in biophysics and biochemistry of cartilage by nmr and mri. 1–43.

Xia, Y. (1998). Relaxation anisotropy in cartilage by nmr microscopy (μmri) at 14-pm resolution. *Magnetic Resonance in Medicine, 39,* 941–949. https://doi.org/10.1002/mrm.1910390612

Xia, Y. (2000a). Heterogeneity of cartilage laminae in MR imaging. *Journal of Magnetic Resonance Imaging*, *11*(6), 686–693. https://doi.org/10.1002/1522-2586

Xia, Y. (2000b). Magic-angle effect in magnetic resonance imaging of articular cartilage. *Investigative Radiology*, *35*, 602–621. https://doi.org/10.1097/00004424-200010000-00007

Xia, Y. (2007). Resolution "scaling law" in MRI of articular cartilage. *Osteoarthritis and Cartilage*, *15*(4), 363–365. https://doi.org/10.1016/j.joca.2006.12.004

Xia, Y., Alhadlaq, H., Ramakrishnan, N., Bidthanapally, A., Badar, F., & Lu, M. (2008). Molecular and morphological adaptations in compressed articular cartilage by polarized light microscopy and fourier-transform infrared imaging. *Journal of Structural Biology*, *164*(1), 88–95. https://doi.org/10.1016/j.jsb.2008.06.009

Xia, Y., Moody, J. B., Burton-Wurster, N., & Lust, G. (2001). Quantitative in situ correlation between microscopic MRI and polarized light microscopy studies of articular cartilage. *Osteoarthritis and Cartilage*, *9*(5), 393–406. https://doi.org/10.1053/joca.2000.0405

Xia, Y., & Zheng, S. (2010). Reversed laminar appearance of articular cartilage by T1-weighting in 3D fat-suppressed spoiled gradient recalled echo (SPGR) imaging. *Journal of Magnetic Resonance Imaging*, *32*(3), 733–737. https://doi.org/10.1002/jmri.22278

Xia, Y., Zheng, S., & Bidthanapally, A. (2008). Depth-dependent profiles of glycosaminoglycans in articular cartilage by μMRI and histochemistry. *Journal of Magnetic Resonance Imaging*, *28*(1), 151–157. https://doi.org/10.1002/jmri.21392

Zheng, S., & Xia, Y. (2010). The impact of the relaxivity definition on the quantitative measurement of glycosaminoglycans in cartilage by the MRI dGEMRIC method. *Magnetic Resonance in Medicine*, *63*(1), 25–32. https://doi.org/10.1002/mrm.22169